New Insights Into The Mathematics Of The Brain:

Neuro-Quantum Elementally Connective Relationships (Functional, Geometrical and Magnetic), with Possible Implications for Neurological Health and Wider Quantum Physics

First Edition

By

Dr Ricardo Joseph Simeoni

Neurödinger

New Insights Into The Mathematics Of The Brain:

Neuro-Quantum Elementally Connective Relationships (Functional, Geometrical and Magnetic), with Possible Implications for Neurological Health and Wider Quantum Physics

First Edition

By

Dr Ricardo Joseph Simeoni

PhD *JCU*, MAppSc(MedPhys) *QUT*, BAppSc(Phys) *QUT*, GDipT(Sec) *ACU*, GCMagResonTech *Qld*

Neurödinger Reports

" Bringing the quantum world to neural signalling for brain-computer interfacing, neuroprosthetics and neural health "

Published by

Neurödinger

Buddina
Queensland 4575, Australia

First Edition Published November 14, 2022

The mountain/star trail image and central (only) portion of the constituted "record" image (the latter also having been annotated) of the front cover are attributed to Getty Images.

ISBN: 978–0–646–86663–5

Contents

Preface

This report follows my two most recent scientific publications, namely: *A New Approach to High-Order Electroencephalogram Phase Analysis Details the Mathematical Mechanisms of Central Nervous System Impulse Encoding* (1 March 2021, with associated patent pending priority date of 9 September 2020) and *Chronic Fatigue Syndrome: A Quantum Mechanical Perspective* (9 May 2022). The first of these publications is a substantial 34 page paper that was formally peer reviewed by two United States-based engineering academics, with the review describing the paper's analysis as "inspired". The second publication represents high-interest academic journalism around the topic of chronic fatigue syndrome (CFS), and also includes the presentation of preliminary results for a Case Study based around a CFS mechanism hypothesised from the above peer reviewed paper. These publications are respectively contained within Appendices A and B such that the report represents a complete volume of related works. The report component of this volume is pitched for a broad readership, ranging from those with a general scientific interest in the mathematics of nature, to those with biomedical engineering or quantum physics interests.

In following on from the above publications, the report identifies:

- Further quantum mechanical-like characteristics of the brain's neural signalling.
- New insights into the mathematics of the brain, including that prime numbers are over-represented throughout the complexities of the brain's neural signalling, which to some may carry implication beyond mathematical intrigue.
- Further evidence of the periodic table's imprint upon the brain's neural signalling, here in association with *symmetrical functional geometries of neuro-quantum states* structured in a "henge-like" arrangement.
- Element-based magnetic susceptibility relationships within the above neuro-quantum functional arrangement.
- Heavy metal neural interference pathways within the above neuro-quantum functional arrangement.
- Newly derived, seemingly profound underlying quantisation relationships for the above neuro-quantum functional arrangement, with universal (beyond neurological) application.

In arriving at these new findings, the report further considers and analyses the above-noted CFS Case Study, particularly in relation to heavy metals, to provide unique insights into possible CFS instigation and recovery mechanisms. These insights are also considered in a broader health context but with recognition that, because they are from mathematical and biophysical perspectives, the report is classified as *non-medical*.

Finally, the widely recognised discoveries and thought discussions from a much celebrated age of physics, some 100 years ago, are typically elegant in their complexity, and in some cases even elegant in their powerful outward simplicity (with inner sophistication). In the spirit of that celebrated age, the report's original and seemingly profound quantisation relationships are more readily physically visualised and applied (including for large multiple particle systems) than many of the abstract mathematical constructs typical of quantum mechanics formalism, and are explained for non-experts in line with the report's broad readership pitch. It is anticipated that the readership will find the report's own hypothetical thought discussions, which complement its more formal aspects, to be engaging, and that interest will be such that a readership subset will follow the report's formal lead in terms of future undertaken research.

Dr Ricardo J. Simeoni
Neurödinger Director

1. Qualifying Declarations

This and the following Sections predominantly cite [1,2] which are the publications named within the Preface as forming a complete volume of work along with the present report. While details of [1,2] are expectedly given within the report's References Section, for convenience and completeness their full copies are also contained within Appendices A and B respectively.

Presented in [2] is a chronic fatigue syndrome (CFS) Case Study and new CFS hypothesis stemming from [1]. While the preliminary results of [2] are interesting, if not remarkable, they require validation by a formally controlled and independent study, and consequently so too do *some* report aspects which represent insightful continuations of the analysis in [2]. Despite this statement of caution, such report aspects potentially represent important stepping stones, while other aspects, like prime number observations, heavy metal interference pathways, and several quantum-based deliberations, are heavily based on [1] and are fully or mostly independent of [2].

The report does not reintroduce CFS other than to reaffirm it being a neurological illness known for its complexity due to its confounding impact on multiple body systems, and readers are directed to [2], or prominent reviews such as those cited within [2], for a topic introduction. Finally, all contained observations and associated discussions are ultimately from qualified mathematics and physics perspectives (i.e., no medical or nutritional advice is intended, and nor should it be taken, from the report).

2. Overview of New High-Order Phase Analysis and CFS Case Study

A new form of high-order phase analysis reveals the presence of many structured phase changes, $\Delta\phi$, within the complexities of the electroencephalogram (EEG) [1], and it is from the findings of [1] that prime numbers within, and deeper insights into the mathematical functionality of, the brain will soon be extracted. Within [1] $\Delta\phi$ from the EEGs of several clinical subjects are initially grouped into ten Families, namely, eight Primary Families for which $\Delta\phi$ cluster about $\Delta\phi_c = 5^\circ, 10^\circ, 20^\circ, 30^\circ, 50^\circ, 90^\circ, 180^\circ\ 270^\circ$, and two Secondary Families for which $\Delta\phi$ cluster about $\Delta\phi_c = 135^\circ$ and 220°. Furthermore, the Families display fine structure, with member $\Delta\phi$s being separated by integer or fractional integer amounts of a proposed quantum increment value, α, which is determined to high precision for each Family. A "global" α value that applies across Families is additionally identified and, based on α versus $\Delta\phi_c$ modelling, corresponds to a Global Family value of $\Delta\phi_c \approx 25^{\circ}$. Note that from this point the expression "Family $\Delta\phi$" replaces the $\Delta\phi_c$ notation of [1].

Finally, linear mapping of Family $\Delta\phi$ values to atomic numbers, Z, via $\Delta\phi/5 \rightarrow Z$, results in associated element labelling of: (i) H, He*, Be, C, Ne*, Ar*, Kr* and Xe* for Primary Families (where the asterisk signifies a noble gas); (ii) Co and Ru for Secondary Families; and (iii) B for the Global Family. Several identified quantum mechanical-like characteristics of the high-order neural phase encodings, e.g., Family fine structuring via α and symmetries therein, leads to the suggestion in [1] that associations between Families and elements are suggestive of neuro-quantum processes involving optimal quantum states with elemental imprints.

Adding to quantum interest is the CFS Case Study of [2], which hypothesises that telecommunication-associated atmospheric electromagnetic radiation (i.e., the "modern ether") may interfere with the $\Delta\phi$ and/or α values of [1], since these values overlap with typical phase changes within the modern ether. Note however that this report, like [2], takes a non-alarmist approach to possible adverse modern ether effects, advocating that professional bodies (such as the World Health Organization, Australian Radiation Protection and Nuclear Safety Agency, and International Commission for Non-ionising Radiation Protection) should continue to form the basis of society's position on exposure, and that the hypothesised neural interference is not problematic for the majority.

Within [2] body mineral levels, based on Oligoscans of the (non-independent) Case Study subject, seemingly change in response to modern ether removal (for several hours per day, including during some hours of sleep, and for several months). The changes display the following quantum mechanical and other characteristics:

- The most electromagnetically relevant elements demonstrate the largest percentage increase in levels (with for example ferromagnetic Co and Ni being the mineral and heavy metal that display the highest percentage increase).
- Element level changes appear to be dependent upon, and symmetrically structured according to, quantities such as their Z, nuclear spin, and/or associated $\Delta\phi$.

- The Z values of elements involved demonstrate proportionalities observed within a fine structure extension to Bohr's model of the hydrogen atom [3], and also within the ratios of some hydrogen transition probabilities or line intensities (for transitions between half-integer fine structure states distinguished by a conventional quantum number of total angular momentum).

Note that the above hydrogen proportionalities are not meant to imply direct association but rather are analogously raised because spectral similarities are observed across many scales of quantum mechanics, and so the proportionalities broadly further suggest a quantum presence, as well as magnetic involvement (since magnetism is ultimately responsible for the spin-orbit interactions that give rise to fine atomic structure). Also note that modern ether removal combined with a relatively serene approach to neural stimulation is coined "quantum treatment" in [2] and throughout this report, more so for the quantum mechanical basis of its hypothesis and the quantum mechanical-like characteristics of its apparent effects.

Following an extended periodic table perspective of the $\Delta\phi$ Families, additional quantum-like (and mathematical/physical) features of interest can also be identified, and these immediately follow.

3. Prime Numbers in the Human Brain

While the objective of this Section, to identify prime numbers within the brain, may initially appear solely focused on providing another example of an intriguing mathematical form in nature, the example will, as the report progresses, also make a quantum mechanical statement of potential significance.

3.1 General Comment on Prime Numbers in Nature

Occurrences of prime numbers in nature are rare, with these occurrences typically isolated to one or two numbers rather than a sequence or part thereof (in stark contrast to the famous Fibonacci sequence which is widely observed in nature). Furthermore, the identification of some elegant formula that generates the prime numbers is one of the last yet-to-be-conquered frontiers of mathematics (again in contrast to the Fibonacci sequence), despite the intense attempts by some of the greatest mathematical minds throughout modern history.

Hence, for some, the identification of multiple prime numbers in any environment indicates the presence of intelligence and/or design complexity, and has even been flagged as a possible indicator of extraterrestrial life, if ever observed within some future-detected cosmic signal. The continuing analysis to follow reveals the interesting finding of prime number over-representation within the brain's neural signalling, thereby at a minimum demonstrating yet another facet of the brain's remarkable complexity of intellect.

3.2 Deriving Prime Numbers from High-Order Phase Analysis

Elements corresponding to the $\Delta\phi$ Families following $\Delta\phi/5 \rightarrow Z$ linear mapping are highlighted within the periodic table of Figure 1. Shades of highlight in Figure 1 distinguish between Primary, Secondary and Global Family status. It should be remembered here and throughout this report that, while the linear mapping of $\Delta\phi$ to Z in isolation gives the impression of neural process simplicity, the derivation of $\Delta\phi$ (with fine structure α) is based on high-order analysis and demonstrates highly sophisticated and analytically powerful neural functionality (see [1] for a physical interpretation of the high-order in $\Delta\phi$).

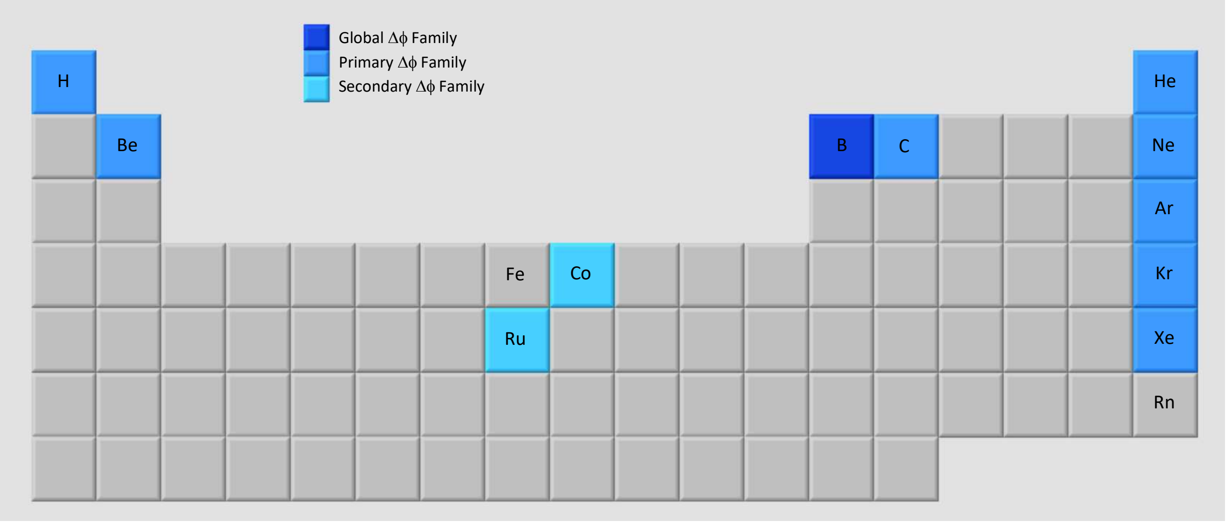

Figure 1: The periodic table with elements corresponding to the $\Delta\phi$ Families of [1] highlighted, and shades of highlight distinguishing between Primary, Secondary and Global Family status. The additional inclusions of Fe and Rn (which presently do not correspond to a $\Delta\phi$ Family) are based on Fe's physical connectivities with Co and Ru, as per the forthcoming commentaries of Subsections 4.2, 6.2 and 7.2, and the labelling completeness provided by Rn in regards to natural noble gases.

Given the scarcity of prime numbers in nature, an interesting finding is that the Δϕ Family-associated elements of Figure 1 generate a multitude of prime numbers when their Z values are paired (based on having adjacent locations within the periodic table or on one of the elements being H, B or Co), and then added or subtracted, as demonstrated by Table 1. While such a finding may appear coincidental, and so without biophysical basis, it possibly carries an important quantum mechanical implication, as briefly raised in Subsection 4.3.

Table 1: Elements corresponding to Δϕ Families and for which pairing generates prime numbers upon the addition or subtraction of their atomic numbers, Z_1 and Z_2. Element pairing is based on having adjacent locations within the periodic table, or on one of the elements being H, B or Co. Where a pairing criterion yields a repeat pair, prime numbers are displayed in light text. Note that the B-associated Δϕ Family holds Global status. While not directly corresponding to a Δϕ Family, Fe and Rn are included, by way of Co-Fe and Co-Rn supplementary pairings, on the bases of physical connectivities between Fe, Co and Ru (Subsections 4.2, 6.2 and 7.2) and the natural noble gas labelling completeness provided by Rn.

Element Pair	$Z_1 + Z_2$	$Z_1 - Z_2$	**Element Pair**	$Z_1 + Z_2$	$Z_1 - Z_2$
Adjacent pairing			*H pairing*		
H-He	3		H-He	3	
H-Be	5	3	H-Be	5	3
H-Ne	11		H-C	7	5
B-C	11		H-Ne	11	
Co-Ru	71	17	H-Ar	19	17
			H-Kr	37	
			H-Xe		53
B (Global) pairing			*Co pairing*		
B-He	7	3	Co-He	29	
B-C	11		Co-Be	31	23
B-Ar	23	13	Co-Ne	37	17
B-Kr	41	31	Co-Ru	71	17
B-Xe	59		Co-Fe	53	
			Co-Rn	113	59

Note that in forming adjacent Δϕ Family pairs, a circular periodic table format is applied whereby Group 18 is considered adjacent to Group 1, and so the Primary Family associated with H is considered adjacent not just to the Be-associated Primary Family, but also to the He- and Ne-associated Primary Families.

The following outcomes apply to the $Z_1 + Z_2$ prime number distributions (for $\Delta\phi$ Families) of Table 1, with *p*-values indicating statistical support, albeit modest in most cases, for an over-representation of prime numbers (bracketed *P*-values are explained following the listed outcomes):

- All five possible element pairs, formed by the criterion of $\Delta\phi$ Families being adjacent, yield a prime number (vertical intra-Group noble gas adjacent pairs not considered, see top left quadrant of Table 1), $p < 0.004$ ($P = 0.32$).
- Six of the ten possible element pairs, formed by the criterion of H being a partner element, yield a prime number (reduces to six of eight if only pairs generating odd *Z* differentials are considered, see top right quadrant of Table 1), $p \leq 0.05$ ($P = 0.32$).
- Four of the five possible element pairs, formed by the criterion of B being partnered with a noble gas, yield a prime number (see bottom left quadrant of Table 1), $p < 0.05$ ($P = 0.32$).
- Five of the ten possible element pairs, formed by the criterion of B being a partner element, yield a prime number (see bottom left quadrant of Table 1), $p = 0.05$ ($P = 0.24$).
- Collectively, fifteen of all forty-five possible combinations of element pairs yield a prime number (vertical intra-Group noble gas adjacent pairs not considered), $p \leq 0.05$ ($P = 0.24$).

The probability of $Z_1 + Z_2$ (for randomly selected and dissimilar *Z*) generating a prime number by chance depends on the maximum value of *Z*, with utilised average probabilities ranging from $P = 0.32$ for $Z_{\max} = 18$, to $P = 0.24$ for $Z_{\max} = 50$. In *some* cases, the conclusion of a statistically supported over-representation of prime numbers for the above outcomes depends on the in-range value of *P*, and therefore on considerations that include one's manner of null hypothesis construction (several permutations provide interest) and philosophical perspective (one might for example consider the relatively low *Z* values of some $\Delta\phi$ Families as representing a bias towards subsequent prime number generation, or as consequential of an inherent nature of deliberate prime number generation that contributes to Family/element selection).

For the applied approximate analysis, $P = 0.32$ is considered conservative, while $P = 0.24$ is non-conservative (unbiased) but arguably justifiable. However, the first of the above-listed outcomes demonstrates a strong over-representation of prime numbers regardless of *P* value or perspective, which alone speaks to the extraordinary uniqueness and embedded complex high-order functional sophistication of the brain, given the otherwise scarcity of prime numbers in nature and the more typical artificial means of their generation.

3.3 Other Prime Number Observations of Bearing

It was discovered by [4] that the parabolic curve-of-best-fit ($r^2 = 0.997$, $p < 0.001$) through the Z values of the six natural noble gases (five of which are $\Delta\phi$ Family-associated elements) is exactly given by the following function involving prime numbers 2, 3 and 7:

$$Z = \left(3 - \tfrac{1}{7}\right)x^2 + 2x + \left(3 + \tfrac{1}{7}\right), \tag{1a}$$

where $x = 0, 1, 2, 3, 4, 5$ respectively for the six natural noble gases in ascending Z order (and the curve-of-best-fit residuals are shown in [4] to carry quantum-like properties).

Additionally, the parabolic curve-of-best-fit ($r^2 > 0.9999$, $p < 0.001$, and with error margins stated at 95% CI) for Family (median) α versus $\Delta\phi$ modelling in degrees is given by [1]:

$$\overline{\alpha}_{\Delta\phi} = (1.9772 \pm 0.0049) \times 10^{-4} \Delta\phi^2 - (9.990 \pm 0.097) \times 10^{-3} \Delta\phi + (3.002 \pm 0.021) \times 10^{-1}, \tag{1b}$$

with the numerical symmetry and prime number connectedness of (1b) emphasised by expressing to two significant figures, i.e., $10\overline{\alpha}_{\Delta\phi} = 2.0 \times 10^{-3} \Delta\phi^2 - 1.0 \times 10^{-1} \Delta\phi + 3.0$. Hence, here prime numbers 2 and 3 again bear some association with $\Delta\phi$ and so with related Families, albeit with reliance on the specified precision reduction and the "degree" unit being physically meaningful (which is evidentially supported later).

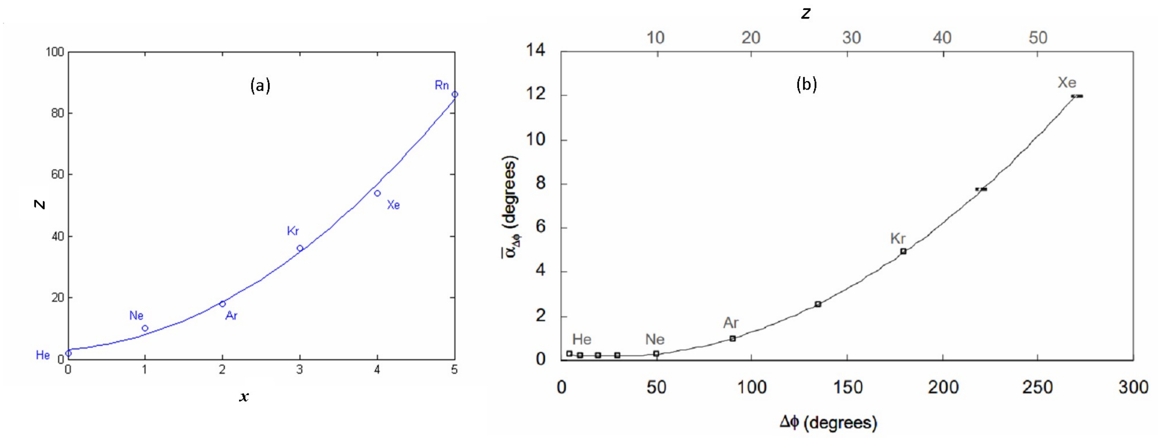

Figure 2: (a) Atomic number, Z, versus x for the noble gases (taken from [4]), where x is a monotonically increasing integer assigned to each successive noble gas and curve residuals carry quantum-like properties, and (b) Family $\overline{\alpha}_{\Delta\phi}$ versus $\Delta\phi$ (taken from [1]), where the secondary x-axis signifies $\Delta\phi/5 \rightarrow Z$ mapping with annotations identifying five of eight Primary $\Delta\phi$ Families that coincide with the Z of indicated noble gases. Error bars (95% CI) are resolvable (just) for the two right-most points only.

As per the opening paragraph of Subsection 3.2 in regards to high-order sophistication amidst a seemingly simple linear mapping façade, the parabolic functions (1a) and (1b), of Figures 2a and 2b respectively, may give a similar ostensible impression. However, countering any such impression is the fact that parabolic functionality is a component of some fundamentally important quantum mechanical systems, and so here it seems that, as repeated throughout this report, the elegant simplicity of (1a) and (1b) veils sophistication and adds to the cases made by [1] and [2] in their identifications of quantum mechanical-like characteristics within neural signalling.

4. General Observations Supporting the Physical and Quantum Significance of a Periodic Table Perspective

Associations for five of the six natural noble gases with $\Delta\phi$ Families support the notion that Family location holds significance within a periodic table perspective. The pairing of Families, based on the adjacent locations of their mapped elements, to generate prime numbers (as per Figure 1 and Table 1) adds to this support, as do the forthcoming deliberately *generalised* observations of this Section (with specificity collectively and progressively provided later by Sections 6, 7 and 9).

4.1 Changing $\Delta\phi$ Across the Periodic Table

The change in Z for vertically and diagonally (left and right) adjacent elements within the periodic table is given by:

$$\Delta Z = (2n^2 + 1) \qquad \text{(diagonal-right)} \qquad (2a)$$

$$\Delta Z = 2n^2 \qquad \text{(vertical)} \qquad (2b)$$

$$\Delta Z = (2n^2 - 1) \qquad \text{(diagonal-left),} \qquad (2c)$$

where n = 1, 2, 3, 4 and the three equations might analogously be considered as respectively representing P, Q and R change-of-state transition branches as often seen in molecular physics (where branches signify a different total angular momentum change). This analogy follows the continuing conceptual theme of element-associated neuro-quantum states. However, even without this analogy it is evident that (2a) to (2c) are expectedly reflective of differentials arising from standard discrete atomic orbital filling and the principal energy level degeneracy of hydrogen, and so are inherently quantum-based.

Substituting $Z \equiv \Delta\phi/5$ into (2a) to (2c), i.e., applying reverse linear mapping as per [2], the change in $\Delta\phi$ (in degrees) between adjacent periodic table elements (or neuro-quantum states) is respectively given by (3a) to (3c) for the P, Q and R branches:

$$\Delta\phi = 10(n^2 + ½) \qquad \text{(diagonal-right, P)} \qquad (3a)$$

$$\Delta\phi = 10n^2 \qquad \text{(vertical, Q)} \qquad (3b)$$

$$\Delta\phi = 10(n^2 - ½) \qquad \text{(diagonal-left, R).} \qquad (3c)$$

Note that within (3a) to (3c) $\boldsymbol{\Delta\phi}$ is technically $\Delta(\Delta\phi)$ since a change in $\Delta\phi$ is under consideration. However, the double Δ is easily inferred and so for conciseness is simply expressed in the bolded form of $\boldsymbol{\Delta\phi}$. Perhaps also noteworthy is that many $\boldsymbol{\Delta\phi}$ values generated by (3a) to (3c) correspond to Family $\Delta\phi$ and/or landmark polar angles.

An example application of (3b) for adjacent noble gas Group 18 elements generates associated $\boldsymbol{\Delta\phi}$ values of 40°, 40°, 90°, 90°, 160°, 160° (to Og) which displays n degeneracy (2, 2, 3, 3, 4, 4) by not automatically incrementing after each equation application.

Another brief application example, this time for (3a) which applies to diagonal-right elements such as C → P → Se → I → Rn within the periodic table (see Figure 3), sees the $n = 2$ case generate $\boldsymbol{\Delta\phi} = 45°$. Figure 3 highlights all diagonal-right element pairs for which $\boldsymbol{\Delta\phi} = 45°$, Na-Ca being one such pair and is noted here for the additional purpose of later discussion.

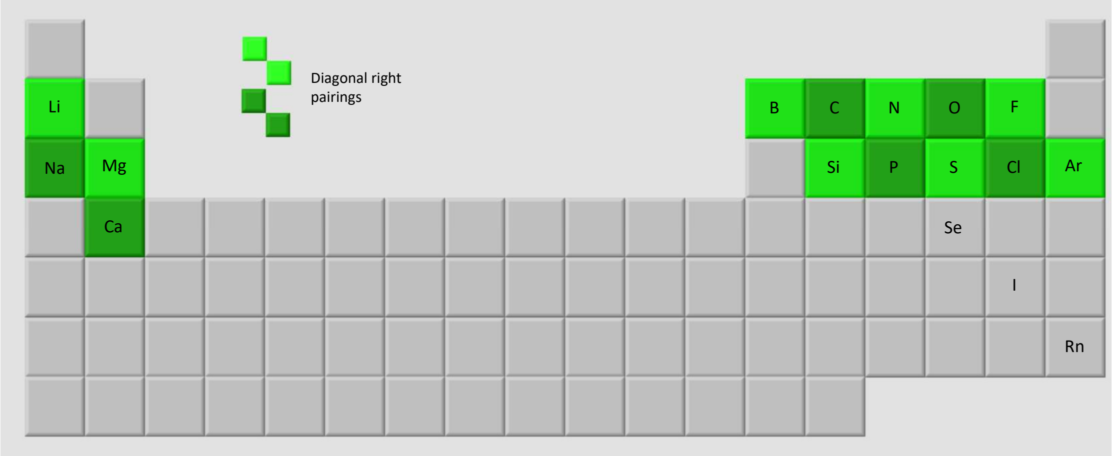

Figure 3: The periodic table highlighting diagonal-right element pairs for which the change in $\Delta\phi$ is 45°, as analytically given by $n = 2$ in (3a). An example complete diagonal to which (3a) applies, C → Rn ($n \geq 2$), is also shown.

The purpose of displaying such $\Delta\phi$ forms is to continue support for the conceptual theme of there being a background presence of quantum mechanics within high-order neural phase encoding, wherein neuro-quantum states appear associated with periodic table elements. This growing support in turn contributes to the validation of a $Z \leftrightarrow \Delta\phi$ synergetic approach. Clearly, the brief application examples here for (3a) and (3b) in isolation are scarcely evidential, but they nonetheless represent a starting point for in-depth and consequential $\Delta\phi$ analyses that follow within proceeding Sections.

4.2 Physical Connectedness of the Iron Grouping of Elements

In addition to its generation of prime numbers (17, 71), the adjacency of the $\Delta\phi$ Families associated with Co and Ru is particularly interesting since Ru vertically proceeds Fe within Group 8 of the periodic table (see Figure 1), resulting in $\Delta\phi = 90^{\circ}$ for $\mathrm{Fe} \rightarrow \mathrm{Ru}$. Expanding upon this interest, Fe and Co are row-wise adjacent within what can be described as the "horizontal iron group" of the periodic table, while Co in the form of vitamin B12 (cyanocobalamin) is central to the production of Fe-containing haemoglobin. Hence, based on these described connectivities it appears that the Co-Ru Family pairing is indeed biophysically, not just mathematically, related (the same then being possible, if not likely, for other Family pairings), and that the supplementary Co-Fe prime number entry of 53 within Table 1 may also be meaningful. This iron grouping of elements will become relevant within later analysis, including on the basis of the integrated CFS Case Study subject displaying historically elevated ferritin levels.

4.3 Neurological Optical-Like "Collisions" Implied From Periodic Table-Generated Prime Numbers

Within [1] resonance-related features of the EEG are analogously compared to resonances within optical and radiative collisions (interactions) of atomic and molecular physics (e.g., involving element pairs such as Na-Ca, He-He, Rb-Na, Rb-K, and many more). Further to that analogous comparison involving pairings, the facts that elements associated with $\Delta\phi$ Families are: (i) adjacently paired within the periodic table (in several cases), and (ii) seemingly biophysically paired by the intriguing and statistically unlikely over-representation of prime numbers following the addition of element Z values as per Subsection 3.2, further support the possibility that element pairs and therefore quantum resonances are indeed neurologically in play.

While the point made above is not reliant on optical-like interactions involving adjacent elements within the periodic table (ordinarily the suitable pairing of element states required to observe specific optical processes can be quite involved, e.g., in terms of selection rules, transition energy matching, and so on), it follows that this large subset of "ordinary adjacent interactions" (e.g., Na-Ca systems) naturally form part of the contextual interest in adjacently paired $\Delta\phi$ Families with apparent connectedness (e.g., He-Ne, He-Be, Co-Ru). Again, these general observations still primarily aim to highlight a background presence of quantum mechanics but may indeed carry specific relevance (i.e., in terms of optical-like resonance involvement) for some past described quantum characteristics.

5. Feature Minerals and Heavy Metals of CFS Case Study

The Case Study of [2] shares a CFS journey for a (non-independent) subject on an apparent road to recovery. The recovery road follows a rationalised hypothesis involving modern ether removal combined with a relatively serene approach to neural stimulation (coined earlier as "quantum treatment"). The preliminary findings of [2] (released in support for the first World ME Day within a general academic interest context) focus on body mineral level changes and appreciable but subjective feelings of CFS improvement. The present report reflects further upon the results of [2], particularly in relation to heavy metals, and applies a more formal and deeper phase wheel analysis following the approach of [1].

After several months of quantum treatment as described in [2], the minerals (out of a total of 21) and heavy metals (out of a total of 15) with the largest percentage increases and decreases were identified and ranked in accordance with Table 2 (which extends by way of heavy metal inclusion a comparable table of [2]). Again following [2], Table 2 additionally includes the four minerals with *absolute levels* associated with a low minus or "red zone", namely P, Zn, Cr and Mo. In relation to these four elements and as described in [2]: P consistently sits in said zone across four diagnostic scans but with gradually increasing levels, possibly indicating impaired/improving oxidative phosphorylation; Zn and Cr commence at a low base level and come to enter said zone; and Mo sits just above said zone after appreciable decline.

Table 2: Heavy metals and minerals with the largest percentage increases and decreases in level following the "quantum treatment" (involving modern ether removal) of [2]. Also included for combined analysis are minerals with absolute levels associated with a low minus or "red zone" (elements in red text) as explained in-text. Most heavy metal changes are relatively slight-to-modest and so emphasis is not placed on their absolute percentage changes.

	Heavy metal	***Z***	**Δϕ (degrees)**	***Mineral (% change)***	***Z***	**Δϕ (degrees)**
Largest % increase	Ni	28	140	Co (+15.8)	27	135
	Bi	83	415	Li (+14.8)	3	15
	Tl	81	405	P* (+14.1)	15	75
	:	:	:	F (+13.4)	9	45
	:	:	:	:	:	:
	:	:	:	:	:	:
	:	:	:	:	:	:
	Hg	80	400	Zn (−5.2)	30	150
	Be	4	20	Cr (−5.6)	24	120
	Gd	64	320	Mo$^\#$ (−14.9)	42	210
Largest % decrease	Ag	47	235	:	:	:
	Pb	82	410	Mg (−40.8)	12	60

*P falls in "red zone" for all four diagnostic scans; $^\#$Mo absolute level falls just above red zone cut-off.

Relative changes only are indicated within the heavy metals ranking of Table 2. Viz., percentage changes are deliberately omitted since their values are generally not as strong as their mineral counterparts, with no discerning change for the majority (as expected). An initial qualitative heavy metal observation based upon Table 2 is the fact that Ni displays the largest increase, which is interesting since while Ni is potentially toxic, it is obviously less harmful, in general, than heavy metals such as As, Cd, Hg, Pb and Tl. In fact, the trace element benefits of Ni (available as a health supplement) are such that its deficiency may disturb skeletal incorporation of Ca and Zn metabolism [5] (and disturbed Zn metabolism certainly seems indicated within the CFS Case Study of [2]).

Bi appearing second behind Ni is similarly qualitatively interesting (since for example Bi is used to treat gastrointestinal disorders, with Bi salts being antibacterial to most Helicobacter pylori isolates [6]). Naturally, a heavy metal not highlighted (i.e., not specified due to placement towards the middle of the Table 2 ranking) is still worthy of consideration within neuro-quantum interference pathways (see later in Section 7), since stimulated or accelerated heavy metal removal in response to quantum treatment should not generally be expected, especially for *all* heavy metals. Similarly, non-highlighted minerals in Table 2 are also worthy of consideration (such as Ca which displays a post-treatment change of −14.8% and is separately analysed in [2]).

While several other qualitative comments arise from a Table 2 perusal, it is not until the $\Delta\phi$ values of its identified elements are graphed, as radials within a polar plot (or *phase wheel* to use the terminology from [1]), that the extent of symmetrical functional geometries between the elements begins to be realised.

6. Phase Wheel Analysis

6.1 Overview

The phase wheel of Figure 4a incorporates Ni, Bi, Pb, Ag and Gd (i.e., the top two and bottom three heavy metals of Table 2). Other "largest changing" heavy metals from Table 2 are temporarily omitted to avoid diagram clutter, but are included within the more comprehensive phase wheel of Figure 4b (and see next Subsection 6.2 for explanation of colour cones and additional mineral inclusions for Figure 4b).

Figure 4c incorporates Table 2's minerals with the largest percentage decreases and lowest absolute levels (Mg, Zn, Cr, Mo) as per Section 5 explanation, while Figure 4d incorporates the minerals with the largest percentage increases (Co, Li, P, F).

Note that Figures 4c and 4d also respectively correspond to even and odd *Z* minerals, and should not be considered in isolation but as a synergetic pair. The ↑ and ↓ annotations within Figures 4b to 4d represent increasing or deceasing percentage level change based on pre- and post-treatment comparisons, and hence the arrows are not intended to directly represent electron spin.

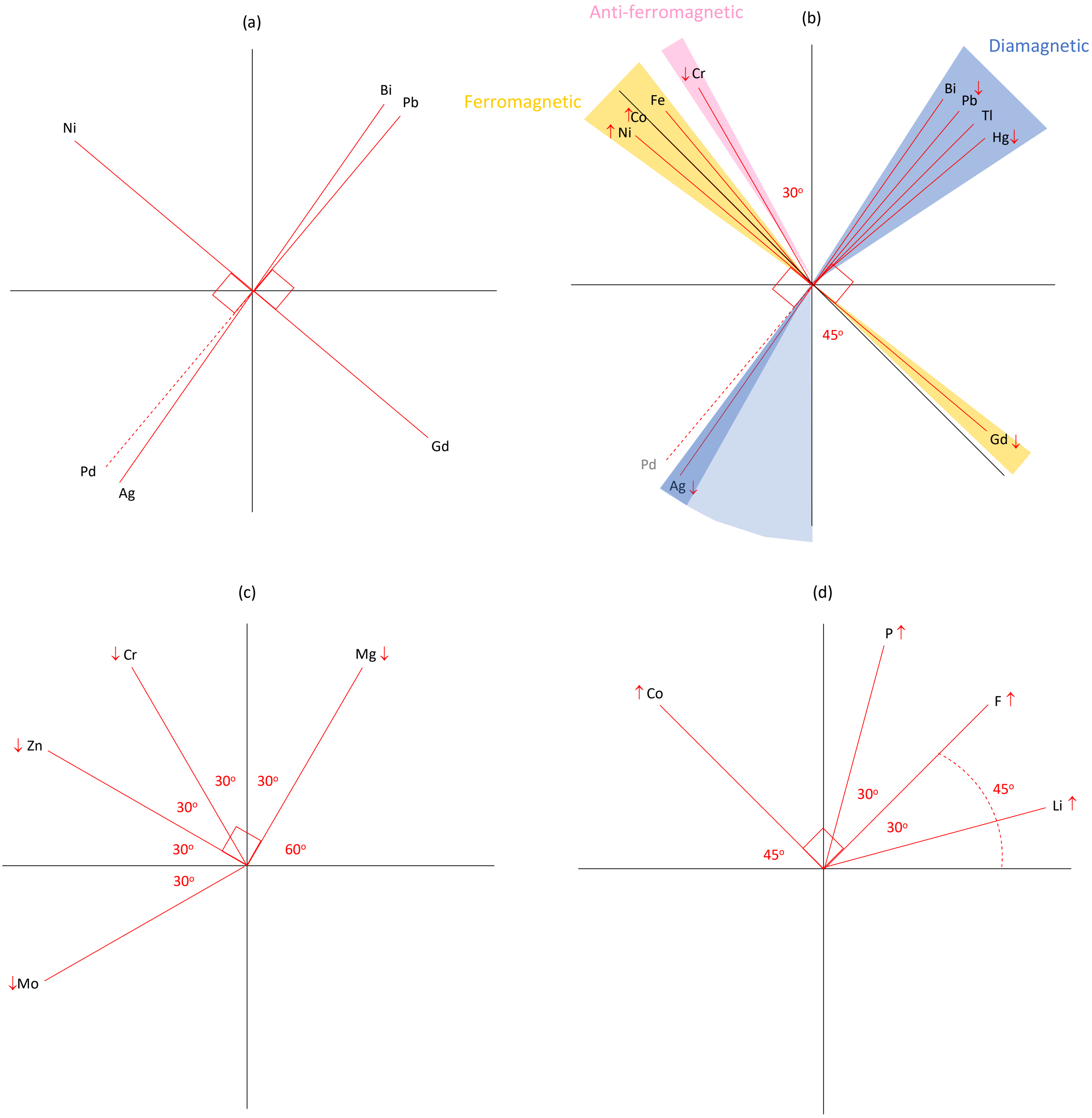

Figure 4: Post quantum treatment phase wheels applying to the Case Study in [2], with radials denoting elements of significance and their associated Δϕ, for Table 2's (a) "largest changing" heavy metals (only), (b) named heavy metals (all), (c) decreasing minerals (all with even *Z*), and (d) increasing minerals (all with odd *Z*). Arrows ↓ and ↑ respectively indicate level decreases and increases, seemingly in response to treatment. See in-text for bases of: Pd inclusion as a dashed radial in (a), and colour cones and feature mineral inclusions in (b). Shown by (e) is the periodic table connectedness of elements in (b).

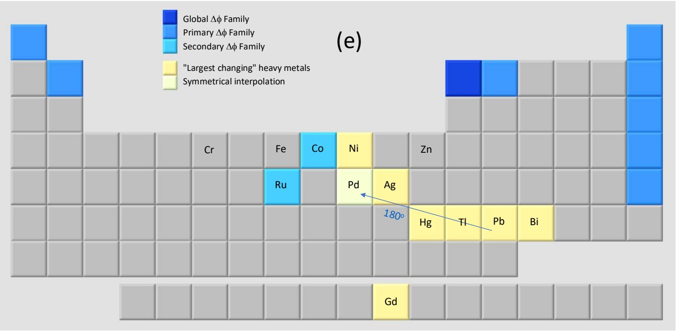

6.2 Symmetrical Geometry of Figures 4a and 4b (Heavy Metals)

It appears from Figure 4a that the removal of the modern ether and its hypothesised neural phase interference facilitates physiological Pb removal, given that the elements of Figure 4a display the largest changes post quantum treatment (Pb reduction being the largest). The striking symmetrical geometry of Figure 4a further strengthens this suggestion of biophysical significance for a facilitated physiological removal process.

This symmetrical geometry of Figure 4a (tentatively assumed to be synergetic) contains the following features: (i) The Pb and Gd radials are perpendicular; (ii) the Pb and Ni radials are perpendicular; (iii) the Ni and Gd radials are antiparallel (separated by 180^o); and (iv) the Ag and Bi radials are antiparallel. Note that Pd, which is not part of diagnostic testing, is included as a dashed radial (antiparallel to Pb) on the tentative assumption that Pd is an element of relevance because of the further symmetry and periodic table connectedness (see Figure 4e) it provides.

The heavy metals of the more inclusive Figure 4b appear connected via their localities within the periodic table (see Figure 4e), as well as by the fact that (except for Ni) they are diamagnetic, with Bi, Hg, Ag and Pb possessing some of the highest magnetic susceptibility magnitudes of the diamagnetic elements. Figure 4b recognises by colour cones an apparent perpendicular connectivity between Table 2's diamagnetic and ferromagnetic elements, as well as cases of approximate antiparallel alignment between similar magnetism types. Note that Figure 4b additionally includes ferromagnetic and anti-ferromagnetic minerals displaying noteworthy percentage changes in [2], namely physiologically relevant Co, Fe and Cr. The noteworthiness in [2] is based on: Co being the mineral with the largest percentage increase; Cr falling in the low minus or "red zone" by the end of the quantum treatment (preliminary) assessment period; and the CFS Case Study subject historically displaying unexpectedly elevated ferritin levels via conventional blood pathology.

Diamagnetism and paramagnetism obviously applies to elements falling outside the colour cones of Figure 4b, however here the intension is to describe the geometry of stand-out elements only. The fact that diamagnetic elements feature for an analysis involving modern ether removal is perhaps not surprising, given that induced effects for diamagnetism are of the *opposing* type (and therefore after removing a source of induction one might expect to see a return towards some homeostasis).

Because the symmetrical geometries of Figures 4a and 4b reflect diamagnetism, ferromagnetism and paramagnetism, results again seem inherently steeped in quantum mechanics (since such magnetism types involve magnetic moments dependent upon electron orbital motion and/or spin, the manner of electron pairing/unpairing, etc.). Hence, ongoing suggestions that $\Delta\phi$ are biophysically meaningful and quantum mechanically-based are further (and in fact quite substantially) supported. Additionally, some *orthogonality* between element-associated neuro-quantum states appears indicated by the described perpendicular geometries (which is again contextually significant for an ever-strengthening case of an underlying quantum basis).

The apparent connectivity of antiparallel elements in Figure 4a (Ni-Gd, Pd-Pb, Ag-Bi), and the 30° and 45° angles made with the primary axes (which associate with some $\Delta\phi$ Families) in Figure 4b, are identified for the continuation of an earlier theme and for scene-setting for forthcoming discussion. Most notably, antiparallel alignment and 45° connectivity feature within heavy metal interference pathways of Section 7, and are quantitatively demonstrated to be meaningful in Section 9.

Figures 4a and 4b also seem to indicate that conventional circular geometry applies for the $\Delta\phi$ analysis of elements, e.g., $\Delta\phi_{Pb} = 410^\circ \equiv 50^\circ$ (on the basis of $410^\circ = 360^\circ + 50^\circ$), which again is revisited within Section 7.

The 5° radial separation in Figure 4b (which expands to 72 elements in a henge-like array via linear mapping for a full phase wheel cycle) suggests that the unit of "degree" is, either by chance or design, biophysically significant in a neuro-quantum sense (thereby explaining why several elements identified in [2] have α values, when expressed in degrees, that are integers or common fractions of integers). This apparent biophysical significance of the 5° minimum separation (with fine structure provided by α) is substantiated in Section 9, however for now the fact that it inherently associates with biologically abundant and fundamentally important H is fitting. Such degree unit insights further support the hypothesis that artificial phase changes within the modern ether might overlap/interfere with those of neural processes. Furthermore, all elements within the just-described expanded 72-element henge-like visualisation may in fact associate with various $\Delta\phi$ Families (but presumably of lesser standing or states of quantum occupancy than the previously identified Primary, Secondary and Global Families).

Finally, it is recognised that some of the symmetry in Figure 4b and in figures to follow, if biophysically meaningful, cannot be strict because of potential external influences and internal limits to change. For example, deliberate or accidental high level ingestion of an element would eventually need to be biologically reflected regardless of any preferred physical symmetry. Hence, exceptions to present or future noted symmetries are expected.

6.3 Symmetrical Geometry of Figures 4c and 4d (Minerals)

The mineral phase wheels of Figures 4c and 4d continue to indicate biophysical significance through in-common features with their heavy metal counterparts (e.g., the demonstration of perpendicular relationships for mineral pairs Zn-Mg and Co-F). Such geometry, together with the figures' $30^{o}/60^{o}$ and $30^{o}/45^{o}$ sector angle symmetries, are quintessentially characteristic, albeit broadly, of quantum mechanics or nature in general (e.g., 60^{o}-based hexagonal symmetry is observed within: elementary particle property organisation of baryon and meson octets, beehive construction, crystal structures including snowflakes and rock formations, shell patterns for some tortoises/turtles, and so on). Note that the Primary $\Delta\phi$ Family-associated elements of C, Ar, Kr and Xe also adhere to the $30^{o}/60^{o}$ symmetry of Figure 4c, while for Figures 4c and 4d combined, radials are separated by 15^{o} in line with a "$\Delta Z = 3$" observation for all feature minerals in [2] and the periodic table $\Delta\phi$ separation for $n = 1$ in (3a).

As per the finalising comment of Subsection 6.2, the ↓ and ↑ symmetry, for even and odd Z elements respectively, is not expected to be strict but nonetheless may suggest the possible effect of an alternating unpaired spin-half electron. The pairing of electrons in the filling of atomic orbitals is obviously more involved (e.g., with respect to determining paramagnetism or diamagnetism across all elements) but the general symmetry comment nonetheless applies. Odd/even symmetry is itself a property of quantum mechanics, and so it is becoming increasingly clear that the quantum mechanical-like findings presented here and in [2] do in fact derive, at least partially, from quantised phenomena such as nuclear spin, electron spin, and/or electron orbital angular momentum.

7. Heavy Metal Interference Pathways

7.1 Overview

This Section, which identifies possible heavy metal neural interference pathways, represents a primary culmination of the report and mostly follows from the forbearer paper [1], with aspects of [2] and other available evidence playing supporting roles.

The hypothesis from [2] that the modern ether might interfere with $\Delta\phi$ and/or α of neural signalling, particularly in relation to CFS, has already been summarised. While the preliminary results of [2] appear supportive of this hypothesis, the phase wheel symmetries of the previous Section may additionally indicate a heavy metal presence within such a CFS mechanism. Hence, this Section extends phase wheel analysis with a focus on possible neural interface pathways for the heavy metals that: (i) present with relatively high levels for the CFS Case Study subject; (ii) are generally of particular societal environmental concern; and/or (iii) have a "largest changing" feature role within Table 2. The heavy metals subsequently selected for extended analysis are As, Ba, Bi, Cd, Hg, Pb and Tl.

For the CFS Case Study subject and based on the constituent Oligoscans[1] of [2], As, Ba, Bi, Cd, Hg and Pb all present within the high minus to high plus range (inclusively), while Tl presents in the normal range. Cd and Hg are the heavy metals with the two highest relative levels[2], which is consistently the case for four such diagnostic scans taken across an extended period (> 12 months). Pathology results for a provocative chelation test[1] (that induces heavy metal mobilisation by intravenous aminopolycarboxylic acid administration allowing for in-urine detection pre- and post-administration), were acquired (see Figure 5) for the Case Study subject two weeks prior to the first Oligoscan, but not presented in [2].

For provocative chelation, As and Cd display a free presence pre-test, and As, Cd, Hg and Pb display observable (without being excessive) mobilisations post-test. It is the position of this report that the Oligoscan and provocative chelation results are not necessarily expected to yield equivalency (and are indicatively useful even if efficaciously limited). As will be explained as the report develops, a heavy metal presence, and not necessarily levels of excess, is considered a key element of the above hypothesis (though one would naturally expect excessive levels to be associated with increased contextual risk or relevancy).

---

[1] See [2] for its position on Oligoscan efficacy. The efficacy of provocative chelation testing is contentious or not universally accepted.

[2] Heavy metals are only briefly addressed within an Appendix of [2] which indicates Cd and Pb as presenting with the highest relative levels. However, this paired distinction actually belongs to Cd and Hg, with clarification here having no bearing on previous or ongoing discussions.

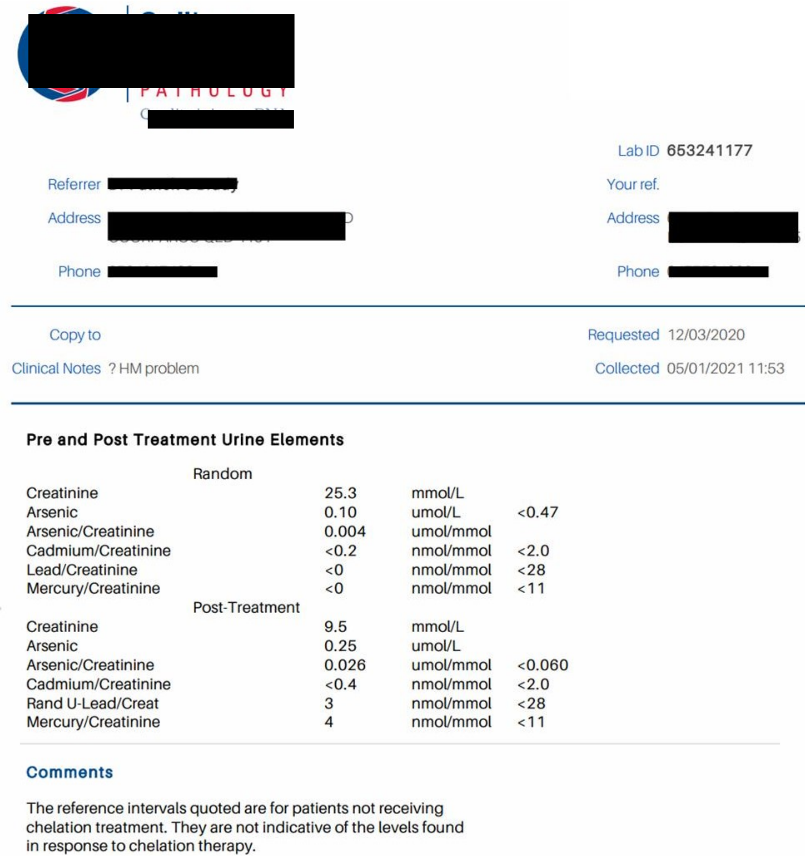

[redacted]

[redacted]

Lab ID **653241177**

Referrer [redacted]
Address [redacted]
Phone [redacted]

Your ref.
Address [redacted]
Phone [redacted]

Copy to

Requested 12/03/2020

Clinical Notes ? HM problem

Collected 05/01/2021 11:53

Pre and Post Treatment Urine Elements

Random			
Creatinine	25.3	mmol/L	
Arsenic	0.10	umol/L	<0.47
Arsenic/Creatinine	0.004	umol/mmol	
Cadmium/Creatinine	<0.2	nmol/mmol	<2.0
Lead/Creatinine	<0	nmol/mmol	<28
Mercury/Creatinine	<0	nmol/mmol	<11
Post-Treatment			
Creatinine	9.5	mmol/L	
Arsenic	0.25	umol/L	
Arsenic/Creatinine	0.026	umol/mmol	<0.060
Cadmium/Creatinine	<0.4	nmol/mmol	<2.0
Rand U-Lead/Creat	3	nmol/mmol	<28
Mercury/Creatinine	4	nmol/mmol	<11

Comments

The reference intervals quoted are for patients not receiving chelation treatment. They are not indicative of the levels found in response to chelation therapy.

Figure 5: Provocative heavy metal chelation test results for the CFS Case Study subject of [2].

Six phase wheels for Hg, Cd, Ba/Bi (combined), As, Pb and Tl, indicating possible physiological relevance in the form of neural interference pathways on the basis of connectivities involving key minerals, are respectively given by Figures 6a to 6f and shortly discussed in turn.

Perpendicular, parallel and antiparallel symmetrical geometries and alignments are of particular interest within Figures 6a to 6f, in line with discussions of the previous Section. Cases of parallel alignment between a heavy metal and mineral are considered suggestive, for element-associated neuro-quantum states, of a potential for $\Delta\phi$ distinguishability corruption (due to interference or lost acuity at the α level). Antiparallel alignment is also considered suggestive of a potential for distinguishability corruption on the basis of α conceivably providing uniqueness for 180° symmetry, or on the basis of inherent connectedness which is supported by Section 9.

An intriguing theorised perspective for some antiparallel alignments is their reflection of a potential for the brain to function in some higher adverse neuro-quantum energy state. Such function might subsequently cause usually separated states to overlap and interfere (within the Case Study of [2] the subject's complete mineral profile is essentially the reverse of what might be considered a typical healthy profile, and so perhaps this reversal carries significance beyond the purely biological). Several such antiparallel alignments occur within the heavy metal-specific phase wheels of Figures 6a to 6f, however the collective interference case made by these phase wheels does not rely on this intriguing theorised perspective.

The phase wheels of Figures 6a to 6f also identify key elements that display some form of 45° symmetrical connectivity, continuing an on-going contextual interest of the report (e.g., see Subsection 4.1) but with recognition that $\Delta\phi = 45^{\circ}$ represents just one of several geometrical connectivities with expected biophysical significance and is therefore not essential for the establishment of interference pathways. Nonetheless for the continuity reason stated, and also because of extra meaningfulness to be demonstrated later in Section 9, $\Delta\phi = 45^{\circ}$ connectivities and the interference pathway support they offer are worthy here of brief notation and consideration.

Finally, for the following phase wheel discussions "metabolism" is used as a generic term due to the report's mathematical/physical basis. That is, the physiologies of mineral-related functional processes involving: catalysation of enzyme systems, cell channel gating, ion transport, metabolism regulation, neurotransmitter messaging, receptor roles, etc., are sophisticated and beyond the scope or need of this report. Hence, for identified interference pathways any generic comment of there being potential for *mineral metabolism interference* takes into account any or all such process aspects.

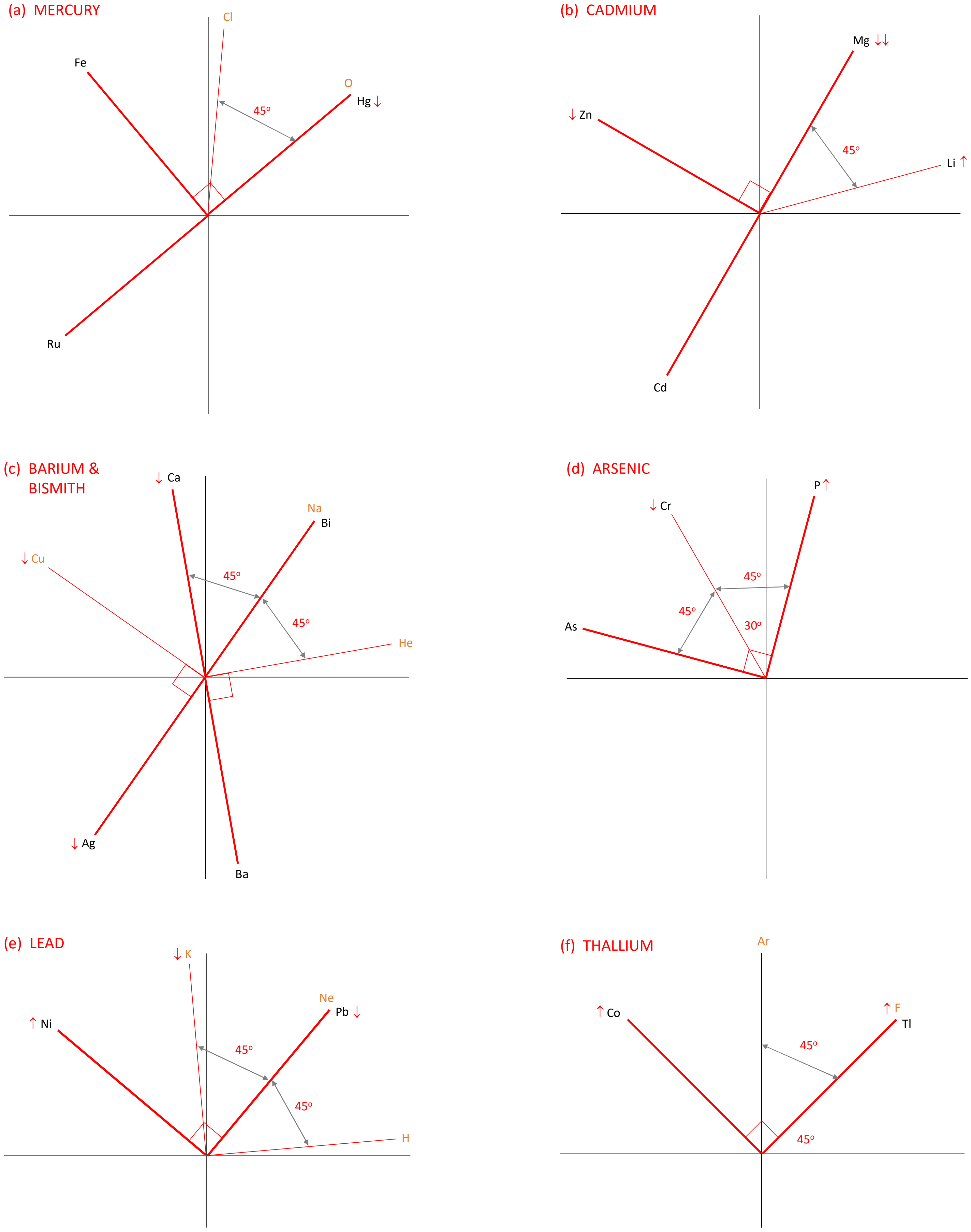

Figure 6: Phase wheels proposing heavy metal neuro-quantum interference pathways, and which include minerals of physiological interest (including from the Case Study of [2]) that contribute to geometrical symmetry or connectivity, for (a) Hg, (b) Cd, (c) Ba & Bi, (d) As, (e) Pb, and (f) Tl.

Note that phase wheel discussions to follow are primarily based on the $\Delta\phi$ Family analysis and subsequent $Z \leftrightarrow \Delta\phi$ synergetic approach from [1]. Where mineral and heavy metal results are used for discussion support, they apply to those of [2] (and so Table 2). Accordingly, the heavy metal provocative chelation results of Figure 5, which are unreported in [2], are specifically identified as required throughout discussions.

7.2 Mercury Phase Wheel (Figure 6a)

The parallel alignment between Hg and O may reflect a potential for interference to O-associated neuro-quantum signalling (and so to O metabolism and overall oxygenation), especially given the high plus Hg level within the CFS Case Study. Potential for interference is also reflected by the antiparallel Hg-Ru alignment, and perpendicular Hg-Fe symmetry.

As per Subsection 4.2, collective connectivity for the pathway is heightened by the facts that: (i) Ru is associated with a Secondary $\Delta\phi$ Family; (ii) Ru proceeds Fe in Group 8 of the periodic table; (iii) Ru is diagonally adjacent to Co in the periodic table; (iv) Co associates with another Secondary $\Delta\phi$ Family; (v) Co is the largest increasing mineral in apparent response to quantum treatment; and (vi) Co, in the form of vitamin B12, is central to the production of Fe-containing/O-carrying haemoglobin.

The CFS Case Study subject has historically displayed unexpectedly elevated ferritin levels with no supplement intake. More specifically, ferritin levels by conventional blood pathology for Nov 2015, Dec 2015, Jan 2020 and Aug 2022 are 354, 327, 349 and 304 $\mu g \cdot L^{-1}$ respectively, with the typical population upper level being 300 – 320 $\mu g \cdot L^{-1}$. Hence, the most recent Aug 2022 result[3] possibly indicates ferritin level reduction in response to quantum treatment lessening the effect of Hg interference within the described pathway. The no detectable provocative chelation pre-test reading for Hg/creatinine versus its post-test (mobilised) reading (Figure 5) for the CFS Case Study subject, also supports the potential for a dynamic Hg *presence* playing a CFS attributional role via the described interference pathway.

---

[3] Sullivan Nicolaides laboratory reference number 669012536-H-H900. See [2] for the identification numbers of past ferritin tests and an additional Dec 2015 PCR test for hereditary haemochromatosis gene (being negative with C282Y, H63D, S65C mutations not detected).

The displayed 45° symmetrical connectivity may also suggest the possibility of interference to Cl metabolism, including action potential cellular hyperpolarisation.

Thus, the symmetrical functional geometries of the Figure 6a phase wheel suggest that Hg has the capacity to disrupt the neuro-quantum signalling of physiological processes, especially those involving Fe metabolism and associated blood oxygenation.

7.3 Cadmium Phase Wheel (Figure 6b)

The antiparallel alignment between Cd and Mg may reflect a potential for interference to Mg-associated neuro-quantum signalling (and so to Mg metabolism), especially given the high plus Cd level within the CFS Case Study. This interference potential is supported by the substantial −40.8% reduction in Mg post quantum treatment (possibly suggesting interference reduction via modern ether removal and the opening of Mg channels despite a somewhat depleted reservoir).

Note that the CFS Case Study subject had previously been diagnosed (by an "ahead-of-its-time" University of Newcastle, Australia commercial laboratory service) with a 10/10 rating for fibrillar catabolism, plus high and low excretion levels for citric and succinic acids respectively, possibly indicative of Krebs cycle disturbance and carrying implications for adverse muscular effects including Mg removal. Hence, the phase wheel symmetries here appear to provide another perspective on accepted physiological interference pathways associated with the displacement of essential cations in such circumstances.

Similarly, the Cd-Zn and Mg-Zn perpendicular symmetries in Figure 6b, and the neuro-quantum interferences these might bring, may explain why Zn metabolism is compromised for the CFS Case Study subject, as indicated by the subject's appreciably low Zn levels. The slight further reduction in Zn levels, into the low minus or "red zone", in apparent response to quantum treatment, may, as for Mg, reflect interference reduction, especially given the significant qualitative feelings of muscular improvement reported by the subject.

The detectable provocative chelation pre-test reading for Cd/creatinine versus its post-test mobilisation increase of approximately 100% (Figure 5), supports the dynamic *presence* of Cd and it potentially playing a CFS attributional role via the described interference pathway for the Case Study subject.

The 45° connectivity with Li (that has key neurological roles as identified in [2]), and it being the mineral with the second largest percentage increase in apparent response to quantum treatment, are noted. The 30°/60° symmetry exhibited between Li and minerals such as P within Figure 4d might also indirectly suggest potential for Cd interference towards these minerals' metabolisms (recall P's consistent low minus level for the CFS Case Study subject). However, a more direct pathway to P interference involving As is identified in Subsection 7.5.

Thus, the symmetrical functional geometries of the Figure 6b phase wheel suggest that Cd has the capacity to interfere with Mg and Zn neuro-quantum signalling, and so disrupt Mg and Zn metabolism.

7.4 Barium/Bismuth Phase Wheel (Figure 6c)

The antiparallel alignment between Ba and Ca may reflect a potential for interference to Ca-associated neuro-quantum signalling (and so to Ca metabolism), especially given the high Ba level within the CFS Case Study. This overlap in particular indicates physiological relevancy due to Ca's critical muscle contraction and action potential functional roles involving ion transport channel and neurotransmitter regulation.

The parallel alignment between Na and Bi, and antiparallel alignment between Na and Ag (Ag being the heavy metal with the second largest percentage decrease in apparent response to quantum treatment), suggest similar physiological relevancy (neuro-quantum interference potential), especially given the 45° connectivity between Ca and the Ag-Na/Bi "meridian", and the fact that Na is the most important element of the action potential.

Ca is one of the few minerals initially in the high normal range prior to quantum treatment for the CFS Case Study subject. The appreciable post-treatment decrease of Ca (−14.8%) may therefore suggest some degree of effective interference reduction and subsequent opening of ion transport channels in response to quantum treatment.

The perpendicular symmetry between Cu and the Ag-Na/Bi meridian may also carry indirect physiological significance given that excess Cu can displace essential minerals of the same divalency such as Zn, and the high/high plus Bi level within the CFS Case Study.

The 45° connectivity with He is noted because He is associated with a Primary $\Delta\phi$ Family in [1]. While noble gases are thought not to play significant physiological roles, their strong representation within Primary $\Delta\phi$ Family members, together with connectivities like that just identified, encourages the rethinking of this conventional non-participant status (this rethinking is briefly undertaken in Subsection 10.2).

Thus, the symmetrical functional geometries of the Figure 6c phase wheel suggest that Ba and Bi, in isolation or in combination, have the capacity to disrupt neuro-quantum signalling for Ca and Na metabolism, in turn offering an alternative perspective on how heavy metals have the capacity to adversely affect the physiologies of ion transport. Since such ion transport disruption capacities for Ba and Bi are perhaps relatively lesser known, one noteworthy example is extracellular Ba's targeting of K inward rectifier channels, which are involved in many physiological processes and are highly expressed in all muscle types, with this targeting ultimately affecting K conductivity [7].

7.5 Arsenic Phase Wheel (Figure 6d)

The perpendicular symmetry between As and P may reflect a potential for interference to P-associated neuro-quantum signalling (and so to P metabolism), especially given the high minus As level within the CFS Case Study. This potential interference is supported by P being the only mineral at a low minus level across all four diagnostic scans for the CFS Case Study subject (and so indicative of impaired oxidative phosphorylation for the subject), and also by P displaying the third largest percentage increase of all minerals in apparent response to quantum treatment.

The detectable provocative chelation pre-test readings for As and As/creatinine versus their post-test mobilisation increases of 150% and 550% respectively (Figure 5), supports the dynamic *presence* of As and it potentially playing a CFS attributional role via the described interference pathway for the Case Study subject.

Noting again that Co displays the largest percentage increase for minerals in apparent response to quantum treatment, the 60° connectivity between P and Co (Figure 4d) may suggest potential for indirect Co interference by As (see Figures 6a and 6f for more direct Co interference pathways). The displayed 45° symmetrical connectivity with "red zone"-associated Cr (see Table 2) is also noted.

Thus, the symmetrical functional geometries of the Figure 6d phase wheel suggest that As has the capacity to disrupt neuro-quantum signalling for P metabolism.

7.6 Lead Phase Wheel (Figure 6e)

The perpendicular symmetry between Pb and Ni may reflect a potential for interference to Ni-associated neuro-quantum signalling (and so to Ni metabolism which as previously raised can indirectly affect Zn metabolism), especially given the high minus/high Pb level within the CFS Case Study. This potential interference appears to be supported by Ni and Pb respectively displaying the largest percentage increase and decrease of all heavy metals in apparent response to quantum treatment.

The no detectable provocative chelation pre-test reading for Pb/creatinine versus its modest post-test (mobilised) reading (Figure 5), supports the potential for a dynamic Pb *presence* playing a CFS attributional role via the described interference pathway for the Case Study subject.

The 45° symmetrical connectivity with K may suggest a possible interference pathway for K metabolism, especially given K's important (Na-following) role in the action potential. The parallel alignment between Pb and Ne, and the 45° symmetry with H, are also potentially collectively meaningful due to the association of Ne and H with Primary $\Delta\phi$ Families, as discussed further in Subsection 10.2.

Thus, the symmetrical functional geometries of the Figure 6e phase wheel suggest that Pb has the capacity to disrupt neuro-quantum signalling for Ni and K metabolism.

7.7 Thallium Phase Wheel (Figure 6f)

The perpendicular symmetry between Tl and Co (the latter associating with a Secondary $\Delta\phi$ Family) may reflect a potential for interference to Co-associated neuro-quantum signalling (and so to Co metabolism). This potential interference is supported by Co displaying the largest percentage increase of all minerals in apparent response to quantum treatment. Likewise, the parallel alignment between Tl and F may reflect a potential interference pathway for F metabolism, F displaying the fourth largest percentage increase of all minerals in apparent response to quantum treatment. This alignment in turn brings 30° symmetrical connectivity to P and Li in accordance with Figure 4d. The 45°

symmetrical connectivity with Ar (noble gas associated with a Primary Δϕ Family) is again raised for Subsection 10.2 discussion.

Thus, the symmetrical functional geometries of the Figure 6f phase wheel suggest that Tl has the capacity to disrupt neuro-quantum signalling for Co and F metabolism.

7.8 Summary of Heavy Metal Interference Pathways

In summary, the identified heavy metal (As, Ba, Bi, Cd, Hg, Pb and Tl) interference pathways of Figures 6a to 6f offer explanatory mechanisms for:

- Ca metabolism impairment (Figure 6c).
- Co and Fe metabolism impairments, oxygenation impairment, red blood cell (RBC) deformation/impairment (Figure 6a, Figure 6f, Subsection 10.2).
- Mg metabolism impairment (Figure 6b).
- Ni metabolism impairment (Figure 6e).
- P metabolism impairment including to oxidative phosphorylation (Figure 6d).
- Zn metabolism impairment (Figure 6b, and indirectly via Figure 6e).
- Multisystem complexity in general, arising from the heavy metal interference pathways of Figures 6a to 6f combined and their varying degrees of potential impact on any given individual. This complexity includes potential for Cl, Li, Na, Cr and K metabolism impairments, via $\Delta\phi = 45^{\circ}$ connectivities, within Figures 6a, 6b, 6c, 6d and 6e respectively.

It is timely to also recall that a component of the above hypothesised mechanisms is the interference to electromagnetically relevant/susceptible elements by the modern ether resulting in lost Δϕ and α acuity, as raised in [2] and further supported by this report.

8. CFS Unification and Extension to Other Illnesses

8.1 The Unification of CFS Studies

Several pathologies or dysfunctions are found in CFS, some of these are summarised in [2] and include: adverse neurological effects such as brain damage; functional and inflammatory changes in the brain; RBC deformation; poor microcirculation; mitochondria dysfunction leading to adenosine triphosphate (ATP) production impairment; and immune system impairment or hyper-responsiveness. Studies of such pathologies or dysfunctions have all made, and continue to make, valuable contributions to the scientific understanding of CFS and its multisystem complexity. However, despite fresh announcements of breakthroughs that further CFS understanding, a confounding complexity, particularly in relation to CFS's multisystem nature, is still clearly present as per the following select (from several similarly-themed) media examples:

A recent Australian media article (Courier Mail, June 23, 2022 under the banner *Hope for Chronic Fatigue Research: Addiction Drug is the Key*) reports that a researcher at a leading Queensland university discovered the cause of CFS in 2017 (that being, a family of dysfunctional receptors leading to hindered Ca transport). The related research also points to drugs used to treat opioid and alcohol addiction as being helpful in low doses for CFS (though as indicated in the article and elsewhere such existing drugs, e.g., naltrexone, are far from a cure or helpful for everyone). An update article (News Corp Australia Network Online, August 11, 2022 under the banner *Game-Changing New Test and Treatment for Long Covid*) additionally confirms sameness between CFS and long Covid fatigue.

Highlighting the complex interdependencies of CFS is another recent but contrasting Australian media article (Daily Telegraph Online, June 18, 2022 under the banner *Australian Researchers Finds Long Covid Causes Brain Damage, Point to a Cure*) reporting the breakthrough that a neurologist from a leading New South Wales hospital has identified a nerve toxin behind brain fog and cognitive impairment in long Covid. The article goes on to report that *some* subjects have cognitive issues linked to the kynurenine pathway which normally provides the body with energy, balances mood, and dampens the immune system when excessively activated by infection (ineffective dampening may lead to enhanced levels of the chemicals quinolinic acid and 3 hyrdroxyanthranilic acid which can induce nerve cell injury or death). The article also reports that the finding opens the way for trials of potential treatments (including the use of existing drugs used for treating epilepsy and cancer) and potential blood test-based biomarkers.

The above June to August 2022 media reports undoubtedly represent significant contributions to CFS science. However, the differences between, and challenges underscored by, the reports (e.g., the range and effectiveness of different existing drugs being considered for trial, the need to develop new drugs, differing causal and cure bases/indicators, etc.) further highlight:

- the multisystem complexities and interdependencies of CFS,
- the fact that a complete unified explanation that links all CFS pathology and dysfunction findings to date is yet to emerge, and
- the absence of a CFS cure.

This report aspires to offer such unification since the notion of modern ether interference, combined with heavy metal neuro-quantum signalling corruption, can potentially manifest in a multitude of ways for a susceptible individual depending on factors such as:

- which heavy metal interference pathways (Figures 6a to 6f) are in play, and to what extent, based on the individual's exposures and predispositions (including generally to CFS onset agents such as viruses), and
- the individual's neuro-quantum signalling resilience and accommodation ability towards a local modern ether.

The presented notion is also complementary to many existing CFS studies by its identification of mechanisms leading to multiple system impairments, as per the multiple heavy metal interference pathways summarised by Subsection 7.8.

Further complementarity arises from the fact that every individual has some unavoidable degree of heavy metal exposure and system accumulation. For example, large-city evidence (from London) suggests that historical environmental Pb deposits of the 20th century, especially from leaded petrol, continue to impact today's urban atmosphere, despite the banning of leaded petrol around the turn of the century. This long-term Pb persistence, due to various remobilisation mechanisms, has resulted in baseline Pb levels that are difficult to further decrease [8]. Thus, from the above and other pollution sources, Pb continues to present an environmental health threat, entering the body through food and fluid intake, but also through inhalation (e.g., of lead oxide nanoparticles). For the latter source, a recent study shows that the sub-chronic inhalation of lead oxide nanoparticles may result in their broad distribution throughout organs and their tissue-specific subcellular localisation [9].

Because Pb contamination is so widespread, it could via Figure 6e be a leading heavy metal contributor to CFS. However, startling population exposure scenarios can be summarised for most of the heavy metals considered by this report and, in any event, the manner in which CFS presents within the wider population may suggest that a heavy metal biological presence does not need to be obviously high to facilitate CFS onset. Viz., just a modest presence could, in the "right" circumstances, trigger adverse neuro-quantum effects as described by this report. Hence as widely suggested elsewhere, but from a unique perspective, this report supports the prudent reduction of heavy metal exposure and accumulation for the benefit of wider population health.

8.2 Extension to Other Neurological and/or Hyperimmune Illnesses

Cautious consideration might also be given to extending report concepts to other neurological or hyperimmune illnesses (with extension potentially even overlapping with autoimmune illness), in which case it is prudent to impress that many such illnesses have been known since pre modern ether times and/or have proven genetic predispositions, and so on. Hence, any adverse neuro-quantum considerations extended to other illnesses should be made within a *risk factor*, rather than primary cause, context. With this provision in mind, some cautious extended considerations are as follows:

Within [2] several elements are tabulated on the basis of having α values that, when expressed in degrees, approximate as integers or integer multiples of ⅓ or ¼ (to within ± 0.5%). The tabulation is replicated here by Table 3. Minerals which feature in Table 3 and which are noteworthy in [2] due to their low absolute level, or marked level change in response to the applied quantum treatment, include F, P, and Zn. Of these minerals, P is the most focused upon in [2] because of its low minus or "red zone" level across all diagnostic tests and the fact that impaired oxidative phosphorylation is seen in CFS [10].

It is rationalised in [2] that an element's inclusion in Table 3 is suggestive of an increased risk of modern ether interference to the neuro-quantum signalling associated with that element. This rationalisation appears further supported by the henge-like geometrical arrangements of recently discussed phase wheels for which element-associated radials are minimally separated by $\Delta Z = 1$ or 5^{o} (i.e., an integer amount of degrees, implying that such amounts carry biophysical significance, and see Section 9 for apparent confirmation of this significance). The dual featuring of Cu, Pd and Ba in Table 3 and in select phase wheels, namely Figure 4a (Pd) and Figure 6c (Cu and Ba, with Ca antiparallel to Ba), also potentially support the above rationalisation.

Z	Element	$\Delta\phi$ (degrees)	Model $\bar{\alpha}_{\Delta\phi}$ (degrees)	± (degrees)	Nominal $\bar{\alpha}_{\Delta\phi}$ (degrees)	Deviation (%)
9	F	45	0.2510	0.0075	¼	0.40
15	P	75	0.6631	0.0121	⅔	-0.53
18	Ar	90	1.0026	0.0148	1	0.26
29	Cu	145	3.0087	0.0265	3	0.29
30	Zn	150	3.2504	0.0277	3¼	0.012
31	Ga	155	3.5020	0.0289	3½	0.057
46	Pd	230	8.4619	0.4484	8½	-0.45
53	I	265	11.5377	0.3281	11½	0.33
54	Xe	270	12.0167	0.1391	12	0.14
55	Cs	275	12.5055	0.0442	12½	0.044
56	Ba	280	13.0042	0.0327	13	0.033
57	La	285	13.5129	0.0952	13½	0.095
58	Ce	290	14.0314	0.2239	14	0.22

Table 3: Taken from [2], $\Delta\phi$ and corresponding median $\alpha_{\Delta\phi}$ values ($\bar{\alpha}_{\Delta\phi}$) predicted by reverse mapping of elements from $Z = 1$ to 63 and for which these generated $\bar{\alpha}_{\Delta\phi}$ values fall within 0.5% of some integer, or integer multiple of a fraction (⅓ or ¼), when expressed in units of degrees. Uncertainties are stated at 95% CI, and see [2] for the subtle distinction between its "non-residual" $\bar{\alpha}_{\Delta\phi}$ modelling approach versus the high precision approach of [1].

As raised by this Subsection's opening paragraph, the inclusion of a not-yet-considered element from Table 3 (e.g., I) might then be seen as a risk factor (only) for illnesses where the metabolism of that element plays a key role. However, interference to neuro-quantum signalling as proposed by this report and in [2] is certainly not restricted to the elements of Table 3 (which happens to also contain several mathematics-in-nature observations[4]).

---

[4] It is mathematically interesting in Table 3 that $\alpha_{Ba} = 13.00^{o}$ (a prime and Fibonacci number), and that nominal α values for Zn, Pd and I form ratios of prime and/or Fibonacci numbers: $\alpha_{Pd}:\alpha_{I} = 17:23$ and $\alpha_{Zn}:\alpha_{Pd} = 13:34$. Of final Fibonacci interest is that two cycles of the 72-element henge-like visualisation contain 144 elements (despite the periodic table not yet extending to this number of elements). While Fibonacci numbers are often observed in nature, *relatively* larger numbers such as 144 are less common.

9. The Quantum Basis of Brain Henge

9.1 Quantisation by $\Delta\phi_{min}$

There are various indications throughout this report of the degree unit holding physical significance within the *symmetrical functional geometries of neuro-quantum states*, from this point generically coined "Brain Henge". Prominent significance indicators include: (i) the collective symmetrical geometries of all presented phase wheels which inherently increment by $Z = 1$ and therefore by a minimum of $\Delta\phi_{\mathrm{min}} = 5^{\mathrm{o}}$ (i.e., an integer amount of degrees) in accordance with applied linear mapping; (ii) the fact that $\Delta\phi_{\mathrm{min}} = 5^{\mathrm{o}}$ inherently associates with biologically abundant and fundamentally important H; (iii) the several feature elements with integer or fractional integer values for α when expressed in degrees, as per Table 3; and (iv) the near-integer form of the degree-based (1b).

What then might be the quantum basis for $\Delta\phi_{\mathrm{min}} = 5^{\mathrm{o}}$? The answer appears to lie with the forms of (3a) to (3c) and their quantisation in $2n^2$ (that naturally also reflect the degeneracy of the principal energy levels of hydrogen). From this quantisation form it can be reasoned that it is not so much 5^{o} that is significant, but rather it is the angular amount associated with $n_e = 6$ for:

$$\Delta\phi_{n_e} = \frac{360^0}{2n_e^2} = \frac{180^0}{n_e^2} \ (\text{degrees}) \qquad \text{or} \qquad \Delta\phi_{n_e} = \frac{2\pi}{2n_e^2} = \frac{\pi}{n_e^2} \ (\text{radians}), \qquad (4)$$

where $n_e = 1$ to 6 is a proposed principal Brain Henge quantum number. The quantisation of (4) is thus Brain Henge-focused, while that of (3a) to (3c) is periodic table-focused, though association between the quantisations naturally exists despite the different foci. Given that groupings of six are common in elementary particle and atomic physics[5], it is perhaps fitting in (4) that $\Delta\phi_6$ corresponds to $\Delta\phi_{\mathrm{min}}$. Furthermore, the set of $n_e = 6$ (lowest state) to 1 (highest state), which could alternatively be written $n_e' = 1$ (lowest state) to 6 (highest state) where $n_e' = 7 - n_e$, will be complemented by another (related) quantum number set of similar size within Subsections 9.2 and 9.3.

It is subsequently indicated by (4) that $\Delta\phi_{n_e} = 180^{\mathrm{o}}$, 45^{o}, 20^{o}, 11.25^{o} and 7.2^{o}, for $n_e = 1, 2, 3, 4$ and 5 respectively, with $\Delta\phi_1 = 180^{\mathrm{o}}$ and $\Delta\phi_2 = 45^{\mathrm{o}}$, together with the strong

---

[5] For example, six leptons including the electron, six quarks, hexagonal elementary particle property arrangements, six natural noble gases with the largest reaching the sixth principal energy level such that subshells below the *s*-subshell are fully occupied, and so on.

180° (antiparallel) and 45° connectivities between key elements in most presented phase wheels, seemingly confirming the biophysical meaningfulness of (4). The $\Delta\phi_1 = 180^\circ$ case may additionally support the intriguing theorised perspective for antiparallel alignment raised in Section 7, in turn indicating some mutuality between opposing neuro-quantum states on the same Brain Henge meridian.

Further to the above meaningfulness, $\Delta\phi_3 = 20^\circ$ $(\pi/3^2)$ corresponds to a Primary $\Delta\phi$ Family, while several examples exist of how the six $\Delta\phi_{n_e}$ may linearly combine or "superimpose" to give the $\Delta\phi$ of Primary, Secondary or Global $\Delta\phi$ Families (e.g., $\Delta\phi_1 - \Delta\phi_2 = 180^\circ - 45^\circ = 135^\circ$ gives $\Delta\phi$ for the Secondary Family associated with Co). Phase amounts such as $\Delta\phi_4 = 11.25^\circ$ $(\pi/4^2)$ and $\Delta\phi_5 = 7.2^\circ$ $(\pi/5^2)$ have yet to be considered by analysis like that in [1], but it is anticipated that these phase amounts will provide further meaningfulness in the fullness of time.

9.2 The Radius-of-Thought

This and the following Subsection increase in hypothetical standing, and the report's identified heavy metal neuro-quantum interference pathways are not contingent on their deliberations. Nonetheless, the Subsections offer intrigue and possibly profound insight into select fundamental physics phenomena and their associated quantities.

There are various indications throughout this report of an electron spin effect within Brain Henge. Two such prominent indicators are: (i) the arrangement of Brain Henge based on element magnetism type as demonstrated by Figure 4b; and (ii) the even/odd Z symmetry of Figures 4c and 4d. Because Brain Henge increments by $Z = 1$, and so from (4) by $\Delta\phi_{\min} = \Delta\phi_6 = \pi/6^2$, attention is now directed towards this quantum amount with the intention of identifying a quantifiable association with the electron and possibly its spin.

Consider the hypothetical (abstract) quantised Brain Henge sector of Figure 7:

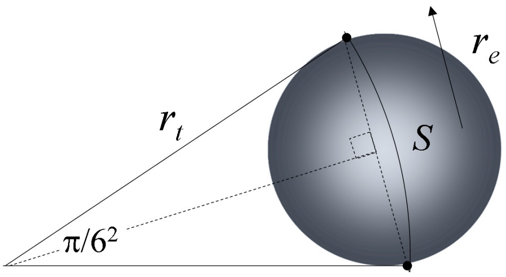

Figure 7: Hypothetical geometry for a minimal sector ($Z = 1$ increment) of Brain Henge. An electron of classical radius, r_e, and inherent spin angular momentum, S, are shown in relation to the sector radius, here coined the "radius-of-thought", r_t.

Figure 7 assumes that the displacement between circumference points for $\Delta\phi_{\min} = \pi/6^2$ effectively equals the classical electron diameter, $d_e = 2r_e$, where the electron radius of $r_e = 2.8179403 \times 10^{-15}$ m is given by equating electrostatic self energy to rest energy[6]. From the geometry of Figure 7, the hypothetical Brain Henge radius, or "radius-of-thought", r_t, is determined via rudimentary trigonometry:

$$r_t = r_e / \sin(\tfrac{1}{2}\pi/6^2)\,. \tag{5}$$

From (5) it is revealed that $r_t = 6.4602931 \times 10^{-14}$ m, with the small angle approximation of $\sin(\tfrac{1}{2}\pi/6^2) \approx \tfrac{1}{2}\pi/6^2$ providing a similar r_t value as expected. Interesting is the numerical outcome from (5) that, to within 0.076% alignment:

$$\sqrt{\frac{\lambda_c}{d_t}} = \frac{\sqrt{3}}{2} n_c\,, \tag{6a}$$

where $\lambda_c = h/m_e c$ is electron Compton wavelength, h is Planck's constant, m_e is electron mass, c is the speed of light, $d_t = 2r_t$ is the "diameter-of-thought", and $n_c = 5$ is a tentatively assumed quantum number for some to-be-explained quantisation with Compton connectedness. Alternatively, (6a) may be expressed as:

$$\sqrt{\frac{1}{D_t}} = \frac{\sqrt{3}}{2} n_c\,, \tag{6b}$$

where $D_t = d_t/\lambda_c$ is the normalised diameter-of-thought in terms of an equivalent number of λ_c (and therefore is dimensionless). Naturally, (6b) could also be expressed in terms of some normalised line frequency, $F_t = 1/D_t$, such that $\sqrt{F_t} = \frac{\sqrt{3}}{2} n_c$. A multiplicative factor of 1.0007634 applied to the right-hand-side of (6a) or (6b) brings about exact alignment. However, exactness is not necessarily an ideal quantum mechanical requirement, with for example the Dirac electron spin g-factor of $g = 2$ once being modified by quantum electrodynamics to $g = 2.0023192$ (0.12% alignment).

---

[6] The stated (current popular) value of $r_e = e^2/4\pi\varepsilon_o m_e c^2$ is near twice $r_e = 1.4093401 \times 10^{-15}$ m previously used within some physics quarters (see in [3] for citation details), with the factored "older value" yielding even closer alignment of within 0.063% in (6a). The ½ factor differential is largely academic, since classical/semi-classical approaches within quantum physics are primarily for guiding complementary perspectives, and for the electron in particular depend on physical visualisations that are inherently uncertain. Furthermore, quantum mechanically r_e is meaningless since an electron is considered a point charge (and while not necessarily applicable here, quantum mechanics has a tendency to place aside or imply certain factors for expediency).

One of the most profound, if not *the* most profound of, physics equations (even ahead of $E=mc^2$), is that for intrinsic electron spin angular momentum, $S=\frac{\sqrt{3}}{2}\hbar$, where $\hbar = h/2\pi$. If (6b) is valid, then it is arguably as profound as $S=\frac{\sqrt{3}}{2}\hbar$ due to (6b) being: (i) dimensionless; (ii) non-reliant on an empirical constant such as h; (iii) suggestive of space or related quantisation involving λ_c; and (iv) suggestive of some Compton-related process as addressed by Subsection 9.3. The classical perspective of the electron within Figure 7 does not diminish deliberations since classical and semi-classical perspectives have, in complementary manners, provided insight and understanding throughout the history of quantum mechanics.

The form of (6a) versus $S=\frac{\sqrt{3}}{2}\hbar=\sqrt{s(s+1)}\hbar$, where s = ½ is the standard spin quantum number, naturally encourages the thought of whether (6a) is expressible in a form such as $\sqrt{\lambda_c/d_t}=\sqrt{s(s+1)}n_c$, with other analogous comparisons then arising for readers familiar with standard space quantisation and its vectorial projections upon a z-axis, and so on. However, while the familiar s-form arising from mathematical comparison is engaging, an alternative tack that eventually indicates $\hbar$ quantisation (which in various forms is fundamental to quantum physics) is pursued for deeper understanding and verification. This alternative tack commences with (6a) written in terms of r_t (with the rewritten form again adhering to within 0.076% alignment):

$$\sqrt{\frac{\lambda_c}{r_t}}=\sqrt{\frac{3}{2}}n_c\,. \qquad \text{(6c)}$$

Firstly, the elegant and precise relationship between r_t and λ_c, as suggested by (6c), could indicate profoundness given that r_e (related to r_t via (5)) and λ_c are known to be connected via a well-known constant of proportionality, the dimensionless fine structure constant of ≈1/137 (formed from the four most fundamental physical constants, e, c h and ε_o, where e is electron charge magnitude and ε_o is the permittivity of free space). Viz., (6c) may provide insight into the fine structure constant which is thought by some to be key to physics unification (i.e., universal understanding) due to its relevance to several major branches of physics, including electromagnetism.

Secondly, while the appointment of n_c to quantum number status remains tentative, (6c) appears validated by recognition that it uniquely makes (with soon-discussed implications) an angular momentum quantisation statement (of embedded $\hbar$ quantisation). Such a statement is recognised by the following algebra commencing with (6c):

$$\sqrt{\frac{\lambda_c}{r_t}} = \sqrt{\frac{3}{2}} n_c$$

$$\Rightarrow \frac{\lambda_c}{r_t} = \frac{3n_c^2}{2} \qquad \text{(square both sides)}$$

$$\Rightarrow \frac{h}{r_t \cdot p_c} = \frac{3n_c^2}{2} \qquad \text{(linear momentum, } |\vec{p}| = p = h/\lambda\text{)}$$

$$\Rightarrow \frac{h}{H_{n_c}} = \frac{3n_c^2}{2} \qquad \text{(angular momentum, } \vec{H} = \vec{r} \times \vec{p}\text{)}$$

$$\therefore H_{n_c} = \frac{2}{3n_c^2} h \quad \text{(6d)} \qquad \text{or} \qquad H_{n_c} = \frac{4\pi}{3n_c^2} \hbar . \quad \text{(6e)}$$

Finally for this tack, several points of intuitive interest are generated from (6d)/(6e):

- In the above working $\lambda_c = \frac{3}{2} r_t n_c^2$, which may support (6c) meaningfulness since any half-integer multiples for quantities involving a wavelength intuitively suggest reasonability.
- The presence of a 2/3 coefficient in (6d), or any possible new fundamental quantisation relationship, is interesting and potentially meaningful since the most elemental of all quantisations (electrical charge) occurs in 1/3 and 2/3 amounts (i.e., quark charge is $\pm\frac{1}{3}e$ or $\pm\frac{2}{3}e$). As these points of interest progress, $\pm\frac{1}{3}e$ quantisation will also be implicated.
- The 2/3 coefficient in (6d) is also interesting from a classical perspective combined with the Brain Henge visualisation of r_t undergoing rotation by $\Delta\phi$. To offer explanation, the angular momentum, H, of a rotating object is directly proportional to the object's moment of inertia, I (which is essentially "rotational mass", that takes into account not just mass but also the all-important radius of rotation for the mass). Classically, I, and thus H, for a rotating thin-walled hollow sphere include a factor of 2/3 (compared to a factor of 1 for a point mass rotating about an axis). Additionally then, the fact that Lorentz proposed a deformable electron model of a spherical surface charge, that contracted and expanded with changing electron velocity, might offer broad contextual interest to some.

- With the above spherical shell visualisations in mind, it is interesting that (6e) involves $\frac{1}{3}4\pi n_c^{-2}$, and so adheres to the form $\frac{1}{3}\times$ *surface area of a sphere (A = 4πr²)*, if n_c has some inverse proportionality with a radial quantity (supported by Subsection 9.3)[7]. Hence, this perspective's outcome alternatively appears associated with $\pm\frac{1}{3}e$ quantisation and further implicates (along with images of space quantisation) a spherical geometry for Brain Henge when visualised in three dimensions.
- The $\pm\frac{1}{3}e$ and $\pm\frac{2}{3}e$ property of quarks demonstrates that e is not the smallest quantum of electrical charge in nature (e is however the smallest quantum of *free* electrical charge). Similarly, (6d) may indicate finer levels of (fractional) h quantisation than previously realised (vector projections of h aside). Since the tentative $n_c = 5$ assignment will soon be justifiably expanded to a full set of $n_c = 5, 4, 3, 2, 1$ within Subsection 9.3, taking liberty it may be stated from (6d) that the quantisation of H_{n_c} occurs in fractional amounts of h, ranging from $H_{n_c} = \frac{2}{75}h$ ($n_c = 5$) to $H_{n_c} = \frac{2}{3}h$ ($n_c = 1$).
- The $s(s+1)n_c^2$ product, identified earlier through mathematical comparison with $S = \frac{\sqrt{3}}{2}\hbar$, *may* then indicate $n_c\sqrt{H_{n_c}/2}$ as a vectorial projection of $\sqrt{h}$ if the comparison reflects more than just similar mathematical form[8].

The collective Section 9 findings thus far of: (i) outcomes such as $\Delta\phi_{\min} = \Delta\phi_{n_e=6} = \pi/6^2$ arising from (4); and (ii) underlying angular momentum quantisation in $\hbar$ multiples as per (6e), represent mission accomplished. Viz., the findings, together with the physical depiction of Figure 7, represent for Brain Henge the establishment of legitimate bases for its $Z \leftrightarrow \Delta\phi$ synergetic approach, $\Delta\phi$ resolution, and $\Delta\phi$ connectivities that underlie presented interference pathways. These findings and subsequently established bases in turn confirm the biophysical/physiological significance of Brain Henge. Nonetheless, the intriguing and seemingly profound forms of (6a) to (6e) make compelling the exploration of their n_c quantisation nature, and this exploration is undertaken by Subsection 9.3.

---

[7] In which case and if $\hbar$ is considered a deconstructable angular momentum quantity, then, while not advocating a physical reality, (6e) can also be proportionally expressed as an abstract spherical volume-linear momentum product.

[8] For readers visualising an older half-valued r_e as per footnote 6, $n_c\sqrt{H_{n_c}}$ becomes a vectorial projection of $\sqrt{h}$, (6d) becomes $H_{n_c} = h/3n_c^2$ with points of interest surrounding its 1/3 coefficient as per main text discussion, and (6c) becomes $\sqrt{\lambda_c/r_t} = \sqrt{3}n_c$.

9.3 Compton Considerations (the Nature of n_c)

While the attainment of further n_c quantisation insight is not essential to the report's primary aim, any additional insight ultimately benefits Brain Henge understanding and is therefore worthy of consideration (albeit of increased hypothetical standing and with at times assumed background knowledge, as per the previous Subsection).

The previous Subsection reveals quantisation involving r_t, λ_c and $\hbar$. This collective revelation is perhaps broadly unsurprising since prior-established $\Delta\phi$ quantisation [1], the basis of Brain Henge, is expected to be biophysically reflected in various ways, including in wavelength-associated ways as per the following scenario examples:

- Phase modulations within a waveform result in effective frequency (and therefore wavelength) modulation. The fact that (high-order, structured) $\Delta\phi$ are embedded within real physical brain waves, or EEG waveforms, means that associated effective wavelength modulations must also be embedded and, like for $\Delta\phi$, such modulations would also be quantised.
- A wide spectrum of cellular processes are regulated via frequency encodings (including frequency modulation) within cytosolic Ca ion concentration oscillations that originate from an intricate concert action between several Ca transporters [11]. Given that $\Delta\phi$ quantisation exists on a higher neuro-quantum level, then on some real physical level this quantisation might also be reflected within the known wavelength modulations of biological/cellular signal encodings.

The wavelength-based deliberations above, together with the presence of r_e and λ_c throughout the development to (6e), encourages the assumption that Brain Henge physically involves a Compton-like process to be explored in pursuit of further n_c insight. Certainly, the geometry of Brain Henge and the geometry of Compton scattering at a minimum contain analogous similarities which further encourage such an exploration, which quantitatively commences below:

Figure 7 focuses on $\Delta\phi_{\min} = \pi/6^2$ for any initial angular displacement. Considering now, via Figure 8, all six $\Delta\phi_{n_e} = \pi/n_e^2$ ($n_e = 6\ldots1$), the corresponding chord lengths, $d_{AB} = 2r_{AB}$ between circumferential points A and B, are given by:

$$d_{AB} = 2r_t \sin\left(\frac{\pi}{2n_e^2}\right). \qquad (7)$$

Combining (6c) and (7) then gives:

$$d_{AB} = 2\lambda_c \sin\left(\frac{\pi}{2n_e^2}\right)\cdot\frac{2}{3n_c^2}. \tag{8}$$

Some similarity exists between (8) and Compton's equation which is given by:

$$\Delta\lambda = 2\lambda_c \sin^2\left(\frac{\theta}{2}\right), \tag{9}$$

where $\Delta\lambda$ is the slight change (increase) in photon wavelength, up to a maximum of $2\lambda_c$, upon its scatter from an electron and θ is the angle between the directions of the incident and scattered photon.

The similarity between (8) and (9) appears to further support the notion of a Compton-like process at the heart of Brain Henge, especially when the same order of sine is achieved by visualising $\Delta\lambda$ as proportional (parallel) to a component of the vectorial change $\overrightarrow{\Delta r_t}$ (see Figure 8), whereby $\Delta\lambda = \frac{3}{2}n_c^2 d_{AB}\sin\left(\pi/2n_e^2\right) = 3n_c^2 r_t \sin^2\left(\pi/2n_e^2\right)$. However, because n_c labels $\sqrt{\lambda_c/r_t}$, this doubly quantised (by n_e,n_c subscripts) expression is preferably written:

$$\left(\frac{\Delta\lambda}{r_t}\right)_{n_e,n_c} = 3n_c^2 \sin^2\left(\frac{\pi}{2n_e^2}\right). \tag{10}$$

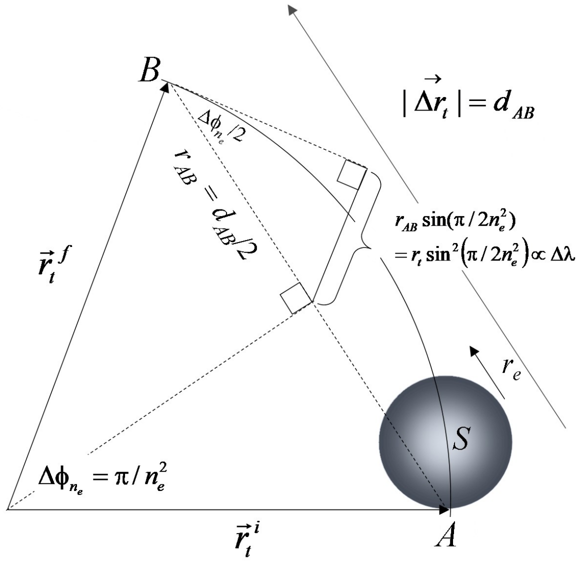

Figure 8: Hypothetical geometry for a Brain Henge sector of any quantised angle $\Delta\phi_{n_e}$, which also reflects an associated $\Delta\lambda$ for a Compton-like perspective as per (8) to (10). $\overrightarrow{\Delta r_t}$ is the vectorial difference between initial and final radial vectors $\vec{r}_t^{\,i}$ and $\vec{r}_t^{\,f}$, with $\Delta\lambda$ taken as proportional to a component of r_{AB} and therefore $\overrightarrow{\Delta r_t}$.

Within the Compton effect $\Delta\lambda$ reflects lost kinetic energy of the scattered photon, and so (10) also suggests quantised kinetic energy loss (and synergetic gain elsewhere for its total conservation within an elastic process).

Because: (i) n_c labels different angular momentum states in (6d)/(6e), with $n_c = 5$ previously assigned to the geometry of Figure 7; (ii) Figure 7 appears to represent a minimum value for r_t; and (iii) some inverse proportionality between r_t and n_c is suggested by the overall proportionality of $\sqrt{\lambda_c / r_t} \propto n_c$ in (6c) and by the previously made comparison between (6e) and $A = 4\pi r^2$ in Subsection 9.2, it is assumed here that $n_c \leq 5$, i.e., $n_c = 5, 4, 3, 2, 1$ with the progressive decrease in n_c associated with a progressive increase in r_t (and with the possible singularity case of $n_c = 0$ discussed later).

The proportionalities involving n_c as revealed by (6d)/(6e) and (10), i.e., $H_{n_c} \propto 1/n_c^2$ and $\sqrt{\Delta\lambda / r_t} \propto n_c$, additionally appear to be physically reasonable. For example, $n_c = 5$ reflects a relatively small physically-sized system (in a radial motion context) and relatively high $\Delta\lambda$ (i.e., a photon giving up relatively more kinetic energy in an elastic scatter process, analogous to a billiard ball colliding with another billiard ball or object of comparable size). Conversely, $n_c = 1$ reflects a relatively large system, with a photon giving up less kinetic energy during elastic scatter with some "massive" system. The latter situation is analogous to a billiard ball colliding with a (linearly stationary) billiard ball of greater mass, while the possible special singularity case of $n_c = 0$ might analogously suggest collision with an immovable/immense object such that $\Delta\lambda = 0$.

In summary, Figure 9 gives $(\Delta\lambda / r_t)_{n_e, n_c}$ state profiles that are based on (10) for $n_c = 5$ to 1 and $n_e = 6$ to 1.

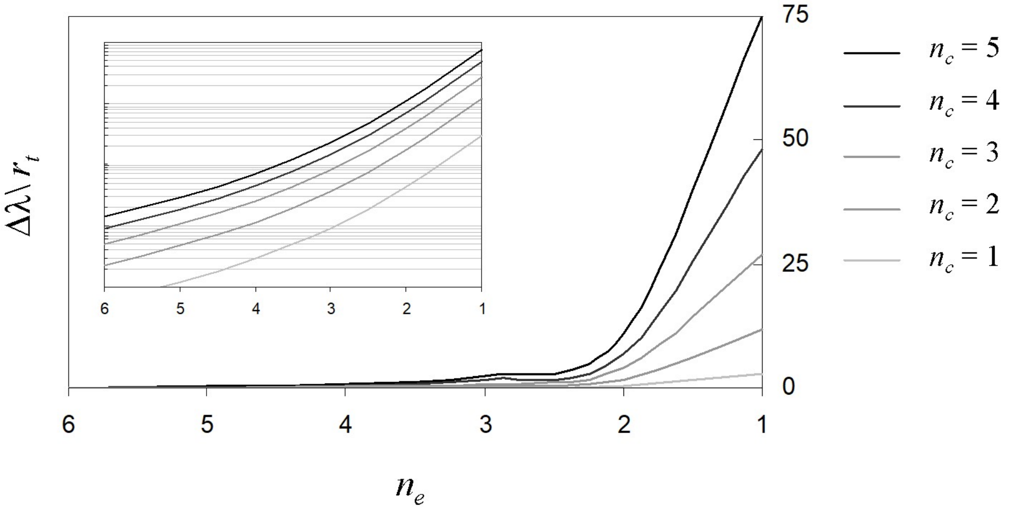

Figure 9: $\Delta\lambda/r_t$ as predicted by (10) for $n_e = 6$ to 1 and $n_c = 5$ to 1 for the hypothesised Compton-like process of Brain Henge. The inset demonstrates the same graph with a logarithmic *y*-axis scale.

Finally, in addition to reasons of mathematics-in-nature appreciation, the numerical exactness of several $(\Delta\lambda / r_t)_{n_e,n_c}$ values within the profiles of Figure 9 is noteworthy for the overall depiction of system quantisation (allowing for example the reflection of quantisation within ratios of $(\Delta\lambda / r_t)_{n_e,n_c}$ to be considered). From (10), all $(\Delta\lambda / r_t)_{n_e,n_c}$ values for $n_e = 1$ ($\Delta\phi_1 = 180^o$) are integers as expected ($3n_c^2$ for all n_c). Numerical exactness is also expected (at least approximately) where a small angle approximation applies in (10) ($n_e = 6$ and 5, and to a lesser extent $n_e = 4$), but not necessarily for the remaining $n_e = 3$ and 2. Following are some *prime* n_e-specific examples of such "numerical exactness" for all n_c, in which: $k = \sqrt{\pi}/5$; the bracketed value is the percentage error as compared to (10); and the last of the expressions (for $n_e = 6$, 5 and 4) is based on the small angle approximation.

$$\left(\sqrt{\Delta\lambda / r_t}\right)_{n_e=1,n_c} = \sqrt{3}n_c \qquad n_e = 1 \quad \text{(exact)}$$

$$\left(\sqrt{\Delta\lambda / r_t}\right)_{n_e=2,n_c} = \frac{\sqrt{7}kn_c}{\sqrt{2}} \qquad n_e = 2 \quad (+0.055\%)$$

$$\left(\sqrt{\Delta\lambda / r_t}\right)_{n_e=3,n_c} = \frac{3\sqrt{2}kn_c}{5} \qquad n_e = 3 \quad (+0.009\%)$$

$$\left(\sqrt{\Delta\lambda / r_t}\right)_{n_e=4,n_c} = \frac{\sqrt{11}kn_c}{4\sqrt{3}} \qquad n_e = 4 \quad (-0.042\%)$$

$$\left(\sqrt{\Delta\lambda / r_t}\right)_{n_e=6,5,4,n_c} = \frac{\sqrt{3}n_c\pi}{2n_e^2} \qquad n_e = 6\ (+0.032\%),\ 5\ (+0.066\%),\ 4\ (+0.16\%).$$

From the above expressions, the ratio of $(\Delta\lambda / r_t)_{n_e,n_c}$ for two states, *i* and *j*, might be considered when reflecting upon the outcomes of Brain Henge quantisation. For example, the small angle approximation-based expression (for n_e = 6, 5 and 4) gives:

$$\sqrt{\frac{(\Delta\lambda / r_t)_i}{(\Delta\lambda / r_t)_j}} = \left(\frac{n_c}{n_e^2}\right)_i \cdot \left(\frac{n_e^2}{n_c}\right)_j , \tag{11}$$

for which ratio errors range from +0.063% (*i* and *j* both involving n_e = 6) to +0.32% (*i* and *j* both involving n_e = 4), with reduction to $\sqrt{\Delta\lambda_i / \Delta\lambda_j} = (n_e^j / n_e^i)^2$ for *i* and *j* involving the same n_c also indicated.

While evidence supporting the nature of n_c quantisation has been presented, the nature cannot be absolutely stated without exact knowledge of governing system potential and related factors. Furthermore, formalism development to this point has likely evoked for interested readers several intuitive pathways to consider[9], all of which are left for future deliberations due to the report's primary aims being accomplished.

In conclusion to Section 9, if its hypothetical deliberations and quantisation outcomes such as $\Delta\phi_{n_e} = \pi / n_e^2$, $\sqrt{1/D_t} = \frac{\sqrt{3}}{2} n_c$ and $(\Delta\lambda / r_t)_{n_e,n_c}$ represent a physical reality, then the deliberate structuring of $\Delta\phi$ (and fine structuring via α) within neurological signalling, as identified by [1], is most certainly verified. Such verification would in turn further support the hypothesised notion of electromagnetic interaction with the modern ether being a component of heavy metal neuro-quantum signal interference pathways as presented.

---

[9] For example questioning the existence of some $n_c^{\max} = n_e^{\max} - 1$ relationship for numerically maximum n_c and n_e values, questioning the existence of some n_c degeneracy/substructure, including in relation to fine α structuring, and so on.

10. Brief Speculations of Intrigue

The brief deliberations of this Section are hypothetical and intended as intriguing bases for future thought discussions.

10.1 Parallel $\Delta\phi$ Alignment Involving H_2O

An intriguing speculative observation that follows from the Pb phase wheel of Figure 6e involves the additional parallel alignment between Pb and H_2O (i.e., $\Delta\phi_{Pb} = 410^o \equiv 50^o$ and $\Delta\phi_{H_2O} = 50^o$, with the latter based on an assumed simple addition of the Z values of H, H and O followed by familiar linear mapping of the resulting $Z_{total} = 10$). Consideration of the $\Delta\phi_{Pb} \equiv \Delta\phi_{H_2O} = 50^o$ alignment is particularly intriguing due to the hypothetical adverse health scenario whereby on some neuro-quantum level, $\Delta\phi_{Pb}$ versus $\Delta\phi_{H2O}$ acuity is compromised due to the corruption of usually distinguishing α_{Pb} and α_{H2O} values.

10.2 Physiological Role of Noble Gases

It is conventionally accepted that noble gases are biologically non-reactive, with their partitioning and exchange controlled only by physical processes, and so for example biological airway concentrations of noble gases are essentially the same as that of the atmosphere. However, prime number observations plus several symmetrical connectivities and alignments within presented phase wheels, involving noble gas-associated Primary $\Delta\phi$ Families (e.g., statistically significant $Z_1 + Z_2$ outcomes of Table 1 plus $\Delta\phi_{He} = 10^o$, $\Delta\phi_{Ne} = 50^o$, $\Delta\phi_{Ar} = 90^o$, $\Delta\phi_{Kr} = 180^o$ and $\Delta\phi_{Xe} = 270^o$ partaking in the symmetries of Figures 4c, 6c, 6e and/or 6f), encourages deliberation upon current convention.

It has been shown that characteristic of RBCs is a notable noble gas supersaturation, indicating absorption onto the RBC, with gas excess increasing in proportion to noble gas atomic mass [12]. If noble gases have some neuro-quantum signalling role, then interference-related lost acuity within the role might indirectly and adversely affect the physiology of this supersaturation, and even indirectly associate with pathologies such as diminished RBC deformability that is sometimes seen in CFS [13,14].

Speaking further to a possible noble gas neuro-quantum signalling role, and therefore to potential for interference to this role, it is noteworthy to recall from [1] that Primary $\Delta\phi$ Families form several high-precision common fractions based on the ratios of their α

values (e.g., for the Primary Families associated with He and Ne, α_{He}:α_{Ne} = 4:5), with these ratios also typically being biologically and/or psychosocially significant. For He and Ne especially, one might philosophically deliberate why the second and fifth most abundant elements of the universe play no direct physiological role. The contrary argument of course being because of their inertness, but He and Ne playing a quantum programming role, rather that a convention physiological role, is perhaps more easily accepted.

10.3 Connectivity Between Functional $\Delta\phi$ and Physical Geometrical Form

It is intriguing that $\Delta\phi = 30^{o}$ for the Primary Family associated with C, given the well-known hexagonal crystal structures associated with C and the 60^{o} symmetry within such structures. While it offers no foreseeable advantage, one could introduce a factor of 2 within formalism, without impacting findings, to bring about $\Delta\phi_{C}' = 2\Delta\phi_{C} = 60^{o}$.

However, the presentation of some case, if it unexpectedly exists, for neuro-quantum phase angles aligning with physical angles within crystal/molecular structures is not pursued, other than to make a final observation of intrigue in regards to the *sum* of $\Delta\phi$ for select structures. Viz., a hexagonal structure such as graphite might be assigned a summed value of $\Sigma\Delta\phi_{C} = 6 \times 30^{o} = 180^{o}$; a cubic structure such as NaCl might similarly be assigned $\Sigma\Delta\phi_{Na\rightarrow Cl} = 4 \times 45^{o} = 180^{o}$ based on (3a) for the $n = 2$ case; and a cubic structure such as Li might be similarly assigned $\Sigma\Delta\phi_{Li} = 4 \times 15^{o} = 45^{o}$. And so the intriguing possibility of $\Sigma\Delta\phi$ or $\Sigma\Delta\phi$ equating to landmark polar angles (especially those of the $n_e = 1$ and 2 cases within (4)) arises for some stable structures, albeit for a select few examples.

10.4 Further Implications of the Quantum Basis of Brain Henge

While Subsection 9 quantisation findings such as $\sqrt{\lambda_c / r_t} = \sqrt{3/2}n_c$ may initially present as surprising, suggestions of quantisations beyond the conventional (those usually associated with energies and angular momenta) are broadly not uncommon. As examples:

- Energy and its units can be broken down into more fundamental quantities and units (consider various rudimentary equations for energy, like that of kinetic energy), leading to suggestions from several quarters that fundamental quantities such as distance and time must also be quantised.
- Planck's units reveal a minimum measurable distance, as well as a minimum time duration of physical meaning.

- Orbital radius is quantised in Bohr's model of the hydrogen atom.
- The Heisenberg uncertainty principle, which specifies an uncertainty in stating the position of a particle due to the limits of measurement and more broadly due to fundamental limits imposed by nature (e.g., the Compton effect that a measuring photon will have on the particle), gives for the complementary pair of ΔE and Δt (uncertainty in the energy of a particle and the time interval it remains in a given energy state), the relationship $\Delta E \cdot \Delta t \geq \hbar / 2$. The equality case of $\Delta t = \hbar / 2\Delta E$ especially suggests that time, like energy, might be quantised.
- Compton scattering off an electron might expectedly be quantised because the electron is an inherently quantum phenomenon.

Hence, Section 9 quantisation findings are philosophically reasonable and, in the fullness of time, may reveal even further intriguing-to-consider quantisations such as time quantisation for like acceleration (r_t and $\Delta\lambda$ being centrifugally parallel as per Figure 8).

11. Concluding Remarks

Fascinating new examples of mathematics-in-nature (especially mathematics-of-the-brain) are identified and include several quantised relationships of potentially profound physical significance, such as $\Delta\phi_{n_e} = \pi / n_e^2$ and $\sqrt{1/D_t} = \frac{\sqrt{3}}{2} n_c$. Through these examples the report aspires to positively contribute to: (i) universal understanding in general; (ii) diagnostic, therapeutic and biomedical engineering facets of the neurological sciences for which the deciphering of currently untapped information within the EEG (or within the high-order functional electrical signalling of the brain more broadly) is likely to bring scientific advancement; and (iii) neurological health by way of the identification of specific neuro-quantum interference pathways for heavy metals, as per Section 7.

The report subsequently offers insight into a possible CFS mechanism and treatment approach. In regards to CFS treatment, it is acknowledged within Section 1, and the Case Study of [2], that a formalised study with multiple independent subjects is required to exclude existing possibilities such as coincidental outcome and treatment response that applies to an individual but not the majority. This formalised need is now also required to validate the report's theorised heavy metal interference pathways. However, the presented evidence is sufficiently encouraging to inspire guarded optimism, especially since validation would carry significant potential health implications.

Finally, the above (quantum) treatment's: (i) inherent electromagnetic underpinning (i.e., modern ether-related theory); (ii) finding of the most electromagnetically relevant elements appearing most affected in the Case Study of [2]; and (iii) associated magneto-functional connectivities such as those depicted by Figure 4b, are arguably not inconsistent with known neurological sensitivities to therapies such as transcranial magnetic stimulation (suggested in [2] as an example less passive future complement to quantum treatment). Hence, the prospect of report concept transference from CFS to especially neurological illnesses already efficaciously linked to electromagnetically-based therapies appears reasonable and also provides optimism for the future.

References

1. Simeoni RJ. 2021 A new approach to high-order electroencephalogram phase analysis details the mathematical mechanisms of central nervous system impulse encoding. *UNET J. Sci. Soc.* **1,** 1-34. (https://doi.org/10.52042/UNETJOSS010101)

2. Simeoni RJ. 2022 Chronic fatigue syndrome: a quantum mechanical perspective. *UNET J. Sci. Soc.* **2,** 21-42. (https://doi.org/10.52042/UNETJOSS020103)

3. Simeoni RJ. 2003 Bohr's model of atomic hydrogen extended to include electron rotational kinetic energy. *Physics in Canada.* **59**, 309-311.

4. Simeoni RJ. 2008 Noble gas magic numbers: from quarks to quasars, *Austral. Math. Soc. Gaz.* **35,** 93-96.

5. Anke M, Croppel B, Kronemann H, Grün M. 1984 Nickel – an essential element. *IARC Sci. Publ.* **53,** 339-365.

6. Alkim H, Koksal AR, Boga S, Sen I, Alkim C. 2017 Role of bismuth in the eradication of Helicobacter pylori. *Am. J. Ther.* **24:** e751-e757. (https://doi.org/10.1097/MJT.0000000000000389.)

7. Bhoelan BS, Stevering CH, van der Boog AT, van der Heyden MA. 2014 Barium toxicity and the role of the potassium inward rectifier current. *Clin. Toxicol.(Phila).* **52,** 584-593. (https://doi.org/10.3109/15563650.2014.923903)

8. Resongles E, Dietze V, Green DC, Harrison RM, Ochoa-Gonzalez R, Tremper AH, Weiss DJ. 2021 Strong evidence for the continued contribution of lead deposited during the 20th century to the atmospheric environment in London of today. *PNAS* **118**. (https://doi.org/10.1073/pnas.2102791118)

9. Dumková J, Smutná T, Vrlíková L, Le Coustumer P, Večeřa Z, Dočekal B, Mikuška P, Čapka L, Fictum P, Hampl A, Buchtová M. 2017 Sub-chronic inhalation of lead oxide nanoparticles revealed their broad distribution and tissue-specific subcellular localization in target organs. *Part. Fibre Toxicol.* **14:55**. (https://doi.org/10.1186/s12989-017-0236-y)

10. Morris G, Maes M. 2014 Mitochondrial dysfunctions in myalgic encephalomyelitis/chronic fatigue syndrome explained by activated immuno-inflamatory, oxidative and nitrosative stress pathways. *Metab. Brain Dis.* **29,** 19-36. (https://doi.org/10.1007/s11011-013-9435-x)

11. Smedler E, Uhlén P. 2014 Frequency decoding of calcium oscillations. *Biochem. Biophys. Acta.* **1840,** 964-969, 2014. (https://doi.org/10.1016/j.bbagen.2013.11.015)

12. Tomonaga Y, Brennwald MS, Livingstone DM, Tomonaga G, Kipfer R. 2014 Determination of natural in vivo noble-gas concentrations in human blood. *PLoS ONE* **9:** e96972. (https://doi.org/10.1371/journal.pone.0096972)

13. Saha AK, Schmidt BR, Wilhelmy J, Nguyen V, Abugherir A, Do JK, Nemat-Gorgani M, Davis RW, Ramasubramanian AK. 2019 Red blood cell deformability is diminished in patients with chronic fatigue syndrome. *Clin. Hemorheol. Microcirc.* **71,** 113-116. (https://doi.org/10.3233/CH-180469)

14. Miwa K. 2015 Cardiac dysfunction and orthostatic intolerance in patients with myalgic encephalomyelitis and a small left ventricle. *Heart Vessels* **30,** 484-489. (https://doi.org/10.1007/s00380-014-0510-y)

Appendix A

A New Approach to High-Order Electroencephalogram Phase Analysis Details the Mathematical Mechanisms of Central Nervous System Impulse Encoding (1 March 2021)

Appendix Disclaimer: The inclusion of this officially peer reviewed paper within the present report, permitted under the Author copyright maintenance policy of the paper's host journal, does not necessarily indicate report endorsement by the host journal, especially given the report's hypothetical aspects and abstract thought discussions.

UNETJOSS
Journal of Science and Society
in association with ChristianUniversityforAustralia.org.au

Date of submission Sept. 28, 2020, date of acceptance Feb. 5, 2021.
https://doi.org/10.52042/UNETJOSS010101

A New Approach to High-Order Electroencephalogram Phase Analysis Details the Mathematical Mechanisms of Central Nervous System Impulse Encoding

Ricardo J. Simeoni
Research and Development, Neurödinger, Sunshine Coast, QLD 4575 Australia.

Corresponding author: Ricardo J. Simeoni (rsimeoni@neurodinger.com, www.neurodinger.com).

This work is fully funded by Neurödinger which holds an associated patent pending with priority date Sept. 9, 2020.

ABSTRACT This paper presents a new electroencephalogram (EEG) analysis technique which is applied to example EEGs pertaining to nine human subjects and a broad spectrum of clinical scenarios. While focusing on technique physical efficacy, the paper also paves the way for future clinically-focused studies with revelations of several quantified and detailed findings in relation to high-order central nervous system communicative impulse encoding akin to a sophisticated form of phase-shift keying. The fact that fine encoding details are extracted with confidence from a seemingly modest EEG set supports the paper's position that vast amounts of accessible information currently goes unrecognised by conventional EEG analysis. The technique commences with high resolution Fourier analysis being twice applied to an EEG, providing newly-identified harmonics. Except for deep sleep where harmonic phase, ϕ, behaviour becomes highly linear, ϕ transitional values, $\Delta\phi$, measured between harmonics of progressively increasing order are found to cluster rather than follow a normal distribution (e.g., $\chi^2 = 303$, $df = 12$, $p < 0.001$). Clustering is categorised into ten Families for which many separations between $\Delta\phi$ values are writable in terms of $k = j/4$ or $j/3$ ($j = 1, 2, 3 \ldots$), with a preference for $k = j/2$ ($\chi^2 = 77$, $df = 1$, $p < 0.001$), amounts of a Family-specific quantum increment value, $\alpha_{\Delta\phi}$. A parabolic relationship ($r > 0.9999$, $p < 0.001$) exists between $\alpha_{\Delta\phi}$ (and the parabola minimum associates with an additional inter-Family or universal quantum increment value, $\alpha_{\min}$). Ratios of $\alpha_{\Delta\phi}$ typically align within ± 0.5% of simple common fractions (95% CI).

INDEX TERMS Communication, electroencephalogram, encoding, high-order phase analysis, phase-shift keying

1. INTRODUCTION

1.1 GENERAL INTRODUCTION AND AIMS OF STUDY

The complexity of the human brain with its approximately 100 billion neurons undoubtedly transcends to some high-order form of collective electrical signal (impulse) encoding within everyday central nervous system (CNS) function associated with motor control and the cognitive processes including those of memory storage, recall and utilisation. The sophisticated detail of this encoding (i.e., the mathematical nature and co-ordination of embedded modulation and sequencing keys) is far from fully understood despite decades of scientific study into the human electroencephalogram (EEG). In fact, given the large volume of information gathered in a single EEG sitting, through multi-channel high sampling rate data acquisition of several minutes to hours duration, modern EEG analysis surprisingly still mostly adopts conventional, in some cases rudimentary, brain activity indicators that are based upon long-standing approaches, or extensions to these core approaches, rather than upon genuinely new analysis alternatives, and this is particularly true at the clinical interface (these existing indicators are introduced within Subsection 1.2).

One may readily undertake any number of contrasting (in terms of information volume provision) colloquial comparisons to appreciate that, while conventional EEG analysis is often clinically diagnostic, vast volumes of untapped CNS impulse encoding information must be embedded within the complexities of the EEG, and so remain lost to neurodiagnosis. Two such colloquial comparison examples include 1 μg of DNA being theoretically capable of storing up to approximately 500 Tbytes of information [1], and the efficient communication rates (≥ Mbit per second) of Bluetooth-type technologies [2]. The encoding complexities of the CNS must logically be somewhat comparable (if not superior) to these systems, yet current EEG information revelation pales by comparison. Nonetheless, the cerebral cortex functional activation information (of high temporal resolution) provided by conventional EEG analysis, sometimes in conjunction with magnetoencephalogram (MEG) analysis which originates from the same neurophysiological processes, is clinically invaluable, as is the electrophysiological information provided by sophisticated and established EEG simulation models [3–5] that, through techniques such as inverse solution dipole localisation, provide important EEG insights into organisational complexities of spatiotemporal dynamics across cortical depths, synchronicity, coherence, and surface Laplacians. Note that due to the EEG-MEG overlap, several aspects of the present study will likely also apply to MEG analysis (with recognition of its comparative advantages and disadvantages including challenges associated with accessibility and low-level magnetic field detection), however study focus will remain on EEG analysis.

Functional magnetic resonance imaging (fMRI) and positron emission tomography (PET) increasingly offer competing alternatives or complementary options to EEG analysis, as they collectively detect parameters such as: (i) cerebral blood flow and fluctuations in capillary deoxyhaemoglobin populations which are triggered by the activity of neural populations; (ii) the rate of glucose metabolism which is proportional to the rate of synaptic firing; and (iii) enhanced dopamine secretion which is linked to the activation of genes responsible for brain function [6–11]. For example, through the detection of otherwise finely hidden levels of brain activity, fMRI and (especially) PET offer improved differential diagnosis and long-term recovery likelihood prognostication within consciousness disorders such as unresponsive wakefulness syndrome [8]. Another synergism example challenges a previously held notion of EEG-fMRI interchangeability when analysing neural modulation mechanisms that support visual attention [10]; the demonstration of categorically different stimulus-evoked EEG and fMRI signal patterns in that study leads to a conclusion of necessary haemodynamic and electrophysical system complementarity for the understanding of neural processes supporting cognition. However, despite these described modality synergies, the inherent physical natures of fMRI and PET with their classifications as secondary brain function measures (due to their collective reliance on blood flow and physiological processes involving metabolic activity changes), makes more direct EEG analysis the most likely of the modalities to be receptive to new methods of high-order mathematical analysis with CNS impulse encoding revelation.

The current limited understanding of CNS impulse encoding does not of course negate: (i) the life-changing capacity of advancements in implantable neuroprosthetics such as the cochlear ear [12] and bionic eye (retinal implant) [13]; (ii) the similar capacity of new generation implantable brain-computer interface (BCI) devices including both predictive/advisory-types (e.g., preparing an implanted patient for an anticipated epileptic seizure) and sensory motor function-types (e.g., involving prosthetic limb control) [14–16]; and (iii) the therapeutic effectiveness of deep brain stimulation [17–19], transcranial magnetic stimulation (TMS) [20], and other such neural stimulation therapies.

Rather, the afore introductory comments reasonably recognise that even with a predicted BCI revolution on the neural engineering horizon [15], several years of further advancements are still required to achieve: (i) a full understanding of the deliberate physiology of action potential processes and coordination that lead to EEG characteristics; (ii) neuroprosthetics and BCI at levels allowing full and fine autonomous control (e.g., signal interfacing to substantially mitigate conditions such as spinal cord injury); and (iii) more informed and effective methods of formulating, administering and understanding the benefits of targeted neural stimulation therapies (e.g., for the alleviation treatment of conditions such as depression, Alzheimer’s disease, Parkinson’s disease, Tourette syndrome, tinnitus, and so on).

The present study primarily aims to contribute to such advancement by the introduction of a new, high-order EEG phase analysis technique via its application to a broad clinical spectrum of EEGs (associated with healthy adults in various awake and sleep states, an adult diagnosed with probable Alzheimer’s disease, and various electrode positions), with focus remaining on the *physical* efficacy and applicability of the technique in the variety of clinical circumstances. That is, the design and implementation of clinical research into some specific group or pathology is not part of the study’s aims. However, in reaching its primary aim the study is inevitably expected to generate a basis for such clinical research into the future, and the identification and interpretation of new, high-order characteristics of EEG phase-based encoding is anticipated. In line with [2] it is also postulated that any such phase-based encoding will possess significant quantisation facets.

1.2 CONVENTIONAL EEG ANALYSIS BRIEF OVERVIEW

Time-domain EEG waveforms routinely provide clinical information such as burst and other pattern diagnostics in response to some external auditory, sensory or visual neural stimulus (e.g., temporary reactive changes in parameters such as amplitude and signal-to-noise ratio for a steady-state visually-evoked potential, or SSVEP). Frequency-domain spectra provide a range of complementary diagnostic indices which often refer to the traditional delta, theta, alpha and beta bands, approximately corresponding to spectral frequency ranges of 0.5 to 4, 4 to 8, 8 to 13 and >13 Hz respectively (an additional gamma band that caps and surpasses the beta band from approximately 30 Hz onwards may also be included for relatively high frequency spectra). The total and proportional activities (or powers) of the traditional bands, as well as several permutations of *ratios* of band activities are representative of conventional EEG indices that are monitored within a diagnostic setting [11,21–23], with related but more advanced indices formed by combining several frequency band components (e.g., of the SSVEP).

The index of coherence, that measures the degree of phase similarity and thus functional connectivity for different brain locations, as well as long- and short-range correlates between frequency band components for different brain locations, also make valuable contributions to the understanding of brain function (e.g., by demonstrating that smaller amplitude alpha activities in prefrontal and frontal locations are not solely due to the conduction of electrical currents associated with typically larger amplitude alpha activities in occipital-parietal locations, as was once supported) [11,24,25]. Relatively simple indices that are not specific to any particular band include median frequency and spectral edge frequency (SEF), where SEF is defined as the frequency below which a specified percentage (typically 95%) of a spectrum's power exists [23,26].

It has long been recognised that despite the important clinical information and quantified correlations with physiological or pathological states that conventional EEG indices like those above can provide, their correlations are nevertheless sometimes equivocal or confounded by influencers (e.g., anaesthetic drugs), especially for more simple indices like SEF [23,26–28], such are the inherent complexities of EEG dynamics [4]. Furthermore, even the most experienced EEG reader (e.g., anaesthesiologist, neurologist, sleep technician, etc.) will acknowledge that the neurodiagnostic capability of the EEG overall remains restrictive and certainly lacks specific detailed impulse encoding information as previously introduced. Hence, the development of EEG analysis techniques of ever increasing sophistication is ongoing.

A brief overview of one such sophisticated yet well established phase-based analysis technique, namely bispectral (bicoherence) analysis, follows (since the present study aims to identify and apply a new form of high-order, phase-based EEG analysis, potentially with the inclusion of impulse encoding revelations). However, before that overview it is pertinent to acknowledge that at their core, these established and emerging techniques still incorporate the same wide umbrella of conventional spectral principles, and it may therefore be argued that EEG analysis advancements to some degree are plateauing.

Bispectral analysis, which includes the subset of bicoherence analysis, detects for the existence of phase couplings between the n sinusoidal harmonics, $X_n(f_n) = c_n\sin(2\pi f_n t + \phi_n)$, of an EEG biosignal, where for a given harmonic c_n is amplitude, f_n is frequency and ϕ_n is phase, with t being time. For common second-order analysis, bicoherence, written $bic(f_p, f_q)$, equals 100% if harmonics $X(f_p)$, $X(f_q)$ and $X(f_p+f_q)$ maintain a constant phase relationship in time (see figure 1a). Conversely, if the phases of the three harmonics vary independently in time, as represented by the different phase relationships for the time intervals either side of the vertical line in figure 1b, then $bic(f_p, f_q)$ equals 0%. Accordingly, $bic(f_p, f_q)$ values between 0 and 100% represent other proportionate degrees of second-order phase coupling. A graph of all $bic(f_p, f_q)$ values gives the bicoherence spectrum which is a normalised (via c_n effect negation) version of the bispectrum of corresponding $B(f_p, f_q)$ values. To calculate $bic(f_p, f_q)$ (and $B(f_p, f_q)$ which is implied by $bic(f_p, f_q)$ from this point) over an extended time period, the EEG biosignal is divided into several (e.g., 32) epochs, which may or may not overlap (two such contiguous epochs are depicted by figure 1b), and the harmonic phase information of all epochs is then statistically combined (see [29–32] for relevant equations and further background).

Relatively high $bic(f_p, f_q)$ values indicate that brain function involves significant nonlinear processes (the brain is considered a nonlinear biological system that displays complex dynamics and deterministic chaotic behaviour) and, by observing changes in second-order phase couplings in response to various stimuli, information on, or a deeper understanding of, these nonlinear processes may be achieved [30–35].

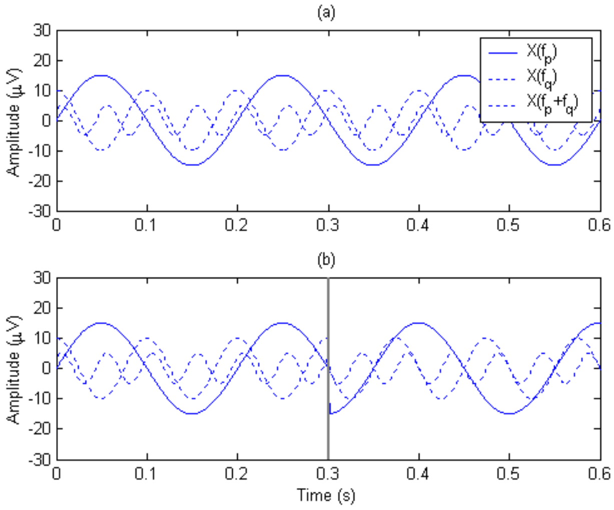

FIGURE 1. **(a) Harmonics $X(f_p)$, $X(f_q)$ and $X(f_p+f_q)$ maintain a constant phase relationship in time and (b) the phases of the three harmonics vary independently in time as indicated by a different phase relationship for the time intervals (epochs) either side of the vertical line.**

One of the most established applications of EEG-based bispectral analysis involves the determination of an index for depth of brain anaesthesia in the form of the bispectral index, which is extensively documented [23,26,30,36–39]. However, bispectral analysis has also been successfully and widely applied as a diagnostic tool within studies involving: phases of epileptic seizure [40,41]; identification of epileptic and focal cerebral ischemia [40,42]; sleep detection [43]; evaluation of the degree of brain maturation in neonates [44]; differentiation of quadriceps muscle activation [45]; and normal sinus versus ischemic, tachycardia and fibrillation cardiac rhythms [31,46].

Example bicoherence spectra for asymptomatic, healthy adults in a somewhat neutral or largely non-stimulated neural state are seemingly unremarkable with example spectra respectively shown in figures 2a and 2b for EEG [34] and electromyogram (EMG) [47]. A further EEG example for higher alpha activation is given in figure 2c, with figure 2d showing its corresponding harmonic-amplitude-reflecting bispectrum [48].

The characteristic triangular shape of bicoherence spectra is a consequence of the mathematical permutations of f_p, f_q and f_{p+q} that are possible without exceeding the maximum spectral frequency. Chaotic-like EEG- and EMG-based spectra such as those of figures 2a and 2b contain characteristic parallel ridge-like contours of high $bic(f_p, f_q)$ at approximately 45^o to the x-axis, as highlighted in those figures and which are also identifiable in figure 2c for higher neural activation. These contours are explicitly noted or identifiable within some of the earliest bicoherence studies [30,31,49] and are considered typical of a normal chaotic response [31,49] which is also observed within electrocardiogram (ECG) bicoherence spectra [31,50]. However, these contours can also be interpreted as several frequencies being coupled to the same f_{p+q} in concert with some form of complex oscillatory $bic(f_p, f_q)$ behaviour across all frequencies (this latter interpretation is particularly relevant for Subsection 1.3). Also indicated by spectra such as figure 2c are couplings across the standard EEG frequency bands (with such inter-band couplings known to be dependent on EEG state [32,48,51]), and higher-order spectral aspects (e.g., self-coupling of diagonal bicoherence contours [32]) have also been studied as addressed further within Subsections 1.3 and 3.3.5.

The chaotic-like nature of EEG bicoherence spectra as exemplified by figure 2a, when the CNS is busy maintaining homeostasis, arguably defies phase relationship expectations of a highly intelligent communication platform and provides motivation for new higher-order forms of phase analysis. Also adding to this motivation is the fact that, while bispectral analysis displays previously cited clinical sensitivities, it is subject to several numerical and physical limitations:

Limitations of bispectral analysis

- Bispectral equations are statistical in nature by their reliance on a vectorial cancellation addition process over all epochs [30,47], with perfect vectorial cancellation yielding $bic(f_p, f_q) = 0\%$ unlikely to mathematically occur due to the finite number of epochs utilised, even if the phase relationships between $X(f_p)$, $X(f_q)$ and $X(f_p+f_q)$ are in actuality completely random.

- The consideration of only second-order (or other relatively low-order) phase couplings is a mathematical simplification (arguably an over-simplification) of the complexity of brain neurophysiology. That is, the complex, nonlinear nature of the brain is expected to contain important higher-order, nonlinear processes, as recognised since the earliest bispectral studies [30,31]. Indeed, it is reasonable that *many* harmonics might instead be expected linked by dynamically changing and sophisticated phase relationships within the impulse encoding of the CNS.

- EEG harmonics oscillate up to ≈60 times per second (since the maximum frequency of conventional EEG frequency spectra is ≈60 Hz, but may even be higher). Over a given epoch, typically up to several seconds duration, bispectral analysis assumes that all ϕ_n remain constant. When harmonics are oscillating at up to ≈60 Hz, the assumption that their ϕ_n remain constant over a several, or even partial, second epoch duration is tenuous. The trend towards using increasingly (in some cases unnecessarily) higher sampling frequencies for EEG acquisition does not overcome this limitation.

- Like the more fundamental EEG indices summarised within this Subsection, while bispectral analysis provides useful clinical information, due to its physical nature the revelations it provides in relation to CNS impulse encoding is and can only be limited.

1.3 HIGHER-ORDER PHASE ANALYSIS OF THE PRESENT STUDY

As noted above, the existence of high-order EEG aspects have been acknowledged within scientific literature for decades, with high-order analysis techniques applied to phase couplings, synchronous relationships across frequencies, and autoregressive EEG modelling formalisms [29,32,42,48,51–54]. As a specific example, in a majority of EEG burst patterns that display high values along the bicoherence diagonal, up to tenth-order (and most commonly fifth-order) self-frequency and self-phase couplings have been identified and analysed [32].

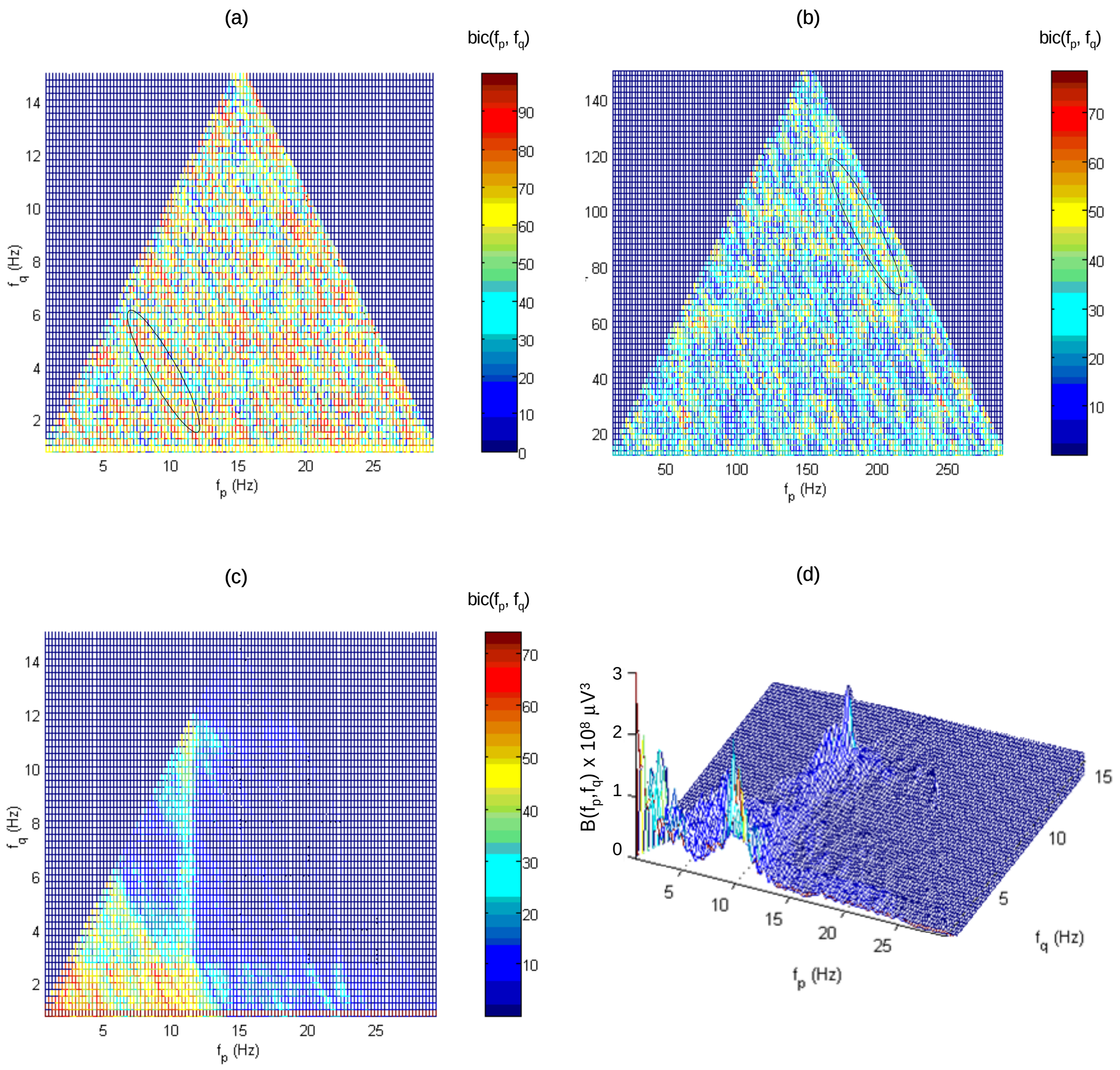

FIGURE 2. **Typical non-stimulated, asymptomatic chaotic-like bicoherence spectrum for (a) EEG [34] and (b) EMG [47] which display bic(f_p, f_q) calculated for all f_p and f_q, with typical ridge-like contours highlighted. An example EEG bicoherence spectrum for higher alpha activation is given in (c), with (d) showing its corresponding bispectrum [48]. bic(f_p, f_q) = 100% indicates a constant phase relationship between the harmonics X(f_p), X(f_q) and X(f_{p+q}), whereas bic(f_p, f_q) = 0% indicates that the phases of the harmonics vary independently.**

The somewhat periodic bicoherence contours across frequencies noted in Subsection 1.2 are also indicative of some higher-order phase interrelationship, with this interrelationship including an *oscillatory* component. Given this component and the range of other oscillatory behaviours that are inherent within the complexities of the EEG[1], the suggestion of some oscillatory aspect to a new form of high-order EEG phase analysis is reasonable.

Further contributing to this reasonability, it may be said that the electrophysiological ion transport origin of the EEG (i.e., the action potential) and above oscillatory phase coupling behaviour across spectral frequencies as indicated by periodic bicoherence contours, are together broadly consistent with other findings involving oscillatory behaviour within the area of ion transport and cellular communication (e.g., broad consistency with the findings of a calcium signalling study [55]). That study demonstrates how Ca^{2+} ions regulate a wide spectrum of cellular processes and examines the frequency encoding of cytosolic Ca^{2+} concentration oscillations. The oscillatory Ca^{2+} concentration patterns display large spatial and

---

[1] Note that EEG oscillations of various forms are well known (e.g., within EEG burst segments [32]), and any prominent spectral peak (i.e., alpha or other) within the conventional EEG frequency spectrum must mathematically trace to an oscillatory component of the original time-domain waveform.

temporal diversity with suggestions of both amplitude and frequency modulation akin to conventional radio broadcast communication, and the oscillatory behaviour originates from an intricate concert action between several Ca^{2+} transporters at the cellular level [55].

Thus, the potential for some manner of deliberately structured oscillations across the frequency spectrum of the EEG, and more broadly across cellular communication processes, provides a justified basis for the application of a new form of high-order analysis, whereby a Fourier (or similar) transformation is applied to conventional EEG *frequency* spectra. That is, the study's commencing modus operandi requires a Fourier transformation to be twice applied to time-domain EEG data. From this point forward such double application is assigned the notation, FT', with the physical significance and implications of FT' in terms of CNS impulse encoding presented throughout.

2. THEORY

As justified above, the present study is founded upon a fast Fourier transformation (FFT) being twice applied to time-domain EEG data and assigned the notation, FT', with the second FFT applied to the AC components of the EEG's conventional amplitude versus frequency spectrum. For an N-point EEG acquired with a sampling frequency and time of f_s and T respectively, standard FFT analysis yields a maximum spectral frequency of $f_{max} = f_s/2$ and a frequency resolution of $\Delta f = f_s/N$. FT' in turn reverts to a time-domain with a maximum of $T'_{max} = T/2$ and resolution of $\Delta T' = 2/f_s$. This resolution of the (N/4-point) FT' spectrum is more coarse than the original time-domain's resolution for which $\Delta T = 1/f_s = T/N$ as is standard.

The physical interpretation of FT' may be approached from original time-domain or literal transformation viewpoints, though both viewpoints ultimately have the same mathematical origin. The first-mentioned viewpoint considers the time-domain characteristics of the EEG that lead to FT' characteristics. This viewpoint is complex since the FT' does not simply return a waveform to its original time-domain form and different time-domain waveforms may result in the same FT' spectrum (hence the use of "effective time" as a domain descriptor from this point). As an example of this latter uniqueness issue, two simple test waveforms that are symmetrical, whereby amplitude or phase symmetrically steps up versus steps down in time, will have the same FT' spectrum. While the FT' spectrum is naturally reflective of the degree to which the original time-domain fluctuates, visualisation of how the original time-domain waveform influences the final FT' is representative of a substantial study in its own right.

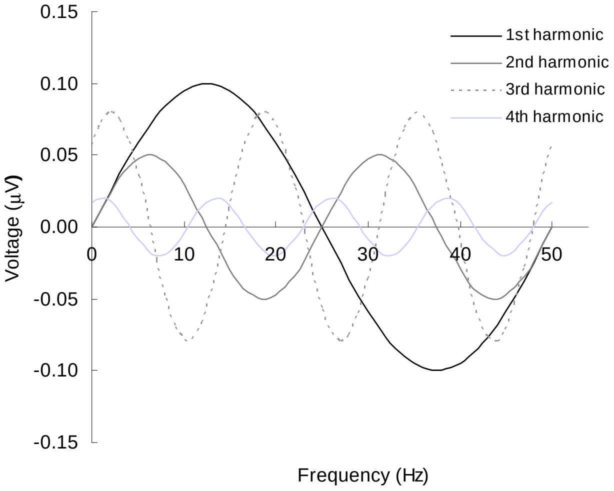

FIGURE 3. **Representation of the physical decomposition of a conventional frequency spectrum resulting from a double Fourier transformation, or *FT'*, process.**

The more easily visualised FT' viewpoint or physical interpretation simply deconstructs the conventional frequency spectrum of the FFT (or comparable algorithm) into sinusoidal harmonics (plus standard DC offset term) that are functions of frequency rather than time, with an additional oscillation occurring across the conventional frequency spectrum with each successive harmonic, as per figure 3 showing the first four harmonics (representative only) of FT' deconstruction. It follows, and is visually apparent, from figure 3 that the amplitude of any given conventional FFT harmonic (i.e., the amplitude of the conventional FFT spectrum at a particular frequency) is constructed from the sum of all FT' harmonics at that chosen frequency. Due to the now sinusoidal linkage of conventional FFT amplitudes and allowed phase movements between the FT' harmonics, such an across-frequency depiction results in high degrees-of-freedom and frequency couplings far beyond second-order.

The FT' spectrum is insensitive to phase constancy in the original time-domain, which is consistent with its derivation from the FFT amplitude (rather than phase) spectrum. That is, spectral characteristics of the FT' will not be attributable to the constant phases of the conventional FFT harmonics. However, the FT' spectrum is sensitive to *changing phases* (modulatory or otherwise) within the constituents of the original time-domain waveform, which are expected to occur in practice. For example, a simple modulation in phase of a conventional harmonic will introduce an oscillation within the FT', with the magnitude of the FT' oscillation being proportional to the magnitude of the original modulation. This manner of phase sensitivity potentially negates the need for division of the original time-domain waveform into epochs, which is a limiting requirement of some existing phase-based analysis techniques as per Subsection 1.2.

3. METHOD

3.1 EEG DATA FOR ANALYSIS

Two EEG data sets were constructed from independent sources so as to represent several clinically dissimilar scenarios and provide opportunity for technique validation and comparison across diverse neurological states. Data set construction also covered relatively short and long T values with the intention of capturing high-order phase relationships that might occur over relatively short and long time scales whilst also defining relatively fine Δf values (values of all signal processing parameter combinations are specified in Subsection 3.2). The data sets pertaining to nine adult subjects are described as follows:

3.1.1 EEG DATA SET 1 (SHORT T)

The first EEG data set pertains to two adult subjects, one classified as young and healthy, and the other as elderly with a probable Alzheimer's disease diagnosis. Data for these two subjects were collected by [56] in both eyes-open and eyes-closed states for all standard 19 channels of the international 10-20 referencing system of electrode placement [57], with all channels simultaneously sampled at $f_s = 128$ Hz for 8 s. Utilisation of this data within the present study focused on prefrontal (Fp1) and occipital (O2) electrode placements as specified throughout the continuing methodology and results to follow.

3.1.2 EEG DATA SET 2 (LONG T)

The second EEG data set pertains to seven healthy adult subjects undergoing clinical sleep (full overnight polysomnographic) studies and, for cross-sectional validation purposes, represented a compilation from sources that included [58] and [59] which are accessible via, and detailed within, the well-established PhysioNet database [60]. Note that while [58] and [59] include symptomatic subjects, only control subjects with no pathology were selected for the compilation (e.g., a subject chosen from the sleep apnoea study of [59] had an apnoea-hypopnoea index, or AHI, of < 5 and was therefore considered normal).

Complied data had been continuously scored for sleep stage over contiguous 30 s intervals whereby each interval was assigned either: awake, stages 1 to 4 (4 being the deepest stage), or rapid-eye-movement. Data from a wide range of conventional polysomnographic electrode placements are available within the compilation sources; those utilised by the preset study predominantly focused on central (C3 or C4) and occipital (O2) electrode placements, with further specification given as results are presented. A wide range of f_s values are similarly available within the sources and see Subsection 3.2 for comments on the seemingly low, but deliberate strategy behind, chosen f_s values that ranged from 100 to 200 Hz.

3.2 HIGH RESOLUTION FFT OF DATA SETS

An FFT was applied (using National Instruments Labview 2016 full development system software) to Data Sets 1 and 2 so as to achieve high resolution frequency spectra of $\Delta f = 0.125$ and 0.005 Hz respectively, in-turn equating to respective signal processing values of $N = 1024$, $T = 8$ (Data Set 1) and $N = 20{,}000$ to 40,000, $T = 200$ s (Data Set 2). Given the extended (overnight) duration of the EEG waveforms within Data Set 2, the 20,000- to 40,000-point FFTs based on $T = 200$ s are representative of select segments of any given EEG. These segments of the total EEG were chosen to allow comparison across a range of sleep stages. While not a key comparison index of the present study, SEF with a 95% cut-off was routinely calculated as a general assessment indicator for all frequency spectra.

The seemingly low $f_s = 100$ Hz value utilised within Data Set 2 related to stage 4 sleep EEG segments for one subject only. For these EEG segments, SEF was less than 30 Hz and so the appropriateness of $f_s = 100$ Hz is maintained in accordance with the Nyquist sampling theorem. The maximum SEF in all other cases was less than (most often appreciably) 55 Hz, with remaining f_s values comfortably meting corresponding Nyquist requirements. The discipline's trend towards relatively higher f_s (e.g., $f_s > 250$ Hz), alluded to within Subsection 1.2, was not followed to avoid or minimise the computation of FFT harmonics at impractically high f_{max} that would otherwise result from the relatively long T (and fine Δf) values utilised.

3.3 FT′ ANALYSIS OF DATA SETS

3.3.1 SECOND FFT APPLICATION

An FFT was applied to all AC components of conventional amplitude versus frequency spectra of Subsection 3.2 to yield corresponding FT' amplitude and phase spectra, in accordance with the prior Theory Section. For Data Set 1, FT' spectra from electrode channels 1 to 12 (prefrontal, frontal, central, temporal T3/T4) and from channels 13 to 19 (occipital, parietal, temporal T5/T6) were also combined to give average FT' spectra for these electrode groupings for both subjects and both eyes-open and closed-states. FT' phase profiles were shifted from a relative range of -180 to $+180^{\circ}$ (the FFT default) to a relative range of 0 to $+360^{\circ}$ to aid visualisation. As part of technique validation testing, the effect of windowing (Blackman, Hanning and Hamming) EEG data on FT' spectra was recorded for select EEG segments of Data Sets 1 and 2.

3.3.2 PHASE ANALYSIS OF FT′ SPECTRA

In addition to standard functional relationship analysis of warranting FT' spectra (e.g., linearity analysis of profiles for stage 4 sleep), continuing (deeper) phase-based analysis was applied to a selection of FT' spectra derived from both data sets. For Data Set 1, prefrontal and occipital eyes-closed EEG were chosen for this continuing analysis since such electrode placement combinations allow for useful, contrasting clinical bicoherence comparison [39] and occipital EEG with eyes-closed provides strong EEG and alpha signals (the posterior dominant rhythm, or PDR, is enhanced during relaxed wakefulness [4,61]). Strong alpha activity is a focus of the present study’s cross-sectional comparison because: (i) literature now links alpha activity to not just relaxed consciousness and passive attention, but additionally to active roles in neural network communication and co-ordination including short-term memory and working memory retention [51], and (ii) conventional spectral peaks might conceivably be linked to quantum mechanical resonances (see Evidence of a Quantum Nature Subsection 5.5). Accordingly, FT' spectra derived from Data Set 2 and selected for this continuing phase analysis also displayed conventional spectral peaks (including sigma sleep spindle) for states from relaxed consciousness to stages 1 to 3 sleep.

The continuing phase analysis of FT' spectra was based upon discrete phase transitions, $\Delta\phi$, observed within many non-stage 4 sleep spectra (from this point ϕ, representative of conventional harmonic phase, dually represents FT' harmonic phase). These $\Delta\phi$ are described throughout as "upward" when the FT' phase profile markedly steps up (from some local minimum to an adjacent local maximum) as a function of effective time. Conversely, $\Delta\phi$ are described throughout as "downward" when the FT' phase profile vertically steps down (from a local maximum to an adjacent minimum) as a function of effective time, with the final descriptor of "horizontal" applying to $\Delta\phi$ between local maxima of FT' phase profiles. Analysis involved the construction of a polar plot (phase wheel) of $\Delta\phi$ values for each FT' phase profile (with $\Delta\phi$ values referred to as radials within phase wheels). Any radial alignment to within $\pm 0.5^{o}$ of conventional landmark trigonometric angles (e.g., 30^{o}, 45^{o}, 60^{o}, 90^{o}, and counterparts within quadrants two to four), referred to here as primary radials, was indicated within phase wheels. The study’s design initially applied broad defining criteria as to what constitutes a primary radial (which initially also included integer and common fraction multiples of 20^{o} not already specified), but progressively applied self-refinement of these defining criteria in accordance with the remaining Method Subsections. Hence, the term *potential* primary radial is initially used within the Results Section.

Within phase wheels, the ratios of sector angles (for sectors formed between radials and other radials or primary radials) that align to within 1.0% of some common fraction were also identified. Such alignment testing represented a rudimentary but necessary initial aspect of a deeper phase-based analysis for upward $\Delta\phi$, the full description of which continues within the following Subsections.

3.3.3 CHI-SQUARED STATISTICAL ANALYSIS OF $\Delta\phi$ RADIALS

A frequency of occurrence distribution based upon all upward $\Delta\phi$ from seven (cross-sectionally representative) phase wheels was generated with a distribution resolution of $\delta\phi = \pm 0.5^{o}$ applied. A second frequency of occurrence distribution was generated with transitions from 180 to 360^{o} converted to complementary angles from 0 to 180^{o} (e.g., $355^{o} \equiv 5^{o}$ and so on), with conversion rationale given within the Discussion. Respective null hypotheses of expected normal $\Delta\phi$ distributions from 0 to 360^{o} and 0 to 180^{o} were tested via standard chi-squared analysis with an applied significance threshold of $p < 0.001$. For any unexpected distribution, polar angles about which $\Delta\phi$ values clustered were recorded for further analysis.

3.3.4 BINOMIAL DISTRIBUTION STATISTICAL ANALYSIS OF $\Delta\phi$ RADIALS

For individual and combinations of phase wheels, binomial distribution analysis gave the probability, P, of $\Delta\phi$ values aligning with predetermined primary radials, with predetermination based upon both the prior-stated landmark polar angles and any radial angle about which an unexpected clustering of $\Delta\phi$ values may have occurred, as identified by the above chi-squared analysis. The P of alignment of h (from a total of H) radials with any of m primary radials, to within a resolution of $\pm\delta\phi$ radians, for individual or combinations of phase wheels, is given from binomial probability theory [62] by (1):

$$P = {}^{H}_{h}C \left(\frac{m\delta\phi}{\pi}\right)^{h} \left(1 - \frac{m\delta\phi}{\pi}\right)^{H-h} . \qquad (1)$$

3.3.5 ITERATIVELY LINEARIZED FAMILY ANALYSIS OF $\Delta\phi$ RADIALS

Based on the frequency of occurrence distribution applied to all upward $\Delta\phi$ radials from the seven phase wheels to which chi-squared analysis was applied, any irregular clusterings of $\Delta\phi$ about particular polar angles were said to form potential "Families" about these polar angles. For each potential Family, the separations between intra-Family radials were calculated and written in terms of quarter- or third-integer ($k = j/4$ or $j/3$, $j = 1, 2, 3 \ldots$) amounts of some to-be-determined proposed quantum increment value, α, such that separation is given by $k\alpha$ (note that the α notation is independent of the "alpha" activity descriptor of conventional EEG frequency spectra). The α value for each established Family was extracted as the gradient of a (zero y-intercept) graph of separation versus k multiplier in an iterative manner. The iterative linearization process involved a separation acceptance/rejection threshold of 1.0% difference between the actual separation and separation given by $k\alpha$. That is, α was recalculated upon each iteration until only separations with residuals of less than 1.0% were included within the linear regression (that applied $r > 0.9999$, $p < 0.001$ Family acceptance thresholds) used for the determination of α, with a 95% confidence interval (CI) that was established via application of a *t*-distribution to the gradient's standard error.

The original iterative method above may be seen to have parallel with the recursive method [32] (adapted from that of [53]) of accepting/rejecting elements contributing to *k*th-order self-phase coupling (where the phase of an element is *k* times the phase of another) within bicoherence indices. However, while such precedents exists for an expectation of phase multiples within high-order self-coupling, here the described *k*α iterative approach is based on the unique quantisation postulate that harmonics of increasing order as depicted by the physical deconstruction of figure 3 may potentially be separated by quantised phase increments which play a role within some to-be-determined form of discrete phase-shift keying (PSK) communication encoding [2,63].

Finally, the existence of any functional relationship between identified α values across all Families was investigated. Because individual Family α values may be readily scaled (e.g., $\alpha' = 2\alpha$ say) with the required 1/4 or 1/3 transition separation multiplicity condition still maintained, relationship identification is potentially straight forward. Thus, any α scaling and relationship finalisation was based on correlation maximisation (the regression for which propagated α error via a Monte Carlo approach that easily achieved model parameter convergence to required confidence levels via 800 simulation iterations) along with α scaling reasonability such that the smallest separations[2] within each Family corresponded to low *k* values (e.g., ¼, ½ and 1). This finalisation in turn allowed for factors such as the overall occupancy of Families, and the extent to which these occupancies involved $k = j/2$ separation multiples (only) of α, to be considered for the potential classification of Families (e.g., as primary or secondary following an analogous quantum classification system), and indeed whether a certain type of α multiplicity is preferred within Families. Note that $k = j/2$ multiples are of particular interest because of the fundamental commonality of full- and half-integer augmentations across many and various quantum systems.

4. RESULTS

This Section, for which conventional FFT and corresponding *FT′* spectral outcomes are generated from 31 example EEG segments pertaining to nine different subjects, is structured into two levels of analysis, Subsections 4.1 and 4.2. Within the latter Subsection, which contains the present study's foremost findings (with appropriate levels of statistical confidence), all *FT′* phase profiles that display characteristic discrete upward Δϕ are combined within an overall analysis that provides insight into the mathematical structure of CNS signal encoding for a broad spectrum of neural states. Other than the revelation of such insight, the present study is non-clinical, aiming to mathematically introduce and demonstrate the physical efficacy of the new EEG analysis technique to pave the way for future clinical studies. Hence, the snapshot spectral comparisons that follow within Subsection 4.1 are not for the purpose of clinical differentiation or diagnosis. To assist mathematical visualisation, spectra and associated analyses involving phase are displayed throughout in units of degrees, though dual radian equivalence is adopted in select cases.

4.1 LEVEL 1 ANALYSIS: EXAMPLES AND OVERVIEW OF FT′ SPECTRAL CHARACTERISTICS

Example *FT′* spectra presented and compared within this Subsection contain harmonic amplitude and phase profiles in the same graph (i.e., such graphs contain dual *y*-axes).

4.1.1 CROSS-SECTION OF FT′ EXAMPLES FOR T = 8 s DURATION EEG SEGMENTS (DATA SET 1)

An example alpha-active conventional FFT spectrum and its corresponding *FT′* spectrum, for occipital (O2) electrode placement upon the healthy subject with eyes-closed of Data Set 1, are respectively shown in figures 4a and 4b. The alpha peak accounts for approximately 28% of the spectrum integral in figure 4a. For comparison, figures 4c and 4d respectively show conventional FFT and corresponding *FT′* of reduced alpha activity simultaneously collected from the same subject for prefrontal (Fp1) electrode placement. Select upward Δϕ of figure 4b are annotated with lower-case alphabetical labels, while select local maxima are annotated with a degrees label given by shifting the relative phase scale by a further -100.7^{o} and rounding to the nearest integer (the actual shifted phase values of local maxima thus equal their corresponding rounded labels to within $\pm 0.5^{o}$). The values of all labeled quantities and their quantified alignment with landmark polar angles are given in table A1 of Appendix A.

Note that while *FT′* spectra extend beyond $t' = 1.0$ s, the *FT′* amplitude profiles generally decay to some relatively low baseline (albeit fluctuating) by this effective time. Hence, this initial 1.0 s decay period of *FT′* spectra is a focus for presented results and later discussion. Similar comparative outcomes (not graphically shown) in terms of general overall *FT′* amplitude profile shape are obtained when averaging the *FT′* profiles of EEG channels 13 to 19 (see Subsection 3.3.1 for electrode placement descriptors) and comparing against the average of the *FT′* profiles for EEG channels 1 to 12.

Figure 4e presents a phase wheel displaying all (not just selectively labeled) upward Δϕ of Figure 4b via solid radials (of any colour), and the corresponding table 1 respectively gives phase wheel sector ratio values that align to within 1.0% of some identified nominal common fraction. The percentage differences between actual and nominal ratio values are bracketed within the central

---

[2] This α scaling reasonability for the smallest separations included those outside of the 1.0% alignment threshold, if the two Δϕ radials of any such separation were individually involved in other separations that met the 1.0% threshold.

column of table 1, with ratios falling outside 1.0% alignment but still worthy of qualitative note shown in light shaded text. Where a ratio involves a sector formed with a *potential* primary radial, that potential primary radial is noted within both table 1 (right-hand column) and figure 4e (as a dashed radial which in several instances is fully or partially overlapped by an actual Δϕ radial – see table A1 for degree of overlap). Orange radial colouring reflects such overlapping with other colourings reflecting some connectedness in terms of sector formation. Also within figure 4e, dashed lines annotated as "mid" represent the polar location symmetrically between radial pairs. Table A2 gives select sector angle values for figure 4e.

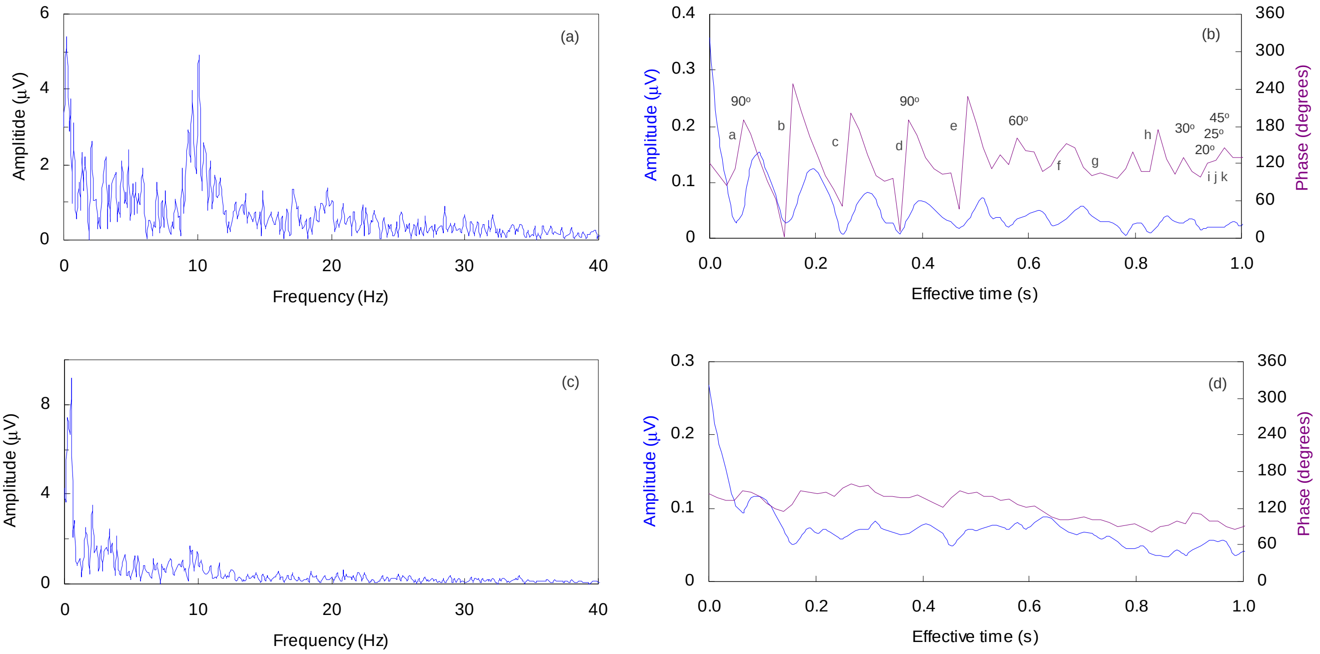

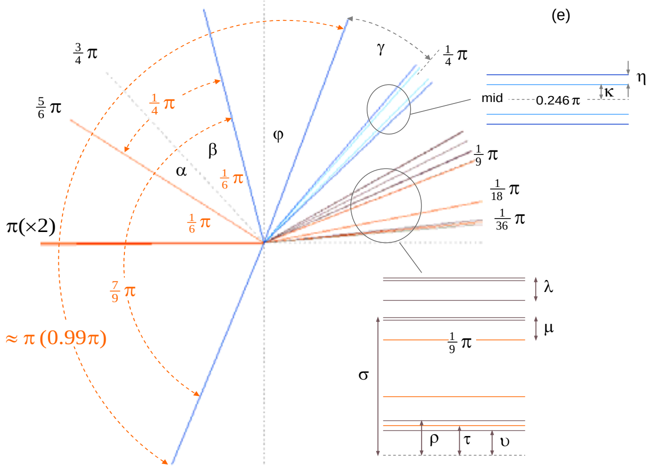

Table 1. Common fraction alignment of sector ratios within the figure 4e phase wheel, and potential primary radials involved in sector formation.

Sector ratio	Sector ratio value (% difference from common fraction)	Primary radial involved with sector formation (radian equivalent)
λ:μ	1:1 (< 0.01)	20° (1/9 π)
η:υ	1:4 (0.3)	–
ρ:σ	1:4 (0.6)	10°, 20° (1/18, 1/9 π)
η:κ	2:3 (0.8)	45° (1/4 π)
α:β	1:2 (2.4)	135°, 150° (3/4, 5/6 π)
φ:γ	1:1 (2.5)	–

The indicated 1/4 π sector angle within the second quadrant of figure 4e is measured to the exact 5/6 π primary radial.

Sector ratios of 1:1, 1:2 and 2:3 are also inherently implied by the alignment of Δϕ radials with primary radials in figure 4e.

FIGURE 4. Conventional frequency spectra of a healthy adult subject with eyes-closed for (a) occipital (O2) with relatively high alpha activity and (c) prefrontal (Fp1) EEG. For each conventional frequency spectrum the corresponding (adjacent) double Fourier transformation of the EEG, or *FT′* spectrum, is respectively given in (b) and (d). Annotated local maxima labels in (b) are generated by adding –100.7° to the relative phase scale of the right vertical axis and rounding the resulting maxima values to the nearest integer. All upward Δϕ of (b) are displayed as radials within the phase wheel of (e), with notable ratios of phase wheel sector angles given within the adjacent table 1 (sector angle symbolism is generic and separate to any elsewhere duplication).

Figures 5a and 5b respectively show conventional FFT and corresponding *FT′* spectra for occipital (O2) electrode placement upon the probable Alzheimer's subject with eyes-closed of Data Set 1, with figures 5c and 5d showing equivalent spectra for simultaneously collected prefrontal (Fp1) electrode positioning. Select local maxima in figures 5b and 5d are annotated with degree labels given by respectively shifting their relative phase scales by -178.2^{o} and -154.8^{o}, and then rounding to the nearest integer; the values of labeled quantities are again given in table A1.

Phase wheels following the conventions of figure 4e and corresponding to figures 5b and 5d are respectively given in figures 5e and 5f (note that results presented within Subsection 4.2 and the later Discussion Section refine and justify what constitutes a primary radial within such figures). Table 2 gives phase wheel sector ratio values that align to within 1.0% of some identified nominal common fraction, while table A2 gives select sector angle values for figures 5e and 5f.

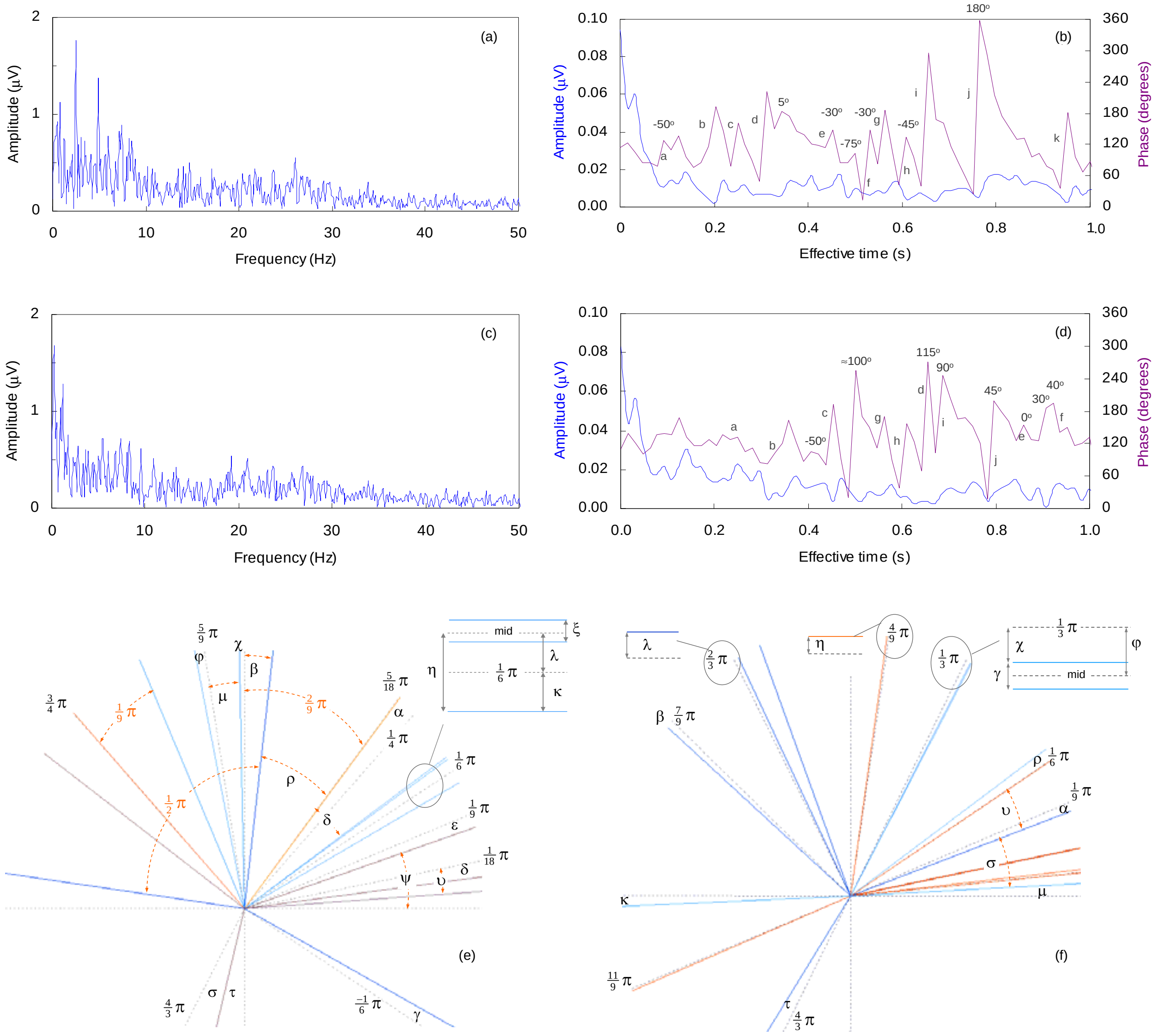

FIGURE 5. **Conventional frequency spectra for elderly subject diagnosed with probable Alzheimer's disease with eyes-closed for (a) occipital (O2) and (c) prefrontal (Fp1) EEG. For each conventional frequency spectrum the corresponding (adjacent) double Fourier transformation of the EEG, or *FT′* spectrum, is respectively given in (b) and (d). Annotated local maxima labels in (b) and (d) are generated by respectively adding -178.2^{o} and -154.8^{o} to the relative phase scale of the right vertical axis and rounding the resulting maxima values to the nearest integer. All upward $\Delta\phi$ of (b) and (d) are respectively displayed as radials within the phase wheels of (e) and (f), with notable ratios of phase wheel sector angles given within table 2 (sector angle symbolism is generic and separate to any elsewhere duplication).**

Table 2. Common fraction alignment of sector ratios within figures 5e and 5f, and potential primary radials involved in sector formation.

Sector ratio	Sector ratio value (% difference from common fraction)	Primary radial involved with sector formation (radian equivalent)
figure 5e		
$\gamma:\beta$	1:2 (0.02)	-30°, 90° (-1/6, 1/2 π)
$\upsilon:\psi$	3:8 (0.2)	10°, 360° (1/18, 2 π)
$\chi:\varphi:\eta$	1:2:5 (0.3)	30°, 90°, 100° (1/6, 1/2, 5/9 π)
$\kappa:\lambda^{\#}$	1:1 (0.9)	30° (1/6 π)
$\eta:\mu$	2:3 (0.9)	30°, 100° (1/6, 5/9 π)
$\delta:\psi^{*}$	1:5 (< 1.0)	10°, 50°, 360° (1/18, 5/18, 2 π)
$\varepsilon:\lambda$	1:1 (1.2)	20°, 30° (1/9, 1/6 π)
$\alpha:\beta^{*}$	2:3 (1.3)	45°, 50°, 90° (1/4, 5/18, 1/2 π)
$\delta:\rho^{*}$	1:1 (2.0)	50° (5/18 π)
$\sigma:\tau$	1:1 (2.0)	300°, 270° (-1/3, 3/2 π)
figure 5f		
$\varphi:\rho$	1:2 (0.04)	30°, 60° (1/6, 1/3 π)
$\gamma:\eta$	2:3 (<0.10)	60°, 80° (1/3, 4/9 π)
$\upsilon:\sigma$	3:4 (0.2)	30° (1/6 π)
$\alpha:\tau$	1:2 (0.2)	20°, 240° (1/9, 4/3 π)
$\rho^{**}:\mu$	1:1 (0.5)	30°, 360° (1/6, 2 π)
$\varphi:\mu$	1:2 (0.6)	60°, 360° (1/3, 2 π)
$\lambda:\beta$	2:3 (0.8)	120°, 140° (2/3, 7/9 π)
$\chi:\kappa$	1:2 (1.4)	60°, 180° (1/3, 1 π)
$\alpha:\beta$	1:1 (1.6)	20°, 140° (1/9, 7/9 π)
$\eta:\varphi$	2:5 (1.6)	60°, 80° (1/3, 4/9 π)

[#] Angles κ and λ are measured about the exact 1/6 π primary radial in figure 5e.

[*] Angles ρ, δ and α are measured to the Δϕ radial that aligns near the exact 5/18 π primary radial in figure 5e.

Sector ratios of 1:2, 4:9 and 2:9 are also inherently implied by the alignment of Δϕ radials with primary radials in figure 5e.

[**] Angle ρ is measured to the exact 1/6 π primary radial in figure 5f.

Sector ratios of 1:2, 1:3, 1:4, 1:6 and 3:4 are also inherently implied by the alignment of Δϕ radials with primary radials in figure 5f.

4.1.2 CROSS-SECTION OF FT′ EXAMPLES FOR T = 200 s DURATION EEG SEGMENTS (DATA SET 2)

Note that for this Subsection the hash numbering of subjects within figures is consistent with anonymous numerical identifiers used by the original cited data sources that compile (overnight polysomnographic) Data Set 2. Figures 6a and 6b respectively show example conventional FFT and corresponding *FT′* spectra for an occipital (O2) EEG segment for which the subject is in a state generally described as possessing both awake and significant stage 1 sleep components (with the multi-stage description indicative of sleep scoring at 30 s intervals within the relatively long $T = 200$ s EEG segment). An oscillatory ϕ profile with approximate linear decay, as exemplified by figure 6b, is a common characteristic of sleep *FT′* phase profiles, especially when conventional FFT peaks (e.g., alpha, sigma sleep spindle) are present, in which case the amplitude of ϕ oscillation is generally indicative of peak dominance and decreases with increasing sleep depth. As per Subsection 4.1.1, upward Δϕ of oscillations within spectra such as figure 6b are more formally analysed within Subsection 4.2. For later comparison purposes, the gradient of the phase profile in figure 7b, with error margin at 95% CI, is $d\phi/dt' = -141 \pm 6^{o}{\cdot}s^{-1}$ based on linear regression modelling ($r = -0.987$, $p < 0.001$).

Figures 6c and 6d respectively show example conventional FFT and corresponding *FT′* spectra for a central (C4) EEG segment for a subject in stage 4 sleep. A model trend line based on linear regression of the phase profile in figure 6d, over a selected domain of interest ($0.1 \le t' \le 0.7$ s), is given in figure 6e stacked alongside similarly derived trend lines for five other $T = 200$ s stage 4 sleep segments of the same overnight EEG recording (hence the six consecutive segments, each separated by 10 s, represent a total stage 4 sleep analysis time of 20.8 min for the same subject). Stacking is achieved by progressively (chronologically) vertically shifting each successive series by an additional 40°. Comparison figure 6f is derived in a similar manner for another subject in extended stage 4 sleep and for the same electrode placement. Note that domain commencement at $t' = 0.1$ s in figures 6e and 6f is due to a slight deviation from linearity over the domain $0.0 \le t' \le 0.1$ s for some such phase profiles (not apparent within figure 6d), and so the domain $0.1 \le t' \le 0.7$ s is maintained to allow consistent comparison across figures. Also, *y*-error bars in figures 7e and 7f are smaller than the graphical markers utilised and not resolvable by the figures' scales.

Annotated in figures 6e and 6f are 95% CI $d\phi/dt'$ values and linear regression statistics ($-r \ge 0.990$, $p < 0.001$ in all cases). Within these figures, $d\phi/dt'$ ranges from -163 ± 9 to $-203 \pm 7^{o}{\cdot}s^{-1}$ (3.3%) and -166 ± 6 to $-206 \pm 4^{o}{\cdot}s^{-1}$ (3.7%) respectively, with bracketed values giving the average of all intra-figure error margins when the margins are expressed as a percentage. A third similar stage 4 sleep analysis example (not graphically shown) gives a $d\phi/dt'$ range of -190 ± 5 to $-236 \pm 8^{o}{\cdot}s^{-1}$ (2.5%).

Figure 6g focuses upon the first of the phase profiles in figure 6e and is therefore associated with the commencement of the extended 20.8 min stage 4 sleep analysis. This focused-upon profile demonstrates sight oscillatory behaviour, possibly attributable to some residual (less-deep) sleep component, and is partially mirrored by figure 6g's additional phase profile simultaneously collected for prefrontal (Fp2-F4) electrode placement (discussed within Subsection 5.6.1).

Notwithstanding later general discussion that naturally generates from figures 6e and 6f and associated results, since a detailed clinical study into stage 4 sleep is not an aim of the present study, these stage 4 sleep results are primarily intended to demonstrate repeatable linear characteristic outcomes of the new technique (that are in stark contrast to the chaotic-like first-order phase behaviour of conventional EEG frequency spectra.

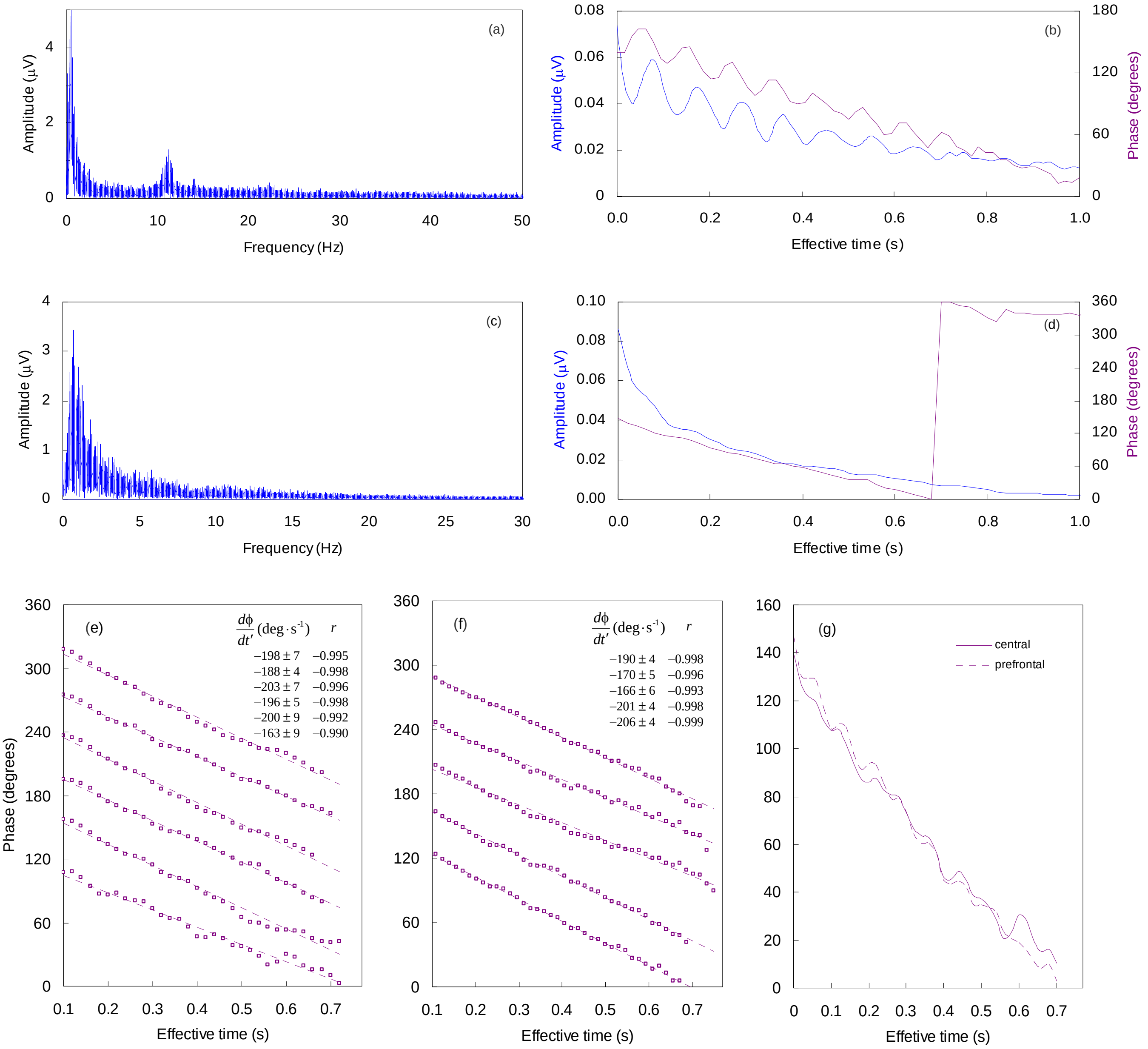

FIGURE 6. **A conventional frequency spectrum (with alpha peak) for subject #7 [58] categorised as awake/stage 1 sleep for occipital (O2) electrode placement is given in (a) with the corresponding double Fourier transformation of the EEG, or *FT′* spectrum, given in (b). A similar spectral pair for subject #16 [58] in stage 4 sleep and central (C4) electrode placement are shown in (c) and (d). A linear regression of the phase profile in (d) over the domain $0.1 \leq t' \leq 0.7$ s is given in (e) (third-from-bottom trend line) which also stacks five other stage 4 sleep trend lines of the same EEG recoding (the six consecutive EEG segments with 10 s separation yield a total stage 4 sleep assessment time of 20.8 min and see main text for manner of incremental stacking via relative phase shifting), with regression values given in the figure legend. Similar stacked profiles for subject #15 [59] in extended stage 4 sleep is given in (f). The first phase profile in (f) is zoomed within (g) along with a simultaneously collected phase profile for prefrontal (Fp2-F4) electrode placement.**

While not a focus of the present study ($\Delta\phi$ analysis being the focus), the average (mean ± SD) oscillation frequency of five *FT′* amplitude profiles that contain notable oscillatory form (e.g., figures 5b and 6b) is 9.7 ± 1.8 Hz.

Figures 7a and 7b respectively show example conventional FFT and corresponding *FT′* spectra for an EEG segment of an awake subject in sleep preparedness and for occipital (O2) EEG; the relatively uniform FFT is without appreciable alpha or similar spectral peak. The smoothness of the *FT′* amplitude and phase profiles in figure 7, that reflect the FFT uniformity, is an atypical but nevertheless repeatable *FT′* characteristic. The decays of profile tails in figure 7 follow simple exponential functionality but overall are more accurately modelled via exponential functionality of the form $e^{-t'^{x}/\tau}$, where for a given profile τ is a standard time constant and the exponent, x, ranges from approximately 0.70 to 0.85 (again, $\Delta\phi$ analysis rather *FT′* profile decay functionality is the focus of the present study and therefore decay functionality is presented in a generalised context).

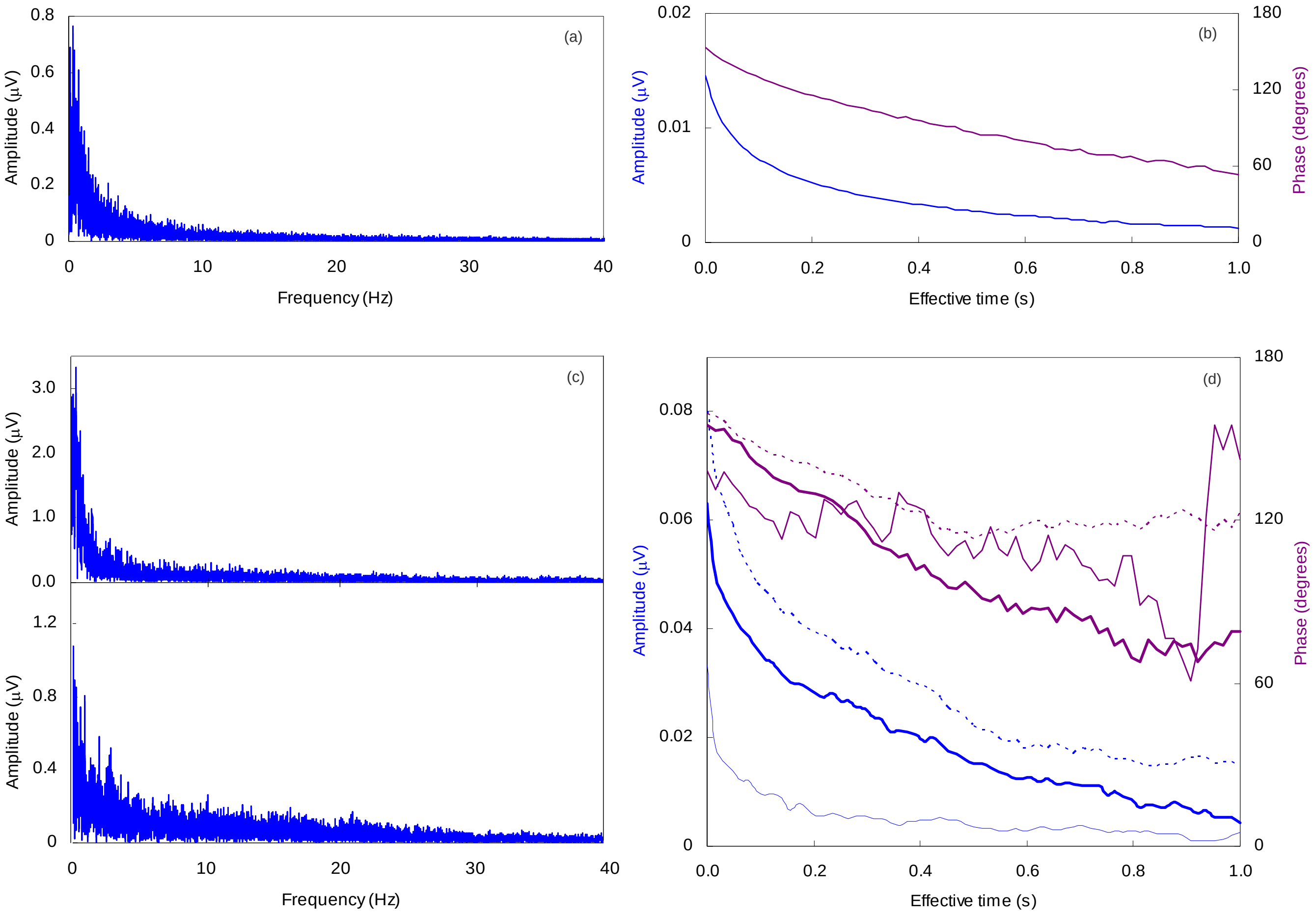

FIGURE 7. **Conventional frequency spectra for subjects #6 and #9 [58] in sleep preparedness and for occipital (O2) electrode placement are respectively given in (a) and (c), with the two spectra of (c) associated with two separate EEG segments (recording times) for subject #9. For each conventional frequency spectrum the corresponding (adjacent) double Fourier transformation of the EEG, or *FT′* spectrum, is respectively given in (b) and (d). Also shown by dashed lines in (d) are *FT′* profiles for central (C3) electrode placement for subject #9, but again for a different EEG segment (corresponding FFT not shown but similar to those in (c)).**

Figure 7d shows three sets of similar profiles for another subject in sleep preparedness; one set associates with central (C3) electrode placement (dashed) and the other two sets associate with occipital (O2) electrode placement (all three sets have different EEG recording commencement times within the same polysomnographic record). Corresponding conventional FFT spectra are given in figure 7c for the occipital *FT′* profiles (the central FFT profile is not shown but is similar to the given occipital examples). While tabulations of select $\Delta\phi$ (ala example table A1) are not presented, the dominant discrete transition of $\Delta\phi = 90^{o}$ in figure 7d, with slight symmetrical ϕ oscillation about the transitioned level, is worthy of note within the context of analysis and is called upon by later discussion. For broad comparison purposes only (a general rate trend for increasing sleep depth is later discussed), the 95% CI gradient for the phase profile of figure 7b over a selected domain of interest ($0.2 \le t' \le 1.0$ s) is $d\phi/dt' = -74 \pm 2^{o}\cdot s^{-1}$ (3%), based on an approximation of linear modelling ($r = -0.994$, $p < 0.001$).

Table 3. Frequency distributions of rounded $\Delta\phi$ values for radials from seven phase wheels combined.

$\Delta\phi$ (degrees)	Number of occurrences	$\Delta\phi$ (degrees)	Number of occurrences
5	4	4 – 6	7
10 & 11	4	9 – 11	7
18	4	18 – 23	14
20	3	26 – 33	14
22	2	50	2
27	3	80 – 81	3
30	2	178 – 180	3
33	5		
50	2		
59	2		
80 & 81	3		
180 – 182	3		
	36 out of 87 radials		50 out of 87 radials

4.2 *LEVEL 2 $\Delta\phi$ DISTRIBUTION ANALYSES*

4.2.1 CHI-SQUARED STATISTICAL ANALYSIS OF $\Delta\phi$ RADIALS

Based on a frequency of occurrence distribution applied to all 87 upward $\Delta\phi$ radials of seven phase wheels collectively representing a cross-section of subjects and clinical states, including relatively short and long analysis times over which high-order phase relationships might occur, the most repeated $\Delta\phi$ values (rounded to integer values for a distribution resolution of $\delta\phi = \pm 0.5^{o}$) are given, together with their frequency of occurrence, in the two left-most columns of table 3. The two right-most columns present similar frequency of occurrence results but with $\Delta\phi$ values from 180 to 360^{o} (constituting 17 of the 87 radials) converted to a complementary angle from 0 to 180^{o} (i.e., $355^{o} \equiv 5^{o}$ and so on, with conversion rationale given within the Discussion).

The null hypothesis of an expected normal distribution of $\Delta\phi$ values is excluded via chi-squared analysis for which 36 out of 87 radials align with 16 out of a possible 360 polar angle values (two left-most columns), and 50 out of 87 radials align with 26 out of a possible 180 polar angle values (two right-most columns). Associated chi-squared values are respectively: $\chi^2 = 303$, $df = 12$, $p < 0.001$ and $\chi^2 = 346$, $df = 7$, $p < 0.001$.

4.2.2 BINOMIAL DISTRIBUTION STATISTICAL ANALYSIS OF $\Delta\phi$ RADIALS

The following binomial distribution analysis considers primary radials at 5^{o}, 10^{o}, 20^{o}, 30^{o}, 45^{o}, 50^{o}, 60^{o}, 80^{o}, 90^{o}, 120^{o}, 135^{o}, 150^{o} and 180^{o}, with these primary radials based on landmark polar angles, individual phase wheel analysis, and the above frequency distribution results for all phase wheels combined. Note again that primary radials are provisionally defined and their ongoing refinement continues throughout this Subsection with finalisation rationale summarised within the Discussion.

For individual and combinations of phase wheels, the probability, *P*, of $\Delta\phi$ radials aligning with these primary radials is given within table 4, for which *P* is calculated in accordance with binomial probability theory and (1). Input parameters for (1), in addition to $m = 13$ as set by the above-defined primary radials, are given in table 4, and bracketed values within that table signify the effect of converting angles above 180^{o} to complementary angles in the range 0 to 180^{o}.

Table 4. Binomial probably of upward $\Delta\phi$ radial alignment with provisionally defined primary radials for various combinations of phase wheels.

Phase wheels	Phase wheel clinical descriptions	Total number of transitions, H	Number of alignments, h, between transitions and primary radials	Alignment resolution, $\pm\delta\phi$ (degrees)	Binomial probability of observed alignment, P
1 to 7	All scenarios	87	19	0.60	4.3×10^{-9}
1 to 6	All scenarios excluding approaching deep sleep	80	19	0.60	9.8×10^{-10}
figure 4e	Healthy adult	20	7	0.60	1.3×10^{-5}
figures 5e + 5f	Probable Alzheimer's	33	6	0.51	0.0010
4, 5 and 6	Light and mid sleep	28	6 (8)	0.50	3.7×10^{-4} (9.7×10^{-5})
7	Approaching deep sleep	6	0	0.50	0.64

4.2.3 QUANTISED STRUCTURE ANALYSIS OF $\Delta\phi$ RADIALS

Table 5 reveals identified Family $\Delta\phi_c$ values about which $\Delta\phi$ radials cluster and for which separations between clustering radials (Family members) can be written in terms of $k = j/4$ or $j/3$ $(j = 1, 2, 3 \ldots)$ multiples of a quantum increment value, α. The α value determined for each Family, $\alpha_{\Delta\phi}$, is given within table 5 along with 95% CI error margins, including for mean values, $\bar{\alpha}_{\Delta\phi}$. This Family $\Delta\phi_c$ and $\alpha_{\Delta\phi}$ analysis is based on the combined radials of seven phase wheels, and the previously described iterative linearization process of $\alpha_{\Delta\phi}$ determination which achieved correlation statistics of $r > 0.99998$, $p < 0.001$ for each Family.

Diagrams showing all radials and, where applicable, the separation between these radials in terms of $k\alpha_{\Delta\phi}$, are given for each Family in figure 8 (for which actual separation values align with their nominal $k\alpha_{\Delta\phi}$ form to within 1.0% unless the alignment is annotated as approximate). For these separations, table 6 gives the exact percentage difference between actual and nominal separations, with the average (mean ± SD) percentage difference for all Families combined being $0.39 \pm 0.28\%$ (i.e., most considered alignments are well within the 1.0% acceptance margin).

Table 5. Quantum increment values, $\alpha_{\Delta\phi}$, for each Family of $\Delta\phi$ radials, with ± error margins (EMs) at 95% CI including for mean values, $\bar{\alpha}_{\Delta\phi}$.

Family $\Delta\phi_c$ (degrees, radians)	$\alpha_{\Delta\phi}$ (degrees)	$\bar{\alpha}_{\Delta\phi}$ EM (degrees)
5, $\pi/36$	0.26534 ± 0.00205	0.00092
10, $\pi/18$	0.22734 ± 0.00123	0.00062
20, $\pi/9$	0.18193 ± 0.00070	0.00023
30, $\pi/6$	0.17685 ± 0.00027	0.00007
50, $5\pi/9$	0.28509 ± 0.00072	0.00019
90, $\pi/2$	0.98495 ± 0.00151	0.00033
135, $3\pi/4$*	2.5329 ± 0.0122	0.0055
180, π	4.9134 ± 0.0259	0.0116
220, $11\pi/9$*	7.7336 ± 0.0604	0.0302
270, $3\pi/2$	11.981 ± 0.090	0.040

* Considered non-primary or secondary Family.

Of the annotated radial separations in figure 8 that fall within the 1.0% acceptance margin, the percentage for each Family that involve only full- or half-integer $(k = j/2)$ multiples of $\alpha_{\Delta\phi}$ are as follows in ascending (degree) Family order: 60, 100, 86, 71, 79, 91, 60, 71, 50 and 80% (78% for all Families combined). Similarly, the percentage for each Family that only involve full-integer multiples $(k = j)$ in ascending Family order are: 40, 75, 43, 36, 64, 19, 60, 29, 0.0 and 40% (38% for all Families combined). Hence, for the annotated radial separations a strong preference exists across all Families for full- or half-integer multiples of $\alpha_{\Delta\phi}$ over other fractional multiples of $\alpha_{\Delta\phi}$ ($\chi^2 = 77$, $df = 1$, $p < 0.001$).

Note that within table 5, the $\Delta\phi_c = 135^o$ and 220^o Families are footnoted as non-primary or secondary Families (with remaining Families hence classified as primary). For the 135^o Family this relegation is based on the fact that all but one of the annotated separations involve a complementary radial (the only Family with an appreciable reliance on complementary radials). For the 220^o Family the relegation is based on relatively low occupancy and displaying the lowest percentage of full- or half-integer multiples of α within annotated radial separations (and furthermore being the only Family displaying no full-integer multiples). Also in contrast to other Families, these Families play lesser roles within table 7 which presents ratios of $\bar{\alpha}_{\Delta\phi}$, whereby ratio values align with nominal common fractions. The percentage differences between actual (exact median) and nominal ratio values are also presented within table 7, along with actual ratio values with error margins at 95% CI (following quadrature error combination). For that table, ratios are classified as: Tier 1 upon the formation of a *simple* common fraction involving *primary* Family members; Tier 2 upon the formation of a *complex* common fraction involving *primary* Family members; and Tier 3 upon the formation of a *complex* common fraction involving a *secondary* Family member.

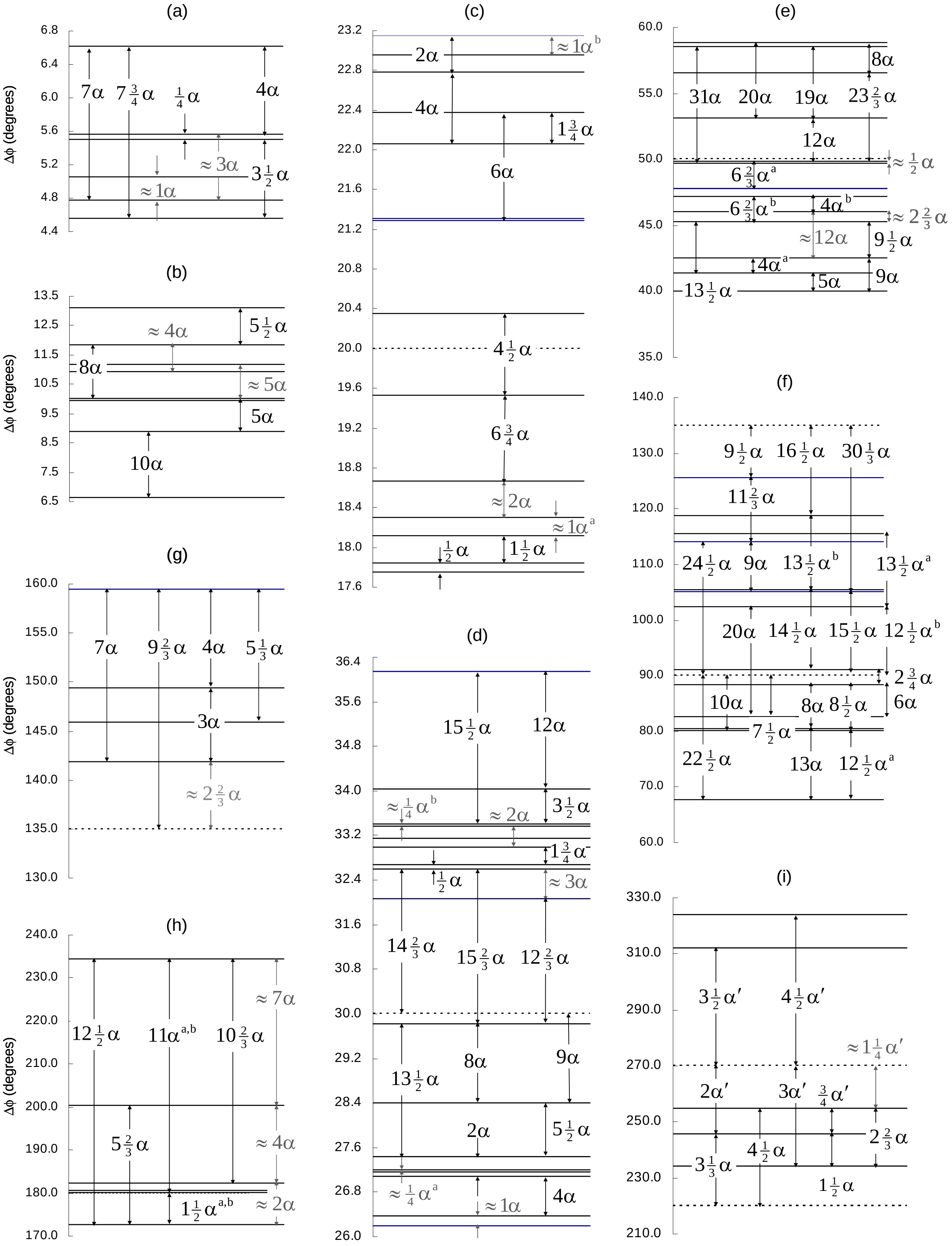

FIGURE 8. **All $\Delta\phi$ radials from seven phase wheels (and thus seven *FT*'s) grouped within the Families of $\Delta\phi_c$ = (a) 5°, (b) 10°, (c) 20°, (d) 30°, (e) 50°, (f) 90°, (g) 135°, (h) 180°, and (i) 220° & 270° (combined). Shown for each Family are radial separations that align with integer and fractional multiples of some quantum transition value, $\alpha_{\Delta\phi}$ (see table 5 for $\alpha_{\Delta\phi}$ values). In (i) α and α' respectively indicate $\alpha_{\Delta\phi}$ for the 220° and 270° Families. Each alignment is within 1.0% of its indicated nominal separation except if indicated as approximate. The percentage difference between actual and nominal separation values are given within table 6. Navy transition radials signify complementary transitions as defined within the main text.**

Table 6. Data pertaining to the Family transition diagrams of figures 8a to 8i.

Family α Value (degrees)	Nominal Radial Separation	% Difference From Actual Separation
$\Delta\phi_c = 5^o$ Family, figure 8a		
0.26534	4α	-0.13
	$7\frac{3}{4}\alpha$	+0.37
	$\frac{1}{4}\alpha$	-0.51
	7α	-0.67
	$3\frac{1}{2}\alpha$	+1.0
	$\approx 3\alpha$	-1.4
	$\approx 1\alpha$	+5.1
$\Delta\phi_c = 10^o$ Family, figure 8b		
0.22734	$5\frac{1}{2}\alpha$	+0.05
	8α	-0.15
	10α	+0.25
	5α	-0.68
	$\approx 5\alpha$	+2.0
	$\approx 4\alpha$	+2.5
$\Delta\phi_c = 20^o$ Family, figure 8c		
0.18193	$\frac{1}{2}\alpha$	+0.038
	$6\frac{3}{4}\alpha$	+0.16
	$1\frac{3}{4}\alpha$	+0.20
	$1\frac{1}{2}\alpha$	-0.33
	6α	-0.33
	4α	-0.51
	$4\frac{1}{2}\alpha$	+0.77
	2α	-0.79
	$\approx 2\alpha$	+1.7
	$\approx 1\alpha^a$	-2.2
	$\approx 1\alpha^b$	-2.7
$\Delta\phi_c = 30^o$ Family, figure 8d		
0.17685	$12\frac{2}{3}\alpha$	+0.040
	$15\frac{1}{2}\alpha$	-0.043
	$14\frac{2}{3}\alpha$	-0.069
	2α	+0.085
	12α	-0.10
	9α	+0.15
	$1\frac{3}{4}\alpha$	+0.17
	$13\frac{1}{2}\alpha$	+0.23
	$15\frac{2}{3}\alpha$	-0.31
	$5\frac{1}{2}\alpha$	-0.38
	8α	+0.65
	$\frac{1}{2}\alpha$	+0.65
	$3\frac{1}{2}\alpha$	+0.81
	4α	+0.93
	$\approx \frac{1}{4}\alpha^a$	+1.8
	$\approx \frac{1}{4}\alpha^b$	+1.8
	$\approx 3\alpha$	-1.8
	$\approx 1\alpha$	-3.9
	$\approx 2\alpha$	+4.6
$\Delta\phi_c = 50^o$ Family, figure 8e		
0.28509	19α	+0.024
	5α	-0.17
	$23\frac{2}{3}\alpha$	-0.17
	9α	-0.19
	$9\frac{1}{2}\alpha$	-0.20
	$13\frac{1}{2}\alpha$	-0.20
	31α	-0.20
	$4\alpha^a$	-0.21
	8α	-0.21
	$4\alpha^b$	+0.23
	12α	-0.56
	$6\frac{2}{3}\alpha^a$	+0.60
	$6\frac{2}{3}\alpha^b$	+0.65
	20α	+0.97
	$\approx 2\frac{2}{3}\alpha$	+1.2
	$\approx 12\alpha$	+1.5
	$\approx \frac{1}{2}\alpha$	+3.1
$\Delta\phi_c = 90^o$ Family, figure 8f		
0.98495	$2\frac{3}{4}\alpha$	-0.023
	$7\frac{1}{2}\alpha$	+0.025
	$12\frac{1}{2}\alpha^a$	-0.080
	$14\frac{1}{2}\alpha$	-0.082
	$24\frac{1}{2}\alpha$	-0.10
	$13\frac{1}{2}\alpha^a$	-0.11
	$8\frac{1}{2}\alpha$	+0.12
	$9\frac{1}{2}\alpha$	+0.13
	$30\frac{1}{2}\alpha$	-0.13
	$16\frac{1}{2}\alpha$	-0.17
	20α	+0.19
	$22\frac{1}{2}\alpha$	+0.27
	$11\frac{3}{4}\alpha$	+0.29
	$12\frac{1}{2}\alpha^b$	+0.29
	$13\frac{1}{2}\alpha^b$	+0.30
	13α	-0.57
	$15\frac{1}{2}\alpha$	-0.68
	10α	+0.72
	9α	+0.90
	8α	+0.93
	6α	-0.99
$\Delta\phi_c = 135^o$ Family, figure 8g		
2.5329	$9\frac{2}{3}\alpha$	+0.12
	3α	-0.26
	7α	-0.39
	4α	-0.48
	$5\frac{1}{3}\alpha$	+0.63
	$\approx 2\frac{2}{3}\alpha$	+1.4
$\Delta\phi_c = 180^o$ Family, figure 8h		
4.9134	$5\frac{2}{3}\alpha$	-0.15
	$12\frac{1}{2}\alpha$	+0.43
	$11\alpha^a$	-0.53
	$11\alpha^b$	+0.60
	$10\frac{2}{3}\alpha$	-0.62
	$1\frac{1}{2}\alpha^a$	+0.73
	$1\frac{1}{2}\alpha^b$	-0.76
	$\approx 4\alpha$	+1.1
	$\approx 7\alpha$	-1.5
	$\approx 2\alpha$	-2.3
$\Delta\phi_c = 220^o$ Family, figure 8i		
7.7336	$4\frac{1}{2}\alpha$	+0.10
	$3\frac{1}{3}\alpha$	+0.43
	$1\frac{1}{2}\alpha$	-0.68
	$2\frac{2}{3}\alpha$	-0.75
$\Delta\phi_c = 270^o$ Family, Fig. 8(i)		
11.981	$4\frac{1}{2}\alpha$	-0.11
	$\frac{3}{4}\alpha$	-0.43
	2α	+0.62
	$3\frac{1}{2}\alpha$	+0.63
	3α	-0.87
	$\approx 1\frac{1}{4}\alpha$	+1.2

Table 7. Ratios of $\overline{\alpha}_{\Delta\phi}$ values and their alignment with common fractions, categorised within three Tiers based on common fraction type (simple or complex) and Family type (primary or secondary). Tier 1 involves simple common fractions and primary Family members only. Here, a simple fraction is defined as being constructible solely from natural numbers less than 10.

Tier 1 Ratio Alignment#			
Family α Ratio	Nominal Ratio Value	% Difference Magnitude From Actual (Median) Ratio Value	Actual Ratio Value ± 95% CI
$\overline{\alpha}_{5^0} : \overline{\alpha}_{30^0}$	3:2	0.024	0.6665 ± 0.0023
$\overline{\alpha}_{10^0} : \overline{\alpha}_{20^0}$	5:4	0.032	0.8003 ± 0.0024
$\overline{\alpha}_{10^0} : \overline{\alpha}_{50^0}$	4:5	0.32	1.2540 ± 0.0035
$\overline{\alpha}_{90^0} : \overline{\alpha}_{180^0}$	1:5	0.23	4.988 ± 0.0119
$\overline{\alpha}_{10^0} : \overline{\alpha}_{30^0}$	9:7	0.018	0.7779 ± 0.0021
Tier 2 Ratio Alignment			
$\overline{\alpha}_{20^0} : \overline{\alpha}_{180^0}$	1:27	0.026	27.01 ± 0.07
$\overline{\alpha}_{50^0} : \overline{\alpha}_{270^0}$	1:42	0.060	42.03 ± 0.14
$\overline{\alpha}_{5^0} : \overline{\alpha}_{270^0}$	1:45	0.34	45.15 ± 0.22
$\overline{\alpha}_{5^0} : \overline{\alpha}_{180^0}$	1:18½	0.093	18.52 ± 0.08
$\overline{\alpha}_{20^0} : \overline{\alpha}_{30^0}$	18½:18 or 18:17½	0.092 or 0.015	0.9721 ± 0.0013
$\overline{\alpha}_{5^0} : \overline{\alpha}_{10^0}$	21:18	0.042	0.8568 ± 0.0038
$\overline{\alpha}_{30^0} : \overline{\alpha}_{50^0}$	18:29	0.058	1.612 ± 0.001
$\overline{\alpha}_{5^0} : \overline{\alpha}_{50^0}$	27:29 or 21:22½	0.033 or 0.017	1.074 ± 0.004
$\overline{\alpha}_{20^0} : \overline{\alpha}_{50^0}$	18½:29 or 16:25	0.034 or 0.29*	1.567 ± 0.002
Tier 3 Ratio Alignment			
$\overline{\alpha}_{5^0} : \overline{\alpha}_{135^0}$	2:18	0.48	9.546 ± 0.039
$\overline{\alpha}_{20^0} : \overline{\alpha}_{135^0}$	1:14	0.55	13.92 ± 0.03
$\overline{\alpha}_{10^0} : \overline{\alpha}_{220^0}$	1:34	0.052	34.02 ± 0.16
$\overline{\alpha}_{220^0} : \overline{\alpha}_{270^0}$	20:31	0.051	1.549 ± 0.008

#For consistency of representation with some Tier 2 and 3 ratios, the Tier 1 ratios 3:2 and 9:7 may be expressed as 27:18 and 18:14 respectively.
*Based on the established Tier 1 ratios 4:5 and 5:4.

For the Tier 1 $\overline{\alpha}_{\Delta\phi}$ ratios of table 7, the percentage differences between actual and nominal ratio values, for CIs ranging from 80 to 95%, are graphically indicated by figure B1 (Appendix B). Figure B1 demonstrates that for all Tier 1 ratio calculations, percentage differences remain within 0.5% when 95% CI error margins (and not just exact median $\overline{\alpha}_{\Delta\phi}$ values) are included.

Figure 9 plots the $\overline{\alpha}_{\Delta\phi}$ versus $\Delta\phi_c$ values of table 5, with vertical error bars at 95% CI just resolvable (and therefore included) for the two right-most points only. The parabolic curve of best fit for figure 9 (r = 0.99998, $p < 0.001$), for which error margins are stated at 95% CI, is given by (2):

$$\begin{aligned}\overline{\alpha}_{\Delta\phi} &= (1.9772 \pm 0.0049) \times 10^{-4} \Delta\phi_c^2 \\ &- (9.990 \pm 0.097) \times 10^{-3} \Delta\phi_c + (3.002 \pm 0.021) \times 10^{-1},\end{aligned} \tag{2}$$

with a subsequent rate of change of:

$$\begin{aligned}\frac{d\overline{\alpha}_{\Delta\phi}}{d\Delta\phi_c} &= (3.954 \pm 0.010) \times 10^{-4} \Delta\phi_c \\ &- (9.990 \pm 0.097) \times 10^{-3}.\end{aligned} \tag{3}$$

Note that the uncertainty analysis applied to the coefficients of the above inter-Family parabolic modelling includes the propagation of $\overline{\alpha}_{\Delta\phi}$ 95% CI error margins, but not standard error based on the variance of the model's *y*-

residuals. The rationale for this approach is found within the Evidence of a Quantum Nature Subsection 5.5. In any event, the standard errors of the coefficients from left to right (second- to zeroth-order function terms) based on *y*-variance analysis are small due to the model's strong correlation (standard errors being $\pm 1.5 \times 10^{-6}$ degrees^{-1}, $\pm 4.0 \times 10^{-4}$ and $\pm 1.8 \times 10^{-2}$ degrees respectively).

The *x*-turning point of the figure 9 parabola minimum is $\Delta\phi_{\min} = 25.33 \pm 0.25^{\circ}$ and the corresponding *y*-turning point is $\alpha_{\min} \approx 0.1740^{\circ}$. Here, $\alpha_{\min}$ is indicated as approximate based on an outcome-driven postulate that can now be formulated. Viz., just like many intra-Family radial separations are multiples of $k\alpha_{\Delta\phi}$ as per figure 8 and table 6, it may be assumed that $\alpha_{\min}$ has significance and that some so-far-unaccounted-for separations are multiples of $k\alpha_{\min}$, in which case $\alpha_{\min}$ can be determined with high accuracy using the previously applied iterative linearization process.

For this process applied about the region of approximated $\alpha_{\min}$ and with the separation acceptance/rejection threshold set finer via its reduction from 1.0% (used for $\alpha_{\Delta\phi}$ determination) to 0.33%, analysis gives $\alpha_{\min} = 0.174019 \pm 0.000054^{\circ}$ with an $\overline{\alpha}_{\Delta\phi}$ EM of $\pm 0.000010^{\circ}$ (95% CI and correlation statistics of $r > 0.99999$, $p < 0.001$), based on a total of 28 $k\alpha_{\min}$ matches across five Families (especially within the 20°, 30° and 50° Families). The average percentage difference (magnitude) between actual and nominal ($k\alpha_{\min}$) separation values for the 28 matches is less than 0.2%. See figure C1 (Appendix C) for transition diagram (with linearization graph of $\alpha_{\min}$ determination as inset). Due to the wide-scoping manner in which $\alpha_{\min}$ spans across Families, it will from this point be referred to as a *universal* quantum increment value.

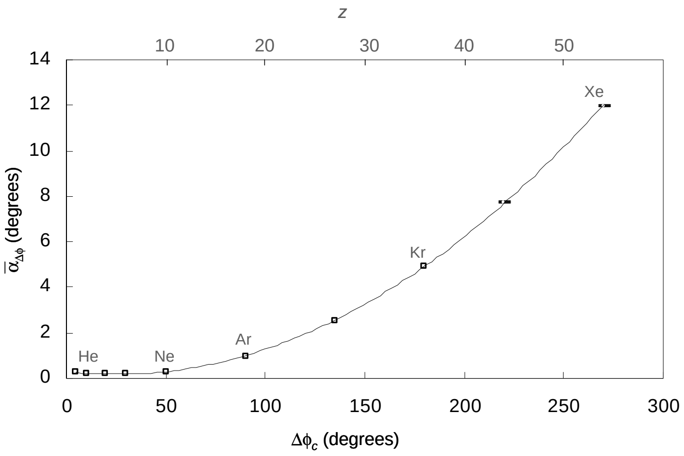

FIGURE 9. Family $\overline{\alpha}_{\Delta\phi}$ versus $\Delta\phi_c$ based on the values of table 5. The secondary *x*-axis applies the linear transformation $\Delta\phi_c/5 \rightarrow z$, with subsequent annotations identifying *z* values for (five of eight) primary Family members that coincide with the atomic numbers of indicated noble (rare) gases. Error bars (95% CI) are resolvable (just) for the two right-most points only.

Finally, the remaining tentative result below is not intended for in-depth analysis but as a brief point of interest and potential relevance within later quantum mechanical discussions:

Linear mapping to a proposed dimensionless index, *z*, via the transformation $\Delta\phi_c/5 \rightarrow z$ (as per the secondary *x*-axis of figure 9), respectively yields for the eight ascending primary Family members $z = 1, 2^*, 4, 6, 10^*, 18^*, 36^*$ and 54^*. The *z* values with asterisk equal the number of electrons for the most stable electronic configurations of atomic structure theory such that all subshells below any given *s*-subshell are fully occupied. That is, these asterisked *z* values equate to the atomic numbers of the noble (rare) gas elements of He ($1s^2$), Ne ($2p^6$), Ar ($3p^6$), Kr ($4p^6$), and Xe ($5p^6$), as annotated within figure 9, where the bracketed notation gives the filling of the outer-most subshell. Following the same atomic labelling, the remaining primary Family $z = 1, 4, 6$ values equate to the elements of H ($1s^1$), Be ($2s^2$), and C ($2p^2$), whilst the turning point equates to $z = 5.07 \pm 0.05$ or ≈B ($2p^1$).

5. DISCUSSION

5.1 ELIMINATION OF ARTEFACT AS A CAUSAL EFFECT

Given the known chaotic-like nature of harmonic phase for conventional EEG frequency analysis (first-order analysis), and chaotic elements and limitations of existing phase-based analysis techniques such as second-order bispectral analysis discussed within Subsection 1.2, the identification of any strong, or even somewhat regular, phase relationship or behaviour within a new manner of EEG analysis prompts inherent interest and calls for closer inspection. However, mathematically, spectral oscillations in response to some sharp peak are expected, and so caution must be followed when assigning any biophysical significance to *FT′* profiles that exhibit oscillations (e.g., figures 4b and 6b) originating from a conventional FFT peak of high alpha (or other such) activity. Hence, consideration must first be given to the possibility of *FT′* spectral characteristics being some not surprising mathematical result or artifact, despite various layers of statistical analysis demonstrating that $\Delta\phi$ behaviours within presented *FT′* spectra defy normal distribution expectations. These possibilities are eliminated as follows:

Firstly, as per Subsection 1.3, the calcium signalling study [55] demonstrates that Ca^{2+} ions regulate a wide spectrum of cellular processes, and that Ca^{2+} concentration oscillatory patterns display large spatial and temporal diversity originating from an intricate concert action between several Ca^{2+} transporters to provide important cellular communication encoding. Also, various forms of coupling, including oscillatory forms, across frequencies of the EEG have been identified as per Subsections 1.2 and 1.3. Hence, suggestions that the oscillatory nature of presented FT' spectra, and the oscillatory FFT deconstruction of figure 3, have some biophysical connectedness to impulse encoding is reasonable through analogous consistency, especially given the ion transport origin of the EEG in the case of the Ca^{2+} analogy.

Secondly, while the decaying behaviour of FT' amplitude profiles are reminiscent of a FFT spectral leakage response to windowing [64], such spectral leakage is typically smaller in scale (–60 to –80 dB compared to –10 to –20 dB for the present study). Also, the main FT' amplitude profile characteristics display relative invariance to window testing and are not apparent for random waveform (e.g., white noise) analysis, with the long duration of analysed EEG segments (up to 200 s) also lessening the significance of windowing. Hence, windowing effect mitigation, together with the consistency of several FT' features for different subjects, EEG states and FFT defining parameters (such as $\Delta f = 0.125$ versus 0.005 Hz and $T = 8$ versus 200 s), further suggest a biophysical basis of FT' characteristics.

Thirdly, aliasing artifact due to a Nyquist-related effect of FFT sampling may be eliminated since FT' amplitude profiles have mostly decayed once an effective time of $t' \approx 1.0$ s is reached. Therefore, the Nyquist sampling theorem of $f_s \geq 2f_{\max}$, which when written in a time base for FFT sampling dictates a $T \geq 2.0$ s condition for the stated effective decay time, is easily met by both data sets.

Finally, within the above-stated mathematical expectation of spectral oscillations in response to some sharp peak lies an important point of perspective. Viz., within clinical neurophysiology, when an alpha or other peak is observed it may be associated with some state of consciousness, increased neural activity and/or memory recall, perhaps with quantitative considerations such as contained relative power and the physical characteristics of a causal sinusoidal oscillation in the original time-domain. More mathematically-orientated considerations (e.g., via EEG simulation models) naturally provide additional quantified explanation of these peaks (e.g., a relatively early explanation, that still holds some relevancy, involves a cortical system modelled as a closed medium allowing the propagation of travelling waves and thus capable of standing waves and resonance [4]). However, despite the many valuable clinical and mathematical neurophysiological insights provided to date, including from quite sophisticated EEG simulation models [4,5], biophysical origin specificity for such peaks still arguably requires completion of explanation.

In contrast, within a highly mathematical field such as quantum mechanics (as a deliberate comparative example due to later discussion), for any frequency spectrum that contains a sharp resonance peak, the peak is invariably traced to a specific and well mathematically understood physical origin. Thus, rather than taking a perspective that an alpha or other conventional FFT peak will naturally bring about spectral oscillation within the FT', a reverse perspective of asking *what underlying functional, biophysical behaviour within the* FT' *is giving rise to the FFT peak?*, is worthy of exploration. Certainly, the apparent deliberate ϕ structuring and functionality over the effective 1 s timescale of FT' amplitude profiles implies biophysical meaningfulness, especially since the 1 s timescale (which may still reflect real-time behaviour) is consistent with the period of average human heart rate and so may broadly reflect expected body homeostasis [33].

5.2 INCREASING LINEARITY OF ϕ AS A FUNCTION OF SLEEP DEPTH

For awake and non-deep sleep states, upward $\Delta\phi$ values of any given FT' spectrum are spread by varying amounts from 0 to 2π radians (most spread for awake), with such spectra also displaying oscillatory ϕ behaviour in the presence of alpha and other spectral peaks within the conventional FFT (recall that a target comparison state of the present study is occipital EEG with eyes-closed, due to the state's known association with strong PDR alpha activity and alpha linkage to neural network communication and co-ordination [4,51,61], as per Subsection 3.3.2).

Reductions in both the spread of $\Delta\phi$ values, and the oscillatory nature of ϕ, are observed for increasing relaxation and sleep depth, and associate with a progressive increase in ϕ versus t' linearity. While these increasing linearity observations are generalised and with exceptions (due to the influence on the FT' spectrum by spectral peaks within, and overall smoothness of, the conventional FFT), the high degree of linearity for stage 4 sleep is more absolute (note that despite this commentary it is actually the FT' spectrum that evidentially influences the FFT spectrum as suggested within Subsection 5.1).

The rate magnitude $|d\phi/dt'|$ similarly appears to generally increase with progression towards stage 4 sleep. For example, the FT' spectrum of figure 4d for a subject in relaxed wakefulness with eyes-closed, derived from a prefrontal EEG (and so physiologically linked to attention and short-term memory), while displaying some degree of ϕ irregularity, demonstrates approximate ϕ constancy or low $|d\phi/dt'|$. The behavioural characteristic of figure 4d is repeated to varying degrees by figures 7b and 7d for subjects in sleep preparedness. The generalised picture of increasing $|d\phi/dt'|$ with increasing sleep depth continues with figure 6b for awake/stage 1 sleep, and is completed by the more in depth stage 4 sleep (linearity) analysis based on three subjects and 17 EEG segments. For this latter analysis ($-r \geq 0.990$, $p < 0.001$ in all cases), $d\phi/dt'$ values for the three subjects are: -163 ± 9 to $-203 \pm 7^{o}{\cdot}s^{-1}$ (3.3%), -166 ± 6 to $-206 \pm 4^{o}{\cdot}s^{-1}$ (3.7%), and -190 ± 5 to $-236 \pm 8^{o}{\cdot}s^{-1}$ (2.5%), with bracketed values giving the average of all intra-figure 95% CI error margins when the margins are expressed as a percentage (see figures 6e and 6f). Stage 2 and 3 sleep FT' spectra that are not shown also complement the described overall characteristic behaviour.

The ranging $d\phi/dt'$ values for deep sleep are suggestive of dynamically changing, structured complexity within outwardly appearing constancy (perfect constancy of linearity would after all be an over-simplified expectation if some linear outcome was hindsighted). It is not uncommon for the tail of an EEG's conventional amplitude versus frequency spectrum to possess some degree of linearity depending on a subject's clinical state. Nevertheless (and despite the slight confounding effect of superimposed oscillations in some cases), the quantified linearities above are remarkable given the chaotic-like behaviour of harmonic phase for conventional first-order FFT spectra, and the limitations of established phase-based analysis techniques such as bispectral analysis. The remarkableness increases upon contemplation of physical significance, since the outcome indicates that the phases of successive harmonics of the figure 3 deconstruction are linearly related across the frequency spectrum, thus demonstrating further complexity within the outwardly simple linear form.

5.3 OSCILLATORY *FT′* BEHAVIOUR

The oscillatory nature of *FT′* amplitude and phase profiles (that clearly follow one another), especially observed in the presence of alpha and other spectral peaks of EEG activity, draws parallel with a PSK study [2] demonstrating the data communication benefits of controlled phase oscillation in the time-domain, with such control for just one conventional harmonic leading to the provision of discretely encoded data transmission rates of up to 8 $\text{Mbit}\cdot\text{s}^{-1}$ (and higher for approach variants). The manner of ϕ oscillation across the t' domain within the present study is comparatively complex and demonstrates several degrees-of-freedom that seemingly include deliberately structured upward, downward and horizontal $\Delta\phi$ (upward remaining the primary focus), as well as oscillation frequency variability with the oscillation frequencies of a selection of *FT′* amplitude profiles being 9.7 ± 1.8 Hz. Recalling that fluctuations in the original time-domain manifest within the *FT′* spectrum, albeit in potentially complex ways, these reported oscillation frequencies are consistent with those of alpha and spindle peaks and so give further credence to the Subsection 5.1 position that *FT′* characteristics are physically meaningful. Following the parallel comparison with [2], here such high degrees-of-freedom within the manner of ϕ oscillation control would lead to discretely encoded data transmission rates of immense potential consistent with that expected of an extraordinarily sophisticated communications platform like the CNS.

Thus, the showcased ϕ oscillations, by their evidential deliberate nature and ion transport origin are indeed broadly consistent with the previously raised calcium signaling whereby Ca^{2+} concentration oscillatory patterns provide important cellular communication encoding [55]. Together with the physical interpretation provided by figure 3, the structure of these ϕ oscillations further elucidate the physical and mathematical nature of high-order, across-frequency EEG relationships that manifest as subtle periodic contours of high second-order phase coupling across bicoherence spectra as outlined within Subsections 1.2 and 1.3. This elucidation includes revelation of why a conventional EEG frequency spectrum typically appears so variable, for both intra- and inter-subject comparisons of the same neural state, since what was considered chaotic-like amplitude variability for any given harmonic of the conventional frequency spectrum, is now revealed as a harmonic amplitude constructed from multi-ordered states of oscillation (or harmonics across the frequency spectrum) as per figure 3.

5.4 PHASE WHEEL SECTOR RATIOS AND RADIAL DISTRIBUTIONS

The $\Delta\phi$ values that become the phase wheel radials belong to Families named for the polar angles about which the radials cluster. Primary Families are identified at $\Delta\phi_c = 5^o$, 10^o, 20^o, 30^o, 50^o, 90^o, 180^o and 270^o, and secondary Families at $\Delta\phi_c = 135^o$ and 220^o. However, the possibility of other Family identification, especially secondary Families below 5^o or above 270^o (e.g., $\Delta\phi_c = 2.5^o$ might be predicted), should not be excluded from future studies.

In many instances within Families, the separations between radials may be written in terms of $k = j/4$ or $j/3$ ($j = 1, 2, 3 \ldots$), with a preference for $k = j/2$ ($\chi^2 = 77$, $df = 1$, $p < 0.001$ and see Evidence of a Quantum Nature Subsection 5.5 for further comment), amounts of some proposed quantum increment value, α, determined through the previously described iterative analysis procedure. Mean Family α values, $\overline{\alpha}_{\Delta\phi}$, form ratios with relatively precise common fraction alignment, with $\overline{\alpha}_{\Delta\phi}$ ratios classified as "Tier 1" within table 7 including:

$\overline{\alpha}_{5^0} : \overline{\alpha}_{30^0} = 3:2\,(0.024\%)$, $\overline{\alpha}_{10^0} : \overline{\alpha}_{20^0} = 5:4\,(0.032\%)$,

$\overline{\alpha}_{10^0} : \overline{\alpha}_{50^0} = 4:5\,(0.32\%)$, $\overline{\alpha}_{90^0} : \overline{\alpha}_{180^0} = 1:5\,(0.23\%)$, and

$\overline{\alpha}_{10^0} : \overline{\alpha}_{30^0} = 9:7\,(0.018\%)$.

Although the high precision of the above $\overline{\alpha}_{\Delta\phi}$ ratios (with bracketed alignment percentage differences based on exact median $\overline{\alpha}_{\Delta\phi}$ values) is slightly tempered by the inclusion of 95% CI error margins (see table 7 and figure B1) which extends the maximum percentage difference to 0.5%, the recurring levels of precision based on exact median values may suggest that, while $\alpha_{\Delta\phi}$ values display some variation (e.g., between subjects and clinical states), ratio alignment with common fractions often remains precise for a given EEG segment or "moment", as per individual phase wheel analysis.

The numerical symmetry of (2), which is emphasised by expressing to two significant figures, i.e., $10\overline{\alpha}_{\Delta\phi} = 2.0 \times 10^{-3}\Delta\phi_c^2 - 1.0 \times 10^{-1}\Delta\phi_c + 3.0$, is mathematically consistent with the above $\overline{\alpha}_{\Delta\phi}$ ratio findings, albeit at the reduced precision specified, though such symmetry is obviously not a necessary requirement for the formation of such ratios. The strong inter-Family $\overline{\alpha}_{\Delta\phi}$ versus $\Delta\phi_c$ parabolic functionality given by (2) raises the issue of biophysical significance which is addressed within the Evidence of a Quantum Nature Subsection 5.5. Certainly, the mathematical appropriateness of parabolic modelling is championed by the fact that the y-minimum appears representative of a universal quantum increment value, $\overline{\alpha}_{\min} = 0.174019 \pm 0.000010^{\circ}$, that has a relatively high frequency of occurrence within figure C1 such that almost every radial has connectedness to $\alpha_{\min}$ and/or some $\alpha_{\Delta\phi}$. The functionality also offers mathematical explanation of statistical outcomes demonstrating a strong departure from a normal distribution of radials (e.g., $\chi^2 = 303$, $df = 12$, $p < 0.001$ of table 3 and $P = 9.8 \times 10^{-10}$ of table 4), since the functionality yields the tendency for $\Delta\phi$ radial alignment with/about not only $\Delta\phi_c$ but also with the relatively large parent set of primary radials (now explained as arising from fractional perturbations of $\alpha_{\Delta\phi}$ about $\Delta\phi_c$ over all Families).

In addition to the formalised $\overline{\alpha}_{\Delta\phi}$ ratio findings above, for the seven analysed phase wheels, that collectively represent a cross-section of subjects and clinical states including relatively short and long analysis times over which high-order phase relationships might occur, the ratios of sector angles within individual phase wheels also demonstrate simple common fraction alignment. The sector angle ratios 1:1, 1:2, 2:3 and 3:4 have the highest propensity (for a 1% alignment tolerance), with several additional examples demonstrating alignment to within a higher precision of 0.10%: 1:1 (<0.01%), 1:2 (0.02%) twice identified, 1:1 (0.04%), 1:2 (0.04%), $1:\sqrt{2}$ (0.04%) and 2:3 (<0.10%), with bracketed values giving the percentage difference magnitude from exact alignment and here the definition of simple common fraction is liberally extended to include fractions involving an integer and $\sqrt{2}$.

The formalised $\overline{\alpha}_{\Delta\phi}$ ratio findings undoubtedly contribute to the fact that, of the phase wheel sector ratios that align to within 1.0% of a common fraction, approximately 60% involve two different primary radials and approximately 70% involve across-Family radials. That is for example, if two sectors are constructed within different Families, then the ratio of the sectors' angles can be expected to form a common fraction when the sector angles are fractional amounts of quantities ($\alpha_{\Delta\phi}$ values) that are themselves fractionally related.

The most highly represented Families within the sector ratios of interest are the 20° and 30° Families (approximately 50% representation), followed by the 10° and 50° Families (approximately 30% representation), followed by the 90° Family. These propensities not surprisingly appear influenced by Family populations (i.e., the 20° and 30° Families are the most populated) which in turn are weighted by the fact that several contributing EEG segments belong to sleep subjects, and it is clear that a trend towards lower $\Delta\phi$ (and ultimately towards a linear ϕ versus t' relationship) exists for progressively deeper sleep stages.

The noted $1:\sqrt{2}$ (0.04%) sector ratio alignment of one analysed phase wheel (not shown) is accompanied by $1:\sqrt{2}$ (0.26%) and $1:\sqrt{2}$ (0.81%) sector ratio alignments from the same phase wheel. While the triple occurrence of $\sqrt{2}$ within sector ratios naturally raises interest, the occurrences must be treated as cautionary due to occurrence being within the EEG segment of one subject only. However, the finding is nonetheless flagged as an area for future verification or contradiction.

5.5 EVIDENCE OF A QUANTUM NATURE

5.5.1 QUANTISED INCREMENTS AND PARABOLIC FUNCTIONALITY

The cerebral cortex potentially represents the ultimate quantum computer. Accordingly, the manner in which $\Delta\phi$ radial separations within each Family align with $k\alpha_{\Delta\phi}$ (where k is preferably an integer or half-integer over other fractional integers, $\chi^2 = 77$, $df = 1$, $p < 0.001$) is possibly suggestive of some form of quantised neurophysiology, especially given the significance of integer and half-integer increments in many well known quantum scenarios (such as quantised principal electron orbitals and spin-based fine structure splitting). The discrete nature of the highly correlated parabolic modelling of $\overline{\alpha}_{\Delta\phi}$ versus $\Delta\phi_c$ for all Families (figure 9) also supports this possibility since parabolic functionality is observed across a spectrum of fundamental quantum scenarios – four example scenarios follow:

Quantum parabola example 1

Parabolic modelling of noble gas atomic numbers, Z, versus a generic quantum number, $x = 0, 1, 2, 3\ldots$, yields the mathematically engaging parabolic function $Z = \left(3 - \tfrac{1}{7}\right)x^2 + 2x + \left(3 + \tfrac{1}{7}\right)$, where the function's coefficients are exact (not rounded), and y-residuals from the model function demonstrate quantised and highly correlated structure [65]. Here, elucidation is also provided as to why the uncertainty analysis applied to the coefficients of the inter-Family parabolic modelling of figure 9 incorporates $\overline{\alpha}_{\Delta\phi}$ error margins but not standard error (y-variance regression) analysis. Viz., the latter analysis assumes that residuals away from the model function represent model error. However, from a quantum mechanical perspective, perturbations from such models are typically quantised and have physical significance (e.g., commonly associated with the fine structure of atomic energy levels). Hence, it is inappropriate to effectively force data points back onto the model function and an assumption that residuals have physical significance is more appropriate for the EEG quantisation postulate at hand.

Quantum parabola example 2

Bohr's famous model of atomic hydrogen, though considered classical or semiclassical in nature, is nonetheless based on a landmark quantisation of angular momentum postulate, and calculates the energies of principal electron orbit levels via a succinctly derived theoretical term involving n^{-2}, where n is a principal orbital quantum number. A theoretical extension to Bohr's model derives an additional n^{-4} term and allows the calculation of fine energy structure to accuracies comparable to that of relativistic Dirac theory [66]. Hence, while semiclassical approaches to quantum systems always possess limitations, Bohr's original model and its cited extension mathematically (if not physically) reflect parabolic functionality of hydrogen energy levels (after rudimentary variable substitution is applied to the original n^{-2} and new n^{-4} terms).

Quantum parabola example 3

A particle contained within an infinite square well potential represents one of the most fundamental quantum systems studied by students learning introductory quantum mechanics. Solutions to Schrödinger's time-independent equation for such a potential yields eigenvalues (energy solutions) that are proportional to n^2, with n again representing a principal quantum number. Hence, the energy functionality is parabolic, and parallels may certainly be drawn with the containment of ions within the confines of the nerve cell membrane and under the influence of a well-like action potential.

Quantum parabola example 4

Within the quantum formalism of some atomic interactions, the total molecular potential of a formed temporary molecule often includes a centripetal term (that relates to the centripetal motion of the atoms), V_c, such that $V_c \propto J(J + 1)$, where J is a quantum number labelling the eigenvalues associated with the total molecular angular momentum. This $V_c \propto J(J + 1)$ term can play a crucial resonance role within atomic interactions (as expanded upon and linked to conventional EEG peaks within Appendix D) and inherently displays parabolic functionality based on its second-order mathematical form.

5.5.2 SYMMETRICAL CONSIDERATIONS

Several phase wheels display radial *symmetry* and in select cases the *mid-line* between symmetrical radials is used to form sectors yielding angular ratios aligning with common fractions (e.g., the η:κ and κ:λ sector ratios of phase wheel figures 4e and 5e respectively). Additionally, symmetrical $\Delta\phi$ clustering about $\Delta\phi_c$ is evident to varying degrees within the figure 8 transition diagrams. Such symmetrical considerations are of interest since they allow further quantum parallels to be drawn or at least considered (e.g., parallels with the symmetries of spin-based spectral splitting and the existence of some atomic resonances in pairs [67]).

The inherent circular symmetry that comes with measuring the phase difference between any two sinusoidal harmonics validates the consideration of complementary radials within aspects of *FT′* analysis, and so the finding that complementary radials appear relevant for some identified Families (recall that the $\Delta\phi_c = 135^{\circ}$ Family was relegated to secondary Family status on the basis of a too heavy reliance on complementary radials) may also be indicative of such quantum mechanical parallels. Accordingly, the above-described $\Delta\phi$-based symmetries may well be a consequence of some lower, preferred (parallel) versus higher, non-preferred (anti-parallel) neural state or process, and contribute to the volume of evidence supporting a quantum aspect to presented findings.

More generally, it is pertinent to recall that within physics every symmetry identifies with a conservation law[3] and, in some common cases, it is parabolic symmetry that leads to the conservation (e.g., as classically observed for some projectile motion parameters within the confines of total mechanical energy conservation), such are the mathematical advantages and applications of the parabolic form.

5.5.3 TRANSFORMATION TO ELEMENTAL LABELLING

The transformation $\Delta\phi_c/5 \rightarrow z$ (see figure 9) yields, for primary Families in ascending order, z = 1, 2, 4, 6, 10, 18, 36 and 54. As per Subsection 4.2.3, based on an atomic number nomenclature this transformation allows the primary Families to be respectively labelled as H ($1s^1$), He ($1s^2$)*, Be ($2s^2$), C ($2p^2$), Ne ($2p^6$)*, Ar ($3p^6$)*, Kr ($4p^6$)*, and Xe ($5p^6$)*, where an asterisk signifies a stable noble gas. Note that this labelling is not suggestive of elemental involvement, but of the possible involvement of some proportionally optimal quantised state within EEG neurophysiology. For $\Delta\phi_c = 10^{\circ}$ it is interesting that $\alpha_{10^{\circ}}$ (or now $\alpha_{z\,=\,2 \text{ or He}}$) forms the most Tier 1 $\overline{\alpha}_{\Delta\phi}$ ratios within table 7, since He is the highest rated universal element in terms of combined abundance and stability.

The above declaration that elemental labelling is suggestive of some proportionally optimal quantised state (or, to re-express, representative of another example of quantum mechanical forms reoccurring across many scales of the physical world as per the approximate repetition of quantised energy level structural form from the level of quarks upwards) and not actual elemental involvement, cannot be overemphasised. Available evidence does not allow further conclusion to be drawn. However, when Dmitri Mendeleev first constructed the periodic table, electrons and orbital concepts were unknown, with elements grouped by their masses and properties. Vacancies within the original periodic table were, in the

---

[3] The symmetry-conservation law association is that of mathematics' historical matriarch, Emmy Noether, as acknowledged by [68].

fullness of time, filled by other scientists leading to discoveries of new elements, with the evolving table eventually paving the way for the understanding of: proton, neutron and electron arrangements; chemical reactivity; and ultimately quantum mechanics [68]. Hence, the preliminary elemental labelling finding of the present study similarly encourages developmental findings that may in time lead to cerebral cortex process understandings that perhaps have not yet been envisaged. Several other elemental labelling outcomes of curious interest exist, including elements of biological abundance and significance, but are not specified here in line with the present study's scope.

5.5.4 QUANTUM MECHANICAL OVERVIEW

In summary, wide-ranging quantum mechanical underpinnings of the EEG are, perhaps unsurprisingly, indicated by: radial symmetry; the quantised structure of intra-Family radial separations; parabolic inter-Family functionality; high degrees-of-freedom displayed by structured $\Delta\phi$ within the FT'; the preliminary finding of elemental labelling (or proportionalities between $\Delta\phi_c$ and Z values of stable elements); and shared characteristics between common quantum resonance types within atomic interactions and peaks within the conventional EEG frequency spectrum (addressed within Appendix D). Such quantum complexities within the cerebral cortex could fittingly, for such a profoundly sophisticated and computationally powerful entity, be described as *biological quantum entanglement* which only a quantum treatment of the EEG can fully interpret into the future.

5.6 OTHER FUTURE CLINICAL RESEARCH DIRECTIONS AND IMPLICATIONS

5.6.1 DECIPHERING OF FT′ ENCODING

While the present study reveals considerable mathematical detail in regards to the manner of FT' encoding based on upward $\Delta\phi$ analysis, scope clearly remains for FT' deciphering in a clinical context, including with additional downward and/or horizontal $\Delta\phi$ analysis. Such deciphering studies, e.g., that quantitatively investigate the manner of deliberate $\Delta\phi$ management and coordination for specific CNS function and stimuli (perhaps even emotional), have the potential to significantly contribute to BCI and neuroprosthetic interfacing advancements.

The similarity of the two (prefrontal and central) linear but slightly oscillatory ϕ versus t' profiles of figure 6g, reflecting origin source overlap, is not surprising and consistent with coherence and range-based correlation findings of conventional EEG frequency analysis [24], as well as with the Subsection 4.1.1 finding of a generally similar outcome for FT' amplitude profile shape when comparing the averages of EEG channels 1 to 12 against channels 13 to 19. However, such profile comparisons may also offer opportunity for more specific origin and functional connectivity information identification due to the profiles containing the phases of many FT' harmonics. That is, the two profiles under comparison in figure 6g are mostly identical except for subtle ϕ variances (that may still maintain the same $\Delta\phi$ in some instances as demonstrated by figure 6g), and so harmonic propagation time or amplitude comparisons (e.g., degree of delay, attenuation, etc.) on a *harmonic-by-harmonic basis for many profiles* may provide opportunity for mathematical reconstruction (e.g., via a forward model) that reveals highly specific spatiotemporal origin distribution and functional connectivity information.

5.6.2 INCREASING LINEARITY WITH INCREASING SLEEP DEPTH FOR THE FT′

A full clinical study that investigates linearity and $d\phi/dt'$ of ϕ versus t' as potential indices of sleep stage naturally derives from the present study. Likewise, the sensitivities of these potential indices towards depth of anaesthesia, awake vigilance, and consciousness in general, are also indicated as topics of future clinical research. An additional aspect of such future research could further quantify the sleep transition characteristics of FT' amplitude profile form, with the present study indicating dynamically changing amplitude profiles that include the display of $e^{-t'^{x}/\tau}$ behaviour.

5.6.3 THE SENSITIVITY OF FT′ TOWARDS NEUROPATHOLOGY

The two FT' spectra for an elderly probable Alzheimer's subject (figures 5b and 5d) produced several examples of the types of common fraction ratios and structured $\Delta\phi$ radial separations of interest within the present study. However, notable is the contrasting comparison between figures 4d and 5d (healthy adult versus probable Alzheimer's respectively for prefrontal EEG with eyes-closed). The healthy adult spectrum displays $d\phi/dt'$ approaching (approximate) early constancy and the mostly featureless spectrum is consistent with the intuitive expectations of a relatively neutral neural state. The probable Alzheimer's spectrum contrastingly displays, for similarly desired neural neutrality, a full (almost "frantic") spectrum of $\Delta\phi$ that is comparable to the subject's simultaneous occipital spectrum (figure 5b). Also, the oscillatory behaviour of the FT' amplitude profile for the healthy adult in figure 4b is not apparent within the probable Alzheimer's counterpart figure 5b. Despite marked alpha activity differences which are clearly influential, these comparisons could indicate a sensitivity of the FT' spectrum towards various neurological disorders. Hence, a large-scale study of healthy versus neuropathological FT' would constitute a meaningful future research direction and potentially contribute to the ongoing understanding of such disorders.

5.6.4 THERAPEUTIC INTERVENTIONS (INCLUDING MUSIC THERAPY) TO FACILITATE HEALTHY $\Delta\phi$ MODULATION OF THE FT′

Subsection 5.3 rationalised the oscillatory nature of *FT′* spectra as being deliberate. However, the added evidential dimension of *FT′* oscillatory behaviour being *ratio-based* may also rationalise a connectedness to music-based neurophysiological research, which for example has found: (i) a strong association between rhythm (perception skills) and language development in young children that is linked to the sharing of neural networks/cognitive resources between rhythm and grammatical structure learning [69]; (ii) that listening to classical music (by musically experienced participants) enhances the activity of genes responsible for brain function (in particular genes involved with dopamine secretion and transport, synaptic neurotransmission, learning and memory), with the synuclein-alpha gene (a known risk gene for Parkinson’s disease) being one of the most enhanced [9]; (iii) benefits of music therapy for the treatment of dementia-based behavioural disorders [70]; and more generally (iv) multiple effects, both structural and functional, on the cerebral cortex in response to deliberate music exposure [6,7,9] (these examples represent only a small subset of a profusion of music-based neurophysiological research).

The identification of common fraction-aligned $\overline{\alpha}_{\Delta\phi}$ ratios, as well as common fraction-aligned sector angle ratios for sectors formed by $\Delta\phi$ radials within individual phase wheels, potentially contributes to the understanding of the biophysical determinants that underlie music therapy/exposure (these determinants remain largely unknown despite the above-noted research profusion [9]). Viz., Tier 1 $\overline{\alpha}_{\Delta\phi}$ ratios align, with high precision, to 3:2, 5:4, 4:5, 1:5 and 9:7, and sector ratios with the highest propensity within individual phase wheels align, with high precision, to 1:1, 1:2, 2:3 and 3:4, and all of these ratios combined (except 9:7) are prominent within (the frequency interval proportions of) pentatonic music scales[4] that are accepted as being the most historically significant scales on the basis of their independent development by many ancient cultures [71,72]. Several other examples of connectedness between key ratios of the present study and those that are fundamental to music theory and formalisms (e.g., in the area of timing and rhythm) also exist but are not specified here in line with the present study’s scope.

Hence, future research that involves the delivery of therapeutic alleviatory interventions via music, TMS, or other means, and designed to stimulate or enhance healthy neurological function (e.g., by resonant absorption of an applied therapeutic medium containing appropriate ratio-based modulations or modulations of a time-domain waveform constructed on the basis of other ideal *FT′* characteristics), and which involves pre- and post-therapy comparisons with healthy EEG, therefore appears warranted. Furthermore, the small 95% CI error margins of $\overline{\alpha}_{\min}$ and $\overline{\alpha}_{\Delta\phi}$ values (equating to percentage errors ranging from 0.006 to 0.39% with an average of 0.19%), appear to indicate that the values of α-related quantities will be tightly confined across a wider population, and thus any future therapies that are found to be beneficial by specifically targeting these or associated quantities may to some extent not require individual prescriptions in terms of applied modulation settings.

5.6.5 IMPLICATION OF POSSIBLE ZOOLOGICAL UNIFORMITY

An interesting zoological offshoot finding is that Tier 1 $\overline{\alpha}_{\Delta\phi}$ ratios coincide with dominant ratios (3:2, 5:1) of the most used sperm whale communication (click-based) codas [73]. This offshoot finding is raised because, for many, sperm whales represent the largest cooperative group of vertebrates outside of humans, and have a multilevel social system with an advanced, culturally transmitted communication system [73–75]. A ratio-based finding can also be extrapolated from communication research for Beluga whales [76], known for being highly vociferous and generating a variety of calls using tonal and pulsed components with an added ability to copy human speech (in a limited manner). Ratios of average inter-pulse intervals (interval at pulse train end:interval at pulse train beginning) within the dominant broadband pulse sound (PS1 call) of isolated whales display the “quintuple” ratios 5:4, 7:5 and 6:5. Note however that, unlike the initial sperm whale example, this extrapolated result is preliminary.

Hence, a finding that communication encoding methods for the Earth’s most intelligent species share the same dominant ratios encourages contemplations on several levels and, as per the ratios-in-music coincidence findings, arguably adds support to the neurological significance (and thus mathematical mechanism and clinical efficacies) of the present study’s technique, in turn providing additional motivation for the future clinical research directions advocated within Subsection 5.6.

6. CONCLUSION

Based on the introduced high-order phase analysis technique, it is concluded that the EEG is encoded by quantised phase transitions between newly-identified harmonics across the conventional frequency spectrum, allowing for powerful phase-shift keying impulse encoding complexity with high transitional degrees-of-freedom. The technique commences with the double application of high resolution Fourier analysis applied to the EEG, leading

---

[4] Pentatonic music scales divide the octave into fifths (i.e., five notes per octave). These scales naturally involve the ratio 2:1, since it is fundamental to the octave concept, as well as the ratio 5:1 given the scales’ divisional methodology. Additionally within pentatonic scales, the ratio 3:2 is referred to as the "pure perfect fifth" and the Pythagorean pentatonic scale (which overlaps with other pentatonic scales) is constructed solely from these 3:2 and 2:1 ratios, giving the following fundamentally important tunings: 5:4 major third; 4:3 perfect fourth; 3:2 perfect fifth; 2:1 perfect octave or duplex; and 1:1, 5:1 (inherently included for reasons stated).

to *FT′* spectra (that include profiles of new harmonic phase, ϕ, over an effective time-domain, t'). The ϕ versus t' behaviour of such profiles generally becomes increasingly linear with the progression of neural state towards deep sleep. Three separate stage 4 sleep analyses (i.e., on three subjects) involving 17 EEG segments display high linear correlations ($-r \geq 0.990$, $p < 0.001$ in all 17 cases) with regression rates, $d\phi/dt'$, ranging from -163 to $-236^{o} \cdot s^{-1}$ and on average displaying error margins of $\pm 3\%$ (95% CI). Such linearities are in stark contrast to the chaotic-like nature of harmonic phase for conventional EEG frequency analysis (first-order analysis), and chaotic elements of established phase-based analysis techniques such as second-order bispectral analysis.

For awake and stages 1 to 3 sleep, *FT′* spectra display many structured ϕ transitions, including oscillatory behaviour in response to peaks (e.g., alpha, sigma sleep spindle) within the conventional frequency spectrum. For transitions whereby ϕ increases by $\Delta\phi$ between local minima and maxima, the combined $\Delta\phi$ values from seven *FT′* spectra (that include pathology, electrode placement and analysis time diversity), are found to cluster rather than follow a normal distribution (e.g., $\chi^2 = 303$, $df = 12$, $p < 0.001$). Influential $\Delta\phi$ clustering is categorised into ten "Families", with primary Families displaying clustering about $\Delta\phi_c = 5^o$, 10^o, 20^o, 30^o, 50^o, 90^o, 180^o 270^o and secondary Families displaying clustering about $\Delta\phi_c = 135^o$ and 220^o.

In many instances within Families, the separations between $\Delta\phi$ values are highly structured and may be written in terms of $k = j/4$ or $j/3$ ($j = 1, 2, 3 \ldots$), with a preference for $k = j/2$ ($\chi^2 = 77$, $df = 1$, $p < 0.001$), amounts of some proposed quantum increment value, α, such that separation is given by $k\alpha$. The α value for each Family, $\alpha_{\Delta\phi}$, is extracted as the gradient of $\Delta\phi$ separation versus k multiplier in an iterative (separation acceptance/rejection) manner that applies $r > 0.9999$, $p < 0.001$ thresholds for Family identification. The 95% CI mean values, $\overline{\alpha}_{\Delta\phi}$, for the primary Families are:

$\overline{\alpha}_{5^0} = 0.26534 \pm 0.00092^o$, $\overline{\alpha}_{10^0} = 0.22734 \pm 0.00062^o$, $\overline{\alpha}_{20^0} = 0.18193 \pm 0.00023^o$, $\overline{\alpha}_{30^0} = 0.17685 \pm 0.00007^o$, $\overline{\alpha}_{50^0} = 0.28509 \pm 0.00019^o$, $\overline{\alpha}_{90^0} = 0.98495 \pm 0.00033^o$, $\overline{\alpha}_{180^0} = 4.9134 \pm 0.0116^o$ and $\overline{\alpha}_{270^0} = 11.981 \pm 0.040^o$, with values for the secondary Families being $\overline{\alpha}_{135^0} = 2.5329 \pm 0.0055^o$ and $\overline{\alpha}_{220^0} = 7.7336 \pm 0.0302^o$.

Family $\overline{\alpha}_{\Delta\phi}$ versus $\Delta\phi_c$ values display strong parabolic functionality ($r = 0.99998$, $p < 0.001$) given by $\overline{\alpha}_{\Delta\phi} = (1.9772 \pm 0.0049) \times 10^{-4} \Delta\phi_c^2 - (9.990 \pm 0.097) \times 10^{-3} \Delta\phi_c + (3.002 \pm 0.021) \times 10^{-1}$ (95% CI), with a universal quantum increment value, $\alpha_{\min}$, spanning across Families and equating to the turning point (minimum) of the parabolic function, given by $\overline{\alpha}_{\min} = 0.174019 \pm 0.000010^o$. $\overline{\alpha}_{\Delta\phi}$ values form ratios with relatively precise common fraction alignment and these ratios, when classified as "Tier 1" (involving primary Families and simple common fractions), include: $\overline{\alpha}_{5^0} : \overline{\alpha}_{30^0} = 3:2\,(0.024\%)$, $\overline{\alpha}_{10^0} : \overline{\alpha}_{20^0} = 5:4\,(0.032\%)$, $\overline{\alpha}_{10^0} : \overline{\alpha}_{50^0} = 4:5\,(0.32\%)$, $\overline{\alpha}_{90^0} : \overline{\alpha}_{180^0} = 1:5\,(0.23\%)$, and $\overline{\alpha}_{10^0} : \overline{\alpha}_{30^0} = 9:7\,(0.018\%)$, with bracketed values giving the percentage difference between the actual formed ratio and its nominal common fraction representation. Although a case exists for basing these ratios on exact (median) $\overline{\alpha}_{\Delta\phi}$ values, all percentage differences nevertheless remain within 0.5% when 95% CI error margins are included. Several Tier 2 and 3 ratios, with classifications explained within, are also identified.

For individual subjects, $\Delta\phi$ values for any given *FT′* spectrum often display symmetries and form sectors within polar diagrams (phase wheels), with the ratios of sector angles often aligning with high precision to common (and other) fractions. Identified sector ratios from seven phase wheels of diversity and to within 0.1% alignment include: 1:1 (<0.01%), 1:1 (0.04%), $2 \times 1{:}2$ (0.02%), 1:2 (0.04%), 2:3 (<0.10%), and $1:\sqrt{2}$ (0.04%). When the alignment threshold is raised to 1.0 %, the sector ratios with the highest propensity include 1:1, 1:2, 2:3 and 3:4.

Given the overlapping common ratio-based nature of music (e.g., fundamental ratios of the culturally and historically important pentatonic scale contain the sector ratios of propensity and all but one Tier 1 ratio) and the profusion of research into the neural effects of music exposure, a possible linkage of the present study's findings to the biophysical determinants of such effects is indicated.

The symmetrical, quantised structure of dependent Family $\alpha_{\Delta\phi}$ and $\Delta\phi_c$ values, the consistency of this structure's parabolic functionality with functionalities of well known quantised systems, and the linkage of conventional EEG frequency peaks to quantum mechanical resonances, together suggest a quantum mechanical governance to neural impulse generation. An additional preliminary but nonetheless intriguing offshoot quantisation finding includes the linear transformation of primary Family $\Delta\phi_c$ values, via simple proportionate mapping, to the atomic numbers of periodic table elements of note, resulting in respective primary Family elemental labelling of H, He*, Be, C, Ne*, Ar*, Kr* and Xe* (where the asterisk signifies a noble gas), and suggestive of neuro-quantum processes involving proportionally optimal quantum states. A need for a fully quantum treatment of the EEG is subsequently indicated.

The fine impulse encoding details (ϕ-based unisons) extracted with confidence from a seemingly modest EEG set supports the present study's position that vast amounts of accessible information currently goes unrecognised by standard EEG analysis and consequently several clinical studies based on the introduced analysis technique are proposed for the future. These unisons will also provide insights for future BCI and neuroprosthetics research.

APPENDIX A – VALUES OF SELECT $\Delta\phi$ AND EXAMPLE PHASE WHEEL SECTOR ANGLES

Table A1 gives horizontal and vertical (upward) $\Delta\phi$ (rounded to one decimal place) pertaining to the annotations of figures 4b, 5b and 5d, and aligned common fraction radian equivalent for alignment margins that typically fall within ±0.5° unless indicated otherwise. Labels such as "90°a" indicates the local maximum labeled "90°" and adjacent to the vertical transition labeled "a", and so on.

Table A2 presents selected sector angle values for the example phase wheels of figures 4e, 5e and 5f. For presentation purposes within this table, angles are rounded to four significant figures (and so minor differences with sector ratio common fraction alignment values presented in tables 1 and 2 may occur).

Table A2 demonstrates a theme of recurring quantised angular increments, consistent with other results presented throughout. In the phase wheel of figure 4e, κ (based on *mid-line* radial symmetry) may be precisely expressed in terms of the figure 9 y-turning point (minimum) value, α_{min} (see Appendix C), giving $\kappa = 10\alpha_{min}$ (0.25%). Similar outcomes (sector angles based on radial symmetry and being precise integer multiples of α_{min}) are observed within two other (not shown) phase wheels, giving $50\alpha_{min}$ (0.048%) and $10\alpha_{min}$ (0.22%) respectively, and thus across-phase wheel ratios of 1:5:1 based upon these angles.

Table A2. Select sector angles for example phase wheels.

Select sector angle (radians)		
figure 4e	figure 5e	figure 5f
$\eta = 0.01995$	$\xi = 0.014985$	$\eta = 0.008884$
$\kappa = 0.03030$	$\chi = 0.02042$	$\gamma = 0.005917$
$\upsilon = 4 \times 0.01990$	$\varphi = 2 \times 0.02048$	$\chi = 0.01965$
$\tau = 4 \times 0.02207$	$\eta = 5 \times 0.02037$	$\kappa = 2 \times 0.01993$
$\rho = 4 \times 0.02428$	$\mu = 5 \times 0.03082$	$\lambda = 0.021363$
	$\gamma = 3 \times 0.02149$	$\varphi = 0.02261$
	$\alpha = 4 \times 0.02121$	$\rho = 2 \times 0.02262$
	$\beta = 6 \times 0.02149$	$\mu = 2 \times 0.02248$
	$\upsilon = 3 \times 0.019641$	$\beta = 0.032306$
		$\alpha = 0.03283$

Table A1. Horizontal and vertical (upward) $\Delta\phi$ (rounded) pertaining to the annotations of figures 4b, 5b and 5d.

Vertical	$\Delta\phi$ (deg)	$\Delta\phi$ (rad)	Horizontal	$\Delta\phi$ (deg)	$\Delta\phi$ (rad)
figure 4b					
a	105.4	(1/3 + 1/4) π	90°a – 60°	30.0	1/6 π
c	149.4	5/6 π	90°a – 30°	59.7	1/3 π
d	180.1	π	90°a – 45°	44.9	1/4 π
e	180.6	≈ π	60° – 30°	29.8	1/6 π
f	10.0	1/18 π	60° – 45°	15.0	1/12 π
g	4.6	1/36 π	60° – 20°	39.8	2/9 π
i	22.4	1/8 π	30° – 20°	10.1	1/18 π
j	5.1	1/36 π	30° – 25°	5.0	1/36 π
k	19.8	1/9 π	45° – 25°	19.8	1/9 π
b – a	140.5	7/9 π	25° – 20°	5.1	1/36 π
c – a	44.0	≈1/4 π			
b – h	178.1	≈ 2 π			
d – c	30.7	≈1/6 π			
figure 5b					
a	49.8	5/18 π	–50° + 75°	24.9	5/36 π
b	115.6		5° + 30°f	35.1	7/36 π
c	82.8		5° + 45°	50.2	5/18 π
d	172.7		5° + 75°	80.7	≈4/9 π
e	32.7		–30°e + 50°	19.9	1/9 π
f	134.9	3/4 π	–30°e + 75°	44.8	1/4 π
g	102.35		–30°f + 75°	45.6	≈1/4 π
h	91.2		–45° + 75°	30.5	1/6 π
i	254.8		180° + 50°	230.0	
j	333.7		180° + 75°	254.9	
k	145.9				
i – f	119.9	2/3 π			
k – b	30.3	1/3 π			
d – c	90.1	π			
c – e	49.9	5/18 π			
g – c	19.7	1/9 π			
j – e	301.0	≈ –1/3 π			
j – d	161.0	≈ 8/9 π			
j – i	78.9	≈ 4/9 π			
j – f	198.8	≈ 10/9 π			
figure 5d					
a	4.8	1/36 π	115° + 50°	164.8	(3/4 + 1/6) π
b	80.5	4/9 π	115° – 45°	69.5	14/36 π
c	234.4	13/10 π	115° – 0°	114.7	(3/4 - 1/9) π
d	200.5	10/9 π	115° – 40°	74.6	15/36 π
e	29.8	1/6 π	90° + 50°	140.2	7/9 π
f	10.0	1/18 π	90° – 45°	45.0	1/4 π
g	58.9	≈ 1/3 π	90° – 0°	90.1	1/2 π
h	118.8	≈ 2/3 π	90° – 30°	59.7	1/3 π
i	141.85	≈ 7/9 π	90° – 40°	50.0	5/18 π
j	182.3	≈ π	45° – 0°	45.2	1/4 π
j – i	40.4	2/9 π	45° – 30°	14.8	1/12 π
			45° – 40°	5.0	3/36 π
			0° + 50°	50.1	5/18 π
			30° + 50°	80.5	4/9 π
			40° + 50°	90.2	1/2 π
			40° – 0°	40.1	2/9 π
			40° – 30°	9.7	1/18 π

APPENDIX B – CONFIDENCE INTERVAL ANALYSIS FOR TIER 1 $\alpha_{\Delta\phi}$ RATIOS

Figure B1 gives the percentage difference between actual and nominal Tier 1 $\overline{\alpha}_{\Delta\phi}$ ratio values of table 7 with CIs ranging from 80 to 95% for (a) $\overline{\alpha}_{5^0}:\overline{\alpha}_{30^0}$, (b) $\overline{\alpha}_{10^0}:\overline{\alpha}_{20^0}$, (c) $\overline{\alpha}_{10^0}:\overline{\alpha}_{50^0}$, (d) $\overline{\alpha}_{90^0}:\overline{\alpha}_{180^0}$ and (e) $\overline{\alpha}_{1^0}:\overline{\alpha}_{30^0}$. In each figure the nominal ratio is given in the top left corner and the central horizontal line represents the percentage difference based on median (exact) $\overline{\alpha}_{\Delta\phi}$ values.

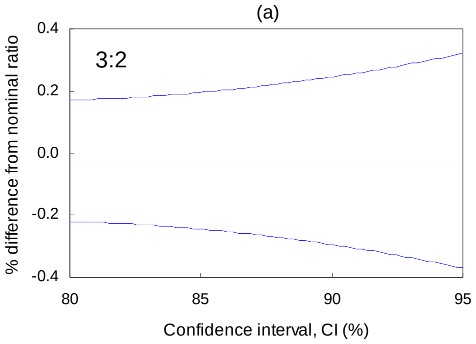

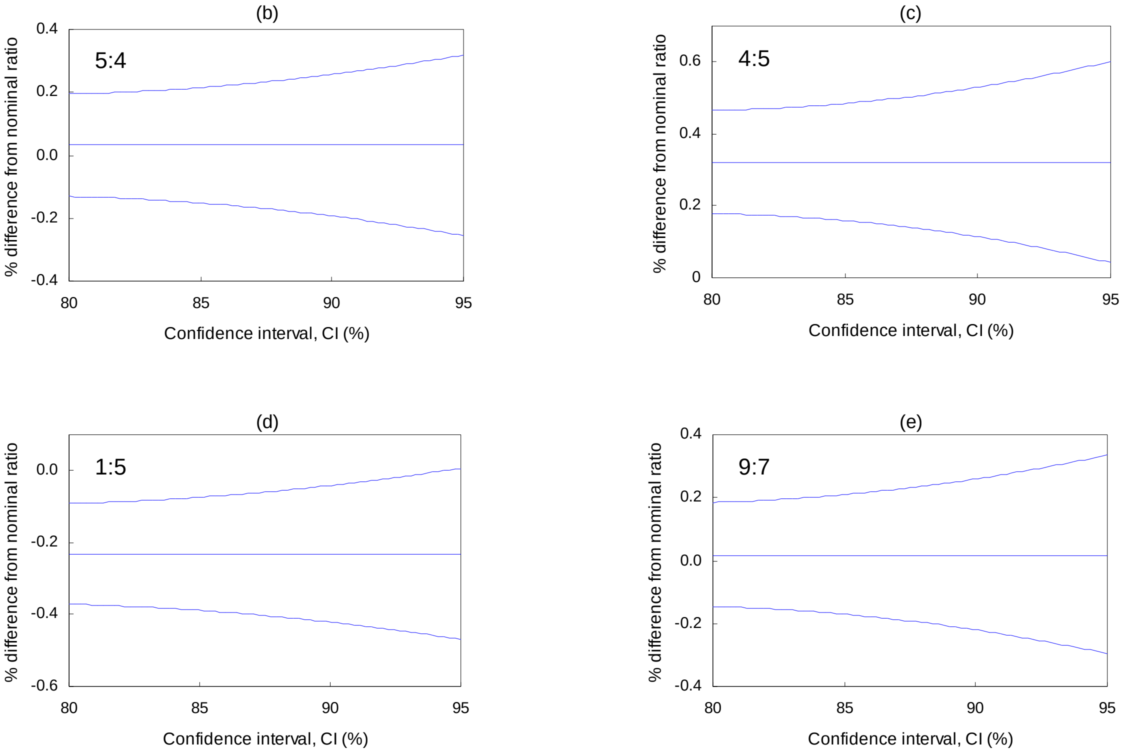

FIGURE B1. **Confidence interval analysis for Tier 1 $\overline{\alpha}_{\Delta\phi}$ ratio values.**

APPENDIX C – RADIAL SEPARATIONS THAT ALIGN WITH $k\alpha_{MIN}$

Separations between Δϕ radials that align with $k\alpha_{min}$ are shown in figure C1 for $\alpha_{min} = 0.174019 \pm 0.000054^o$ (95% CI). α_{min} is determined by the iterative linearization process of the graphical inset and is assumed equal to the *y*-minimum of figure 9. The percentage difference between actual and nominal ($k\alpha_{min}$) separation values is bracketed and the percentage difference (magnitude) averaged over all separations is less than 0.2%.

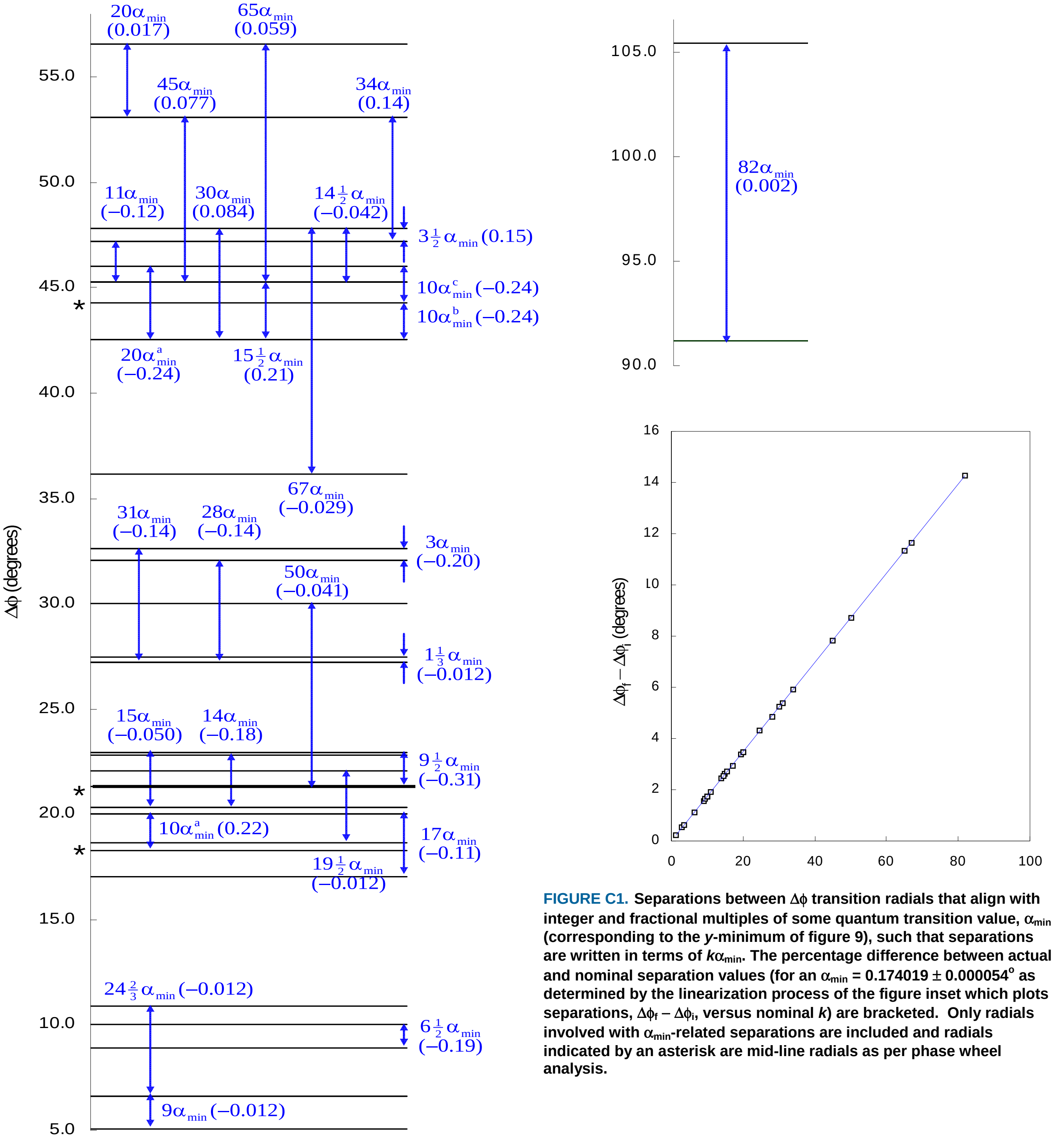

FIGURE C1. Separations between Δϕ transition radials that align with integer and fractional multiples of some quantum transition value, α_{min} (corresponding to the *y*-minimum of figure 9), such that separations are written in terms of $k\alpha_{min}$. The percentage difference between actual and nominal separation values (for an $\alpha_{min} = 0.174019 \pm 0.000054^o$ as determined by the linearization process of the figure inset which plots separations, $\Delta\phi_f - \Delta\phi_i$, versus nominal *k*) are bracketed. Only radials involved with α_{min}-related separations are included and radials indicated by an asterisk are mid-line radials as per phase wheel analysis.

APPENDIX D – CONVENTIONAL EEG PEAKS CONSIDERED AS QUANTUM RESONANCES

The quantised nature of several key findings of the present study intimates a capacity for alpha and other peaks within a conventional EEG frequency spectrum (other than perhaps those without complexity by deriving from the simplest of time-domain oscillations) to be explained as resonant quantum mechanical phenomena. This capacity is now elaborated upon by highlighting several characteristic similarities between *FT′* spectra and the quantum resonances of optical interactions.

Within a field such as quantum mechanics a resonance peak of some frequency spectrum is deconstructed and well understood, with quantum resonance literature spanning decades and presenting solid mathematical and physical underpinnings of such phenomena. For example, a 1973 theoretical study and review [77] associates the energy resonances of quantum systems with the exact complex poles of an appropriate Green's function (sophisticated EEG simulation models also write scalp potentials in terms of a Green's function that describes the conductive head volume [4]).

Another example of quantum resonances being well understood is found within a more recent and substantive review [78] of resonance phenomena that are particularly important for two-body atomic and molecular interactions (e.g., optical and radiative collisions). The theoretical formalisms of such interactions often depict the interacting atoms as forming a temporary molecule whereby a transition is seen to occur between initial and final molecular states as a consequence of some inputted transition-completing energy (e.g., collisional and applied laser energies). Two resonance types that readily appear when solving Schrödinger-based differential equations describing such two-body interactions are *shape* and *Feshbach* resonances.

Shape resonances are attributed to the shape of the governing molecular potential that produces quasibound states in a governing potential well; they are oscillatory and have been associated with a rapid increase in the phase shift (that occurs through odd multiples of 90^o) of scattering amplitudes. Feshbach resonances are attributed to the resonances between closed and open channels[5], or alternatively are described as being made possible by the presence of a molecular bound state that is reasonably coupled to states (of different symmetry and form) of the colliding atom pair. Depending on subtype, Feshbach resonances are either magnetically or optically tuneable in respect to inputted energy [78–85].

A contextually noteworthy interaction affected by such resonances is the laser assisted charge transfer (LACT) process, $\mathrm{H}^+ + \mathrm{Na(3s)} + \text{laser energy} \rightarrow \mathrm{H}(n=2) + \mathrm{Na}^+$ [86], abbreviated as H^+-Na. This reaction is noteworthy because the action potential that generates the EEG analogously represents a governing well-shaped potential of a molecular system undergoing charge (ion) transfer with the assistance of inputted (cellular rather than laser) energy (of course for the action potential ion transfer occurs from extracellular fluid rich in Na^+ and Cl^- ions to intracellular fluid rich in K^+ ions via transport channels through the phospholipid bilayer of the nerve cell membrane). This analogous comparison continues the case for peaks within the conventional EEG frequency spectrum having a quantum resonance origin (note that interactions such as optical collisions, LACT, and laser induced collisional energy transfer (LICET), which are further exemplified by examples below, are considered closely related processes [83,87], and so are all generically referred to as optical collisions for ongoing discussion).

Many optical collision systems involving chemical elements of the action potential's ion transport process have in fact long been studied[6] with select examples including: H^+-Na [86]; Na-Na at ultracold temperatures [82]; Na-noble gas [85]; He-He and He-other noble gases, including at room temperature [83,84,88]; Sr-Ca [89]; Na-Ca [90]; Rb-Na [80]; and Rb-K [91].

As per Subsection 5.5, within the formalism of such optical collisions the total molecular potential often includes a centripetal term (that relates to the centripetal motion of interacting atoms), V_c, such that $V_c \propto J(J+1)$, where J is a quantum number labelling the eigenvalues (energy solutions) associated with the total molecular angular momentum. For many of these systems, reaction cross-section profiles are oscillatory (as a function of inputted energy) with strong, specific and complex shape resonances that are identifiable with particular values of J. Such resonance characteristics are most pronounced in systems of relatively low mass, low temperature (i.e., approximately room temperature and below) and/or close internuclear separation, and accordingly are especially apparent within the above Na-noble gas, He-He, and Na-Na examples. In addition to the elemental and environmental contextual analogies that can subsequently be drawn, resonances within the above-described systems also share several physical characteristics with *FT′* spectra:

- Like *FT′* spectra, shape resonances within reaction cross-section profiles can be constructed from harmonics, that span and constitute a frequency spectrum, with oscillatory decay.

- Shape resonances typically involve rapid 90^o phase shifts and the present study identifies a primary Family based upon $\Delta\phi_c = 90^o$ (and recall the dominant $\Delta\phi = 90^o$ in figure 7d).

---

[5] Channels are fragmentation modes of the collision's composite system with open channels allowed under known conservation laws such as the conservation of energy [81].

[6] Many comparable studies may be cited (e.g., see review [78]) but are too numerous to list, with the vintage of presented examples (from the 1970s onwards) highlighting the depth of understanding and establishment of associated quantum resonances.

- Shape resonances and the EEG (and therefore FT' spectra) share electric dipole origins. That is, it is often appropriate to describe the molecular binding potentials (e.g., van der Walls, adiabatic) of optical collisions as "dipole-dipole-type" (representative of weak interactions responsible for a departure from ideal gas behaviour). These potentials arise because the interacting (typically stable) atoms or molecules often possess permanent diploes due to electron affinity considerations (or even oscillating dipoles due to fluctuating quantum mechanical behaviour). For the EEG, dipole-type interactions play a role within the ion transport processes of the action potential, not just in terms of interactions between ions but also within the complex manner of ion transport channel gating across the nerve cell membrane. Not surprisingly then, dipole approximations to cortical electric current sources (or more specifically dipole moment per unit volume approximations of complex current distributions throughout cortical regions) provide the basis for most realistic EEG simulation models which assume (including for geometric convenience) that EEG sources consist of thousands of dipoles orientated perpendicular to the cortical surface [4,5].

Additional analogies based upon mathematical functionalities may also be drawn. For example, parabolic and linear functionalities are identified with prominence within the present study, while for magnetically tuneable Feshbach resonances, in the vicinity of expected resonance where two channels are strongly coupled (and in the limit of large positive scattering length), the binding energy (or molecular state energy) depends parabolically on the detuning of the applied magnetic field, while away from the region of classical resonance the energy varies linearly with the magnetic detuning [78].

In summary, the following characteristics of showcased resonance-affected optical collisions draw analogy with the EEG on the basis of: (i) shared characteristics with the J-dependent oscillatory nature of reaction cross-sections (that may for example be derived from scattering matrices constructed of oscillatory spherical Bessel functions); (ii) the involved chemical elements (having overlap with elements of the action potential's ion transport processes) and potentials; and (iii) the addition of energy to provide molecular transition completion or excitation, including charge transfer (cellular energy must directly or indirectly be inputted for action potential charge transfer).

It can thus be stated that while the ion transport processes of the action potential may involve physical conditions dissimilar to the previously cited subset of example optical collisions (e.g., dissimilar temperature, matter phase, manner of energy excitation such as cellular rather than laser), based on analogous comparisons made the existence of oscillatory resonances within a fully quantum treatment of the action potential would be unsurprising, if not expected, and indeed such a treatment is considered necessary to fully interpret FT' resonances of the EEG into the future.

REFERENCES

1. Aron J. 2015 DNA in glass – the ultimate archive. *New Scientist* **225,** 15.
2. Simeoni RJ. A discrete oscillator phase noise effect applied within phase-shift keying RF digital signal modulation. In: 9th International Conference on Signal Processing and Communication Systems; 2015 December 14-16; Cairns, Australia. p. 1-9. (https://doi.org/10.1109/ICSPCS.2015.7391745)
3. Rennie CJ, Robinson PA, Wright JJ. 2002 Unified neurophysical model of EEG spectra and evoked potentials. *Biol. Cybern.* **86,** 457-471. (https://doi.org/10.1007/s00422-002-0310-9)
4. Srinivasan R, Winter WR, Nunez PL. 2006 Source analysis of EEG oscillation using high-resolution EEG and MEG. *Prog. Brain Res.* **159,** 29-42. (https://doi.org/10.1016/s0079-6123(06)59003-x)
5. Nunez PL, Nunez MD, Srinivasan R. 2019 Multi-scale neural sources of EEG: genuine, equivalent, and representative. A tutorial review. *Brain Topogr.* **32,** 193-214. (https://doi.org/10.1007/s10548-019-00701-3)
6. Salimpoor VN, Benovoy M, Larcher K, Dagher A, Zatorre RJ. 2011 Anatomically distinct dopamine release during anticipation and experience of peak emotion to music. *Nat. Neurosci.* **14,** 257-262. (https://doi.org/10.1038/nn.2726)
7. Chandra ML, Levitin DJ.2013 The neurochemistry of music. *Trends Cogn. Sci.* **17,** 179-193. (https://doi.org/10.1016/j.tics.2013.02.007)
8. Stender J, Gosseries O, Bruno M, Charland-Verville V, Vanhaudenhuyse A, Demertzi A, Chantelle C, Thonnard M, Thibaut A, Heine L, et al. 2014 Diagnostic precision of PET imaging and functional MRI in disorders of consciousness: a clinical validation study. *Lancet* **384,** 514-522. (https://doi.org/10.1016/S0140-6736(14)60042-8)
9. Kanduri C, Raijas P, Ahvenainen M, Philips AK, Ukkola-Vuoti L, Lähdesmäki H, Järvelä I. 2015 The effect of listening to music on human transcriptome. *PeerJ* **3**:e830. (https://doi.org/10.7717/peerj.830)
10. Itthipuripat S, Sprague TC, Serences JT. 2019 Functional MRI and EEG index complementary attentional modulations. *J. Neurosci.* **39,** 6162-6179. (https://doi.org/10.1523/JNEUROSCI.2519-18.2019)
11. Noor NSEM, Ibrahim H. 2020 Machine learning algorithms and quantitative electroencephalography predictors for outcome prediction in traumatic brain injury: a systematic review. *ACCESS* **8,** 102075-102092. (https://doi.org/10.1109/ACCESS.2020.2998934)
12. Blasco MA, Redleaf MI. 2014 Cochlear implantation in unilateral sudden deafness improves tinnitus and speech comprehension: meta-analysis and systematic review. *Otol. Neurotol.* **35,** 1426-1432. (https://doi.org/10.1097/MAO.0000000000000431)
13. Lou YH-L, da Cruz L. 2014 A review and update on the current status of retinal prosthesis. *Br. Med. Bull.* **109,** 31-44. (https://doi.org/10.1093/bmb/ldu002)
14. Krucoff MO, Rahimpour S, Slutzky MW, Edgerton VR, Turner DA. 2016 Enhancing nervous system recovery through neurobiologics, neural interface training, and neurorehabilitation. *Front. Neurosci.* **10,** 584. (https://doi.org/10.3389/fnins.2016.00584)
15. Gilbert F, Cook M, O'Brian T, Illes J. 2019 Embodiment and estrangement: results from a first-in-human “intelligent BCI” trial. *Sci. Eng. Ethics* **25,** 83-96. (https://doi.org/10.1007/s11948-017-0001-5)
16. Drew L. 2019 The ethics of brain-computer interfaces. *Nature* **571,** S19-S21. (https://doi.org/10.1038/d41586-019-02214-2)
17. Baldermann JC, Schüler T, Huys D, Becker I, Timmermann L, Jessen F, Visser-Vandewalle V, Kuhn J. 2016 Deep brain stimulation for Tourette-syndrome: A systematic review and meta-analysis. *Brain Stimul.* **9,** 296-304. (https://doi.org/10.1016/j.brs.2015.11.005)
18. Keifer Jr OP, Riley JP, Boulis NM. 2014 Deep brain stimulation for chronic pain: intracranial targets, clinical outcomes, and trial design considerations. *Neurosurg. Clin. N. Am.* **25,** 671-692. (https://doi.org/10.1016/j.nec.2014.07.009)

19. Kisely S, Li A, Warren N, Siskind D. 2018 A systematic review and meta-analysis of deep brain stimulation for depression. *Depress. Anxiety* **35,** 468-480. (https://doi.org/10.1002/da.22746)
20. Gaynes BN, Lloyd SW, Lux L, Gartlehner G, Hansen RA, Brode S, Jonas DE, Evans TS, Viswanathan M, Lohr KN, et al. 2014 repetitive transcranial magnetic stimulation for the treatment of depression: a systematic review and meta-analysis. *J. Clin. Psychiat.* **75,** 477-489. (https://doi.org/10.4088/JCP.13r08815)
21. Finnigan SP, Walsh M, Rose SE, Chalk JB. 2007 Quantitative EEG indices of sub-acute ischaemic stroke correlate with clinical outcomes. *Clin. Neurophysiol.* **118,** 2525-2532. (https://doi.org/10.1016/j.clinph.2007.021)
22. Cao T, Wan F, Wong CM, da Cruz JN, Hu Y. 2914 Objective evaluates of fatigue by EEG spectral analysis in steady-state visual evoked potential-based brain-computer interfaces. *Biomed. Eng. Online* **13,** 28. (https://doi.org/10.1186/1475-925X-13-28)
23. Hagihira S. 2015 Changes in the electroencephalogram during anaesthesia and their physiological basis. *Br. J. Anaesth.* **115,** i27-i31. (https://doi.org/10.1093/bja/aev212)
24. Nunez PL, Wingeier BM, Silberstein RB. 2001 Spatial-temporal structures of human alpha rhythms: theory, micro-current sources, multiscale measurements, and global binding of local networks. *Hum. Brain Mapp.* **13,** 125-164. (https://doi.org/10.1002/hbm.1030)
25. Bowyer SM. 2016 Coherence a measure of the brain networks: past and present. *Neuropsychiatr. Electrophysiol.* **2,** 1. (https://doi.org/10.1186/s40810-015-0015-7)
26. Schwarz G, Voit-Augustin H, Litscher G, Baumgartner A. 2003 Specific problems in interpretation of absolute values of spectral edge frequency (SEF) in comparison to bispectral index (BIS) for assessing depth of anesthesia. *Internet J. Neuromonit.* **3,** 1-22. (https://doi.org/10.5580/12ca)
27. Billard V, Gambus PL, Chamoun N, Stanski DR, Shafer SL. 1997 A comparison of spectral edge, delta power, and bispectral index as EEG measures of alfentanil, propofol, and midazolam drug effect. *Clin. Pharmacol. Ther.* **61,** 45-58. (https://doi.org/10.1016/S0009-9236(97)90181-8)
28. Stoeckel H, Schwilden H, Lauven P, Schüttler H. 1981 EEG indices for evaluation of depth of anaesthesia: the median of frequency distribution. *Br. J. Anaesth.* **53,** 117P.
29. Ning T, Bronzino JD. 1990 Autoregressive and bispectral analysis techniques: EEG applications. *IEEE Eng. Med. Biol.* **March,** 47-50. (https://doi.org/10.1109/51.62905)
30. Sigl JC, Chamoun NG. 1994 An introduction to bispectral analysis for the electroencephalogram. *J. Clin. Monit.* **10,** 392-404. (https://doi.org/10.1007/BF01618421)
31. Lipton JM, Dabke KP, Alison JF, Cheng H, Yates L, Brown TIH. 1998 Use of the bispectrum to analyse properties of the human electrocardiograph. *Austral. Phys. Eng. Sci. Med*. **2,** 1-10.
32. Muthuswamy J, Sherman DL, Thakor NV. 1999 Higher-order spectral analysis of burst patterns in EEG. *IEEE Trans. Biomed. Eng*. **46,** 92-99. (https://doi.org/10.1109/10.736762)
33. Goldberger AL, Rigney DR, West BJ. 1990 Chaos and fractals in human physiology. *Sci. Am.* **262,** 40-49. (https://doi.org/10.1038/scientificamerican0290-42)
34. Simeoni RJ, Mills PM. 2003 Does the Fibonacci sequence exist within our brain waves? *The Physicist* **40**, 62-65.
35. Schieke K, Wacker M, Benninger F, Feucht M, Leistritz L, Witte H. 2015 Matching pursuit-based time-varient bispectral analysis and its application to biomedical signals. *IEEE Trans. Biomed. Eng*. **62,** 1937-1948. (https://doi.org/10.1109/TBME:2015.2407573)
36. Nahm W, Stockmanns G, Petersen J, Gehring H, Konecny E, Kochs HD, Kochs E. 1999 Concept for an intelligent anaesthesia EEG monitor. *Med. Inform. Internet.* **24,** 1-9. (https://doi.org/10.1080/146392399298492)
37. Schneider G, Gelb AW, Schmeller B, Tschakert R, Kochs E. 2003 Detection of awareness in surgical patients with EEG-based indices – bispectral index and patient-based index. *Br. J. Anaesth.* **91,** 329-335. (https://doi.org/10.1093/bja/aeg188)
38. Onuki K, Onuki N, Imamura T, Yamanishi Y, Yoshikawa S, Hagihira S, Shimada J, Nagasaka H. 2001 Pentazocine increases bispectral index without surgical stimulation during nitrous oxide-sevoflurane. *J. Anesth.* **25,** 946-949. (https://doi.org/10.1007/s00540-011-1224-2)
39. Hayashi K, Mukai N, Sawa T. 2014 Simultaneous bicoherence analysis of occipital and frontal electroencephalograms in awake and anesthetized subjects. *Clin. Neurophysiol.* **125,** 194-201. (https://doi.org/10.1016/j.clinph.2013.06.024)
40. Chua KC, Chandran V, Acharya UR, Lim CM. 2011 Application of higher order spectra to identify epileptic EEG. *J. Med. Syst.* **35,** 1563-1571. (https://doi.org/10.1007/s10916-010-9433-z)
41. Schieke K, Wacker M, Piper D, Benninger F, Feucht M, Witte H. 2014 Time-variant, frequency-selective, linear and nonlinear analysis of heart rate variability in children with temporal and lobe epilepsy. *IEEE Trans. Biomed. Eng*. **61,** 1798-1808. (https://doi.org/10.1109/TBME.2014.2307481)
42. Zhang JW, Zheng CX, Xie A. 2000 Bispectrum analysis of focal ischemic cerebral EEG signal using third-order recursion method. *IEEE Trans. Biomed. Eng*. **47,** 352-359. (https://doi.org/10.1109/10.827296)
43. Li X, Li D, Voss LJ, Sleigh JW. 2009 The comodulation measure of neuronal oscillations with general harmonic wavelet bicoherence and application to sleep analysis. *NeuroImage* **48,** 501-514. (https://doi.org/10.1016/j.neuroimage.2009.07.008)
44. Wacker M, Schiecke K, Putsche P, Eiselt M, Witte H. 2012 A processing scheme for time-variant phase analysis in EEG burst activity of premature and full-term newborns in quiet sleep: a methodological study. *Biomed. Tech. (Berl.)* **57,** 491-505. (https://doi.org/10.1515/bmt-2012-0034)
45. Simeoni RJ, Mills PM. 2003 Quadriceps muscles vastus medialis obliques, rectus femoris and vastus lateralis compared via electromyogram bicoherence analysis. *Austral. Phys. Eng. Sci. Med*. **26**, 125-131. (https://doi.org/10.1007/BF03178782)
46. Al-Fahoum A, Al-Fraihat A, Al-Araida A. 2014 Detection of cardiac ischaemia using bispectral analysis approach. *J. Med. Eng. Technol.* **38,** 311-316. (https://doi.org/10.3109/03091902.2014.925983)
47. Simeoni RJ, Mills PM. 2003 Bicoherence analysis of quadriceps electromyogram during isometric knee extension. *Austral. Phys. Eng. Sci. Med*. **26,** 12-17. (https://doi.org/10.1007/BF03178691)
48. Simeoni RJ, Mills PM. Bispectral analysis of Alzheimer's electroencephalogram: a preliminary study. In: Allen B, Lovell N, editors, Proceedings of the World Congress on Medical Physics and Biomedical Engineering; 2003 August 24-29; Sydney, Australia
49. Lipton JM, Dabke KP. 1996 Bispectral properties of the simplest dissipative nonautonomous chaotic circuit. *Int. J. Bifurcat. Chaos* **6,** 2419- 2425. (https://doi.org/10.1142/S0218127496001569)
50. Khandra L, Al-Fahoum AS, Binajjaj S. 2005 A quantitative analysis approach for cardiac arrhythmia classification using higher order spectral techniques. *IEEE Trans. Biomed. Eng*. **52,** 1840-1845. (https://doi.org/10.1109/TBME.2005.856281)
51. Palva S, Palva JM. 2007 New vistas for α-frequency band oscillations. *Trends Neurosci.* **30,** 150-158. (https://doi.org/10.1016/j.tins.2007.02.001)
52. Raghuveer MR. 1990 Time domain approaches to quadratic phase coupling estimation. *IEEE Trans. Automat. Contr.* **35,** 48-56. (https://doi.org/10.1109/9.45142)
53. Zhou G, Giannakis GB. 1995 Retrieval of self-coupled harmonics. *IEEE Trans. Signal Process.* **43,** 1173-1186.
54. Schack B, White H, Helbig M, Schelenz Ch, Specht M. 2001 Time-variant non-linear phase-coupling analysis of EEG burst patters in sedated patients during electroencephalic burst suppression period. *Clin. Neurophysiol*. **112,** 1388-1399. (https://doi.org/10.1016/S1388-2457(01)00577-6)
55. Smedler E, Uhlén P. 2014 Frequency decoding of calcium oscillations. *Biochem. Biophys. Acta.* **1840,** 964-969, 2014. (https://doi.org/10.1016/j.bbagen.2013.11.015)
56. Nayak K, 2002 Electroencephalogram (EEG) Data, SCRI, Florida State University. Originally available from http://www.scri.fsu.edu/~nayak/chaos/data.html.
57. Cameron JR, Skofronick JG. 1978 *Medical physics*, 1st ed. New York: John Wiley and Sons, Inc. (https://doi.org/10.1002/jcu.1870060522)
58. Terzano MG, Parrino L, Sherieri A, Chervin R, Chokroverty S, Guilleminault C, Hirshkowitz M, Mahowald M, Moldofsky H, Rosa A, et al. 2001 Atlas, rules, and recording techniques for the scoring of cyclic alternating pattern (CAP) in human sleep. *Sleep Med.* **2,** 537-553. (https://doi.org/10.1016/s1389-9457(01)00149-6)

59. St. Vincent's University Hospital/University College Dublin. 2011 Sleep Apnea Database (revised version). (https://doi.org/10.13026/C26C7D)
60. Goldberger A, Amaral L, Glass L, Hausdorff J, Ivanov PC, Mark RG, Mietus JE, Moody GB, Peng C-K, Stanley HE, et al. 2000 PhysioBank, PhysioToolkit, PhysioNet: components of a new research resource for complex physiological signals. *Circulation* [Online] **101,** e215-e220. (https://doi.org/10.1161/01.CIR.101.23.e215)
61. Marcuse LV, Schneider M, Mortati KA, Donnelly KM, Arnedo V, Grant AC. 2008 Quantitative analysis of the EEG posterior-dominant rhythm in healthy adolescents. *Clin. Neurophysiol.* **119,** 1778-1781. (https://doi.org/10.1016/j.clinph.2008.02.023)
62. Daniel WW. 1995 *Biostatistics a foundation for analysis in the health sciences*, 6th ed. New York: John Wiley and Sons, Inc.
63. Sklar B. 2001 *Digital communications fundamentals and applications*, 2nd ed. Upper Saddle River, New Jersey: Prentice Hall PTR.
64. Harris FJ. 1978 On the use of windows for harmonic analysis with the discrete Fourier transform. *Proc. IEEE* **66,** 51-83.
65. Simeoni RJ. 2008 Noble gas magic numbers: from quarks to quasars, *Austral. Math. Soc. Gaz.* **35,** 93-96.
66. Simeoni RJ. 2003 Bohr's model of atomic hydrogen extended to include electron rotational kinetic energy. *Physics in Canada.* **59**, 309-311.
67. Bransden BH, Joachain CJ. 1992 *Physics of atoms and molecules*. Essex: Longman Scientific and Technical.
68. Mack K. 2016 The pattern of matter. *Cosmos* **66,** 35.
69. Gordan RL, Jacobs MS, Schuele CM, McAuley JD. 2015 Perspectives on the rhythm-grammar link and its implications for typical and atypical language development. *Ann. N.Y. Acad. Sci.* **1337,** 16-25. (https://doi.org/10.1111/nyas.12683)
70. Gómez-Romero M, Jiménez-Palomares J, Rodriguez-Mansilla J, Flores-Nieto A, Garrido-Ardila EM, González-López-Arza MV. 2017 Benefits of music therapy on behaviour disorders in subjects diagnosed with dementia: A systematic review. *Neurología* **32,** 253-263. (https://doi.org/10.1016/j.nrl.2014.11.001)
71. Johnston B. 1964 Scalar order as a compositional resource. *Perspect. New Music* **2,** 56-76. (https://doi.org/10.2307/832482)
72. Powell J. 2011 *How music works: the science and psychology of beautiful sounds, from Beethoven to the Beatles and Beyond.* New York: Little, Brown Spark.
73. Gero S, Whitehead H, Rendell L. 2016 Individual, unit and vocal clan level identity cues in sperm whale codas. *R. Soc. Open. Sci.* **3:**150372,1-12. (https://doi.org/10.1098/ros.150372)
74. Rendell L, Whitehead H. 2003 Vocal clans in sperm whales (physeter macrocephalus). *Proc. R. Soc. Lond. B* **270,** 225-231. (https://doi.org/10.1098/rspb.2002.2239)
75. Whitehead H, Antunes R, Gero S, Wong SNP, Engelhaupt D, Rendell L. 2012 Multilevel societies of female sperm whales (physeter macrocephalus) in the Atlantic and Pacific: why are they so different? *Int. J. Primatol.* **33,** 1142-1164. (https://doi.org/10.1007/s10764-012-9598-z)
76. Mishima Y, Morisaka T, Itoh M, Matsuo I, Sakaguchi A, Miyamoto Y. 2015 Individuality embedded in the isolation calls of captive beluga whales (Delphinapterus leucas). *Zoological Lett.* **1,** 1142-1164. (https://doi.org/10.1186/s40851-015-0028-x)
77. More RM, Gerjuoy E. 1973 Properties of resonance wave functions. *Phys. Rev. A* **7,** 1288-1303. (https://doi.org/10.1103/PhysRevA.7.1288)
78. Chin C, Grimm R, Julienne P, Tiesinga E. 2010 Feshbach resonances in ultracold gases. *Rev. Mod. Phys.* **82,** 1225-1289. (https://doi.org/10.1103/RevModPhys.82.1225)
79. Vahala LL, Julienne PS, Havey MD. 1986 Non-adiabatic theory of fine-structure branching cross sections for Na-He, Na-Ne and Na-Ar optical collisions. *Phys. Rev. A: At. Mol. Opt. Phys*. **34,** 1856-1868. (https://doi.org/10.1103/PhysRevA.34.1856)
80. Cheron B, Kucal H, Hennecart D. 1990 Laser-induced collisional energy transfer in a rubidium-sodium mixture: experiment and interpretation in the framework of the non-adiabatic collision theory. J.*Phys. B: At. Mol. Opt. Phys*. **23,** 4281-4291. (https://doi.org/10.1088/0953-4075/23/23/011)
81. Bransden BH, Joachain CJ. 1992 *Physics of atoms and molecules*. Essex: Longman Scientific and Technical.
82. Moerdijk AJ, Verhaar BJ, Axelsson A. 1995 Resonances in ultracold collisions of ^{6}Li, ^{7}Li and ^{23}Na. *Phys. Rev. A* **51,** 4852-4861. (https://doi.org/10.1103/PhysRevA.51.4852)
83. Simeoni RJ, Peach G, Whittingham IB. 1996 Theoretical study of a LICET-like process in singlet helium systems. *J. Phys. B: At. Mol. Opt. Phys.* **29**, 5567-5582. (https://doi.org/10.1088/0953-4075/29/22/028)
84. Simeoni RJ, Peach G, Whittingham IB. 1997 A laser induced collisional energy transfer (LICET) process involving metastable helium. J.*Phys. B: At. Mol. Opt. Phys*. **30,** 1071-1075. (https://doi.org/10.1088/0953-4075/30/41024)
85. Lavert-Ofir E, Shagam Y, Henson AB, Gersten S, Klos J, Zuchowski PS, Narevicius J, Narevicius E. 2014 Observation of the isotope effect in sub-kelvin reactions. *Nat. Chem.* **6,** 332-335. (https://doi.org/10.1038./nchem.1857)
86. Hsu YP, Olsen RE. 1985 Satellite structure in laser-assisted charge-transfer cross sections. *Phys. Rev. A* **32,** 2707-2711. (https://doi.org/10.1103/PhysRevA.32.2707)
87. Szudy J, Baylis WE. 1996 Profiles of line wings and rainbow satellites associated with optical and radiative collisions. *Phys. Rep*. **266,** 199-225. (https://doi.org/10.1016/0370-1573(95)00054-2)
88. Simeoni RJ. 1996 A theoretical investigation of laser induced collisional energy transfer in rare gases. PhD thesis, Department of Physics, James Cook University of North Queensland, Australia.
89. Falcone RW, Green WR, White JC, Young JF, Harris SE. 1977 Observation of laser-induced inelastic collisions. *Phys. Rev. A* **15,** 1333-1335. (https://doi.org/10.1103/PhysRevA.15.1333)
90. Debarre A. 1983 High-resolution study of light-induced collisional energy transfer in Na-Ca mixture. *J. Phys. B: At. Mol. Phys.* **16,** 431-436. (https://doi.org/10.1088/0022-3700/16/3/017)
91. Cheron B, Lemery H. 1982 Observation of laser induced collisional energy transfer in a rubidium-potassium mixture. *Opt. Commun.* **42,** 109-112. (https://doi.org/10.1016/0030-4018(82)90376-5)

Appendix B

Chronic Fatigue Syndrome: A Quantum Mechanical Perspective
(9 May 2022)

Appendix Disclaimer: The inclusion of this article of academic journalism (also containing a shared Case Study with associated hypothesis) within the present report, permitted under the Author copyright maintenance policy of the article's host journal, does not necessarily indicate report endorsement by the host journal, especially given the report's hypothetical aspects and abstract thought discussions.

UNETJOSS
Journal of Science and Society
in association with ChristianUniversityforAustralia.org.au

Supplementary Communication (Academic Journalism, Case Study, Justified Hypothesis, Preliminary Results)
https://doi.org/10.52042/UNETJOSS020103

Chronic Fatigue Syndrome: A Quantum Mechanical Perspective

Ricardo J. Simeoni
Research and Development, Neurödinger, Sunshine Coast, QLD 4575 Australia.

Corresponding author: Ricardo J. Simeoni (rsimeoni@neurodinger.com, www.neurodinger.com).

1. INTRODUCTION

1.1 GENERAL

Chronic fatigue syndrome (CFS), also known as myalgic encephalomyelitis (ME) or systemic exertional intolerance disease (SEID), is an illness dominated by long-term fatigue persisting for more than six months, incapacitating to the point of sufferers being bedridden or housebound in some cases, and unexplained by some other underlying medical condition. CFS is also often characterised by unrefreshing sleep, post-exertional discomfort ranging from malaise to extreme exhaustion, orthostatic (upright posture) intolerance, muscle pain, cognitive impairment (including the commonly described symptom of "brain fog"), and deterioration in cellular bioenergetics [1–3].

Scientific estimates of the world-wide population percentage that suffer from CFS naturally vary, but a conservative estimate based on several studies is at least 0.4%, thereby equating to millions world-wide [1–4]. Thankfully, after decades of dismissal by some quarters, leading to despair and exasperation of sufferers, CFS is now widely accepted as a legitimate illness. However, while depreciating labels such as "yuppy flu" have subsequently been banished to recent history, this new-found acceptance provides comfort for sufferers only up to a certain point. Viz., CFS is still far from fully understood and is often described as a complex, multisystem illness with no clear pathological mechanisms or diagnostic biomarkers [1–3], from which treatment uncertainty ensues [1,2]. Sadly, due in no small part to this uncertainty and the illness characteristics of the opening paragraph, the suicide rate of CFS sufferers has been reported as approximately seven times that of their healthy counterparts [1,5].

The article *briefly* reviews the medical science of Chronic Fatigue Syndrome and the illness' impact on society, while also sharing a 29-year Case Study with an intriguing hypothesis-based outcome including quantifiable relief. Is this outcome just a one-off mathematical curiosity?, or, will it be verified in the fullness of time as being profoundly grounded in Quantum Mechanics?

The economic and other social impacts of CFS are difficult to determine because of the arbitrariness of case definitions, lack of evidence including prevalence data, diagnostic inability of some physicians due to factors such as disbelief and lack of understanding (one major survey [4] reveals that 62% of sufferers are not confident in their general physician's understanding), and difficulty many sufferers have in explaining the symptoms of their illness (another survey [2] shows that a majority or substantial proportion, depending on factors such as country of origin, have difficulty explaining their illness to not only physicians but also family and friends). Societal impacts of CFS have nonetheless been assessed by various committees (e.g., associated with the United States' Institute of Medicine) and working/action groups (e.g., associated with the European Union). As expected, the economic impact of CFS is formally declared to be significant, with the net income of a CFS household in Europe being substantially lower than general population households (i.e., individual productivity effect), and the total annual cost burden being tens of billions of dollars in the United States alone [1–4].

1.2 CFS AETIOLOGY

The World Health Organization generally classifies CFS as a neurological illness involving the central nervous system. Some notable and more specific examples of proposed CFS aetiology components are summarised below, with these examples reflecting the complex multisystem nature of CFS and not necessarily being mutually exclusive:

- Recent studies suggest that CFS arises from functional changes in the brain, with spectroscopic and inflammatory brain changes (e.g., following repeated exercise) also demonstrated. However, uncertainty over the character,

An extended version of this superseding article was published May 9, 2022 to support the first World ME Day (themed *#LearnFromME*) of May 12.

location and propensity of such changes remains and the need for further functional neuroimaging studies is recognised [2,3,6,7].

- A significant increase in red blood cell (RBC) stiffness is reported in CFS, suggesting that compromised RBC transport through microcapillaries may contribute to CFS aetiology and that this diminished deformability could form the basis of a first-pass diagnostic test [8]. Further to this point, the previously identified CFS characteristic of orthostatic intolerance (estimated to occur in up to 97% of cases) is linked to under-oxygenatation of the brain to which diminished RBC deformability is thought to be a contributing factor [9].

- Unusual RBC shape, leading to reduced blood flow and changes in molecular docking on the RBC surface, is reported in CFS [10]. The subsequent increase in the number of stomatocytes (RBCs that have lost their typical concave shape, due for example to membrane defect), adds to the previous point of diminished RBC deformability to support poor microcirculation as contributing to CFS aetiology.

- Dysfunction of mitochondria (subcellular organelles within the cytoplasm of aerobic cells) is found in CFS, with the interference of adenosine triphosphate (ATP) production being one of several consequences within the explanatory pathological pathway [11] (ATP is fundamentally essential for cellular-level metabolic energy requirements as outlined in Section 3).

- CFS is largely resolved as *not* being attributable to some ongoing infection, endocrine disorder, or psychiatric condition [3,6]. While some similarly do not assign an immunological disorder attribution, more often over-stimulation or over-reaction of the immune system (hyperimmune response), impaired immune system response, immuno-inflammatory, and oxidative damage to the immune system, are all utilised expressions associated with CFS [3,6,8,11–13], which in several research circles is described as a neuroimmune disease [1,11,14]. This immunological quandary again highlights the complexity of the ongoing medical challenge at hand.

1.3 VIRAL TRIGGERS OF CFS

One clear aspect of CFS is that underlying pathophysiology implicates a range of different acute infections as onset triggers in a *significant minority* of cases (i.e., infections like Epstein-Barr, Ross River and the 2003 outbreak variant of Severe Acute Respiratory Syndrome, or SARS, viruses). No other medical or psychological factors are definitively implicated in CFS [7]. For many observers such triggerings are mindful of, if not directly related to, the crippling fatigue that is widely reported within contemporary media and recent studies as a lasting symptom of COVID-19. Such COVID-19-triggred CFS has led to the coined phrases of COVID-19 "long-haulers" or "long COVID", and has returned CFS to the public awareness spotlight [12]. However, too familiarly the lack of definitive CFS biomarkers is again confirmed by long COVID research, and sadly the dismissive attitudes of some in the medical profession is also a point of exasperation for long COVID sufferers [12], contributing for example to the in-desperation-establishment of a "long COVID kids" Facebook site in the United Kingdom.

1.4 CFS TREATMENT

Established treatments, such as cognitive behaviour therapy (CBT) and graded exercise therapy (GET), primarily aim to manage the symptoms and improve the overall function of sufferers. The confounding nature of CFS extends to these treatments, since there is wide ongoing debate over their effectiveness [1,15]. For example, while GET is shown to benefit some, for others it is essentially considered just "cruel". A host of alternative treatments, some of which may be described as holistic or naturopathic or similar, naturally also exist, such as cryogenic, floatation and oxygen therapies, to name just a few. It is not the intention or place of the present article to compare, critique or scientifically review such treatments. It will simply be stated that, at least anecdotally, some such treatments seem to bring relief to some individuals (which is a positive outcome for those lucky enough to find any relief), but certainly most do not consider these treatments to be CFS cures or long-term major alleviators for the majority.

Contemporary scientific scrutiny into how COVID-19 can damage the brain [13,16,17], and suggesting that the virus' fatigue and adverse neurological effects (such as loss of smell and taste, altered mental states that can lead to the development of psychoses, and brain shrinkage in regions essential for processing memory, cognition and emotion) are indeed due to some hyperimmune response with neuroinflammation, does however offer many CFS sufferers new hope. Viz., hope that as a result of such scrutiny highly effective treatments (e.g., neural rewiring therapies [16]) and eventual cure await, even with the caveat of caution around some uncertain degree of overlap between COVID and non-COVID CFS.

1.5 ARTICLE PERSPECTIVE AND SCOPE

The present article's title upon first glance likely appears incongruous. However, while some delight was taken in choosing this "humorous-to-a-physicist" title, the article is journalistically serious and does not make light of CFS. Rather, in addition to the above CFS overview, the article reflects upon a presented clinical Case Study of a seemingly recovering CFS sufferer to form a justified CFS hypothesis for future testing.

The to-be-formed hypothesis follows from the unique neuro-perspectives of [18], which explore central nervous system impulse encoding revelations via a new approach to high-order electroencephalogram (EEG) phase analysis. Given that CFS has a neurological component, can these new perspectives be applied to the area of CFS, and in particular to the to-be-presented Case Study of recovery? While this tangent might seem a long bow to draw, perhaps a fresh CFS perspective is just what is currently needed. Despite the quantum mechanical aspects to come and references [18] and [19], the latter on a discrete oscillator phase noise effect applied within phase-shift keying radiofrequency (RF) digital signal modulation, being recommended prior readings for those with a biomedical engineering or similar background, no such specialist backgrounds are assumed for readers.

In brief, the present article represents academic (science and medicine) journalism that is hopefully considered high-interest, and shares via Case Study the clinical/medical results, collated over several years, for a scientifically dependent individual. The eventually formed hypothesis is intended for testing within a future formalised study, and so presently may be countered by alternative explanatory hypotheses, such as placebo and simple recovery coincidence, which are also identified.

2. CLINICAL CASE STUDY

2.1 GENERAL

The 29 year clinical Case Study (many sufferers of CFS have been living with the illness for over 20 or 30 years [4]) to be shared is that of my own, from CFS onset at 25 years of age to a recovery road at 54 years of age. While journalism (academic or otherwise) in which an Author has a vested interest is not uncommon, and indeed can be beneficial due to the experience and passion that the Author carries (CFS sufferers are considered experts in their own illness and experiences [4]), this declared interest is the reason independence is waived in Subsection 1.5. Despite this declaration, the quantitative and verifiable clinical/medical results to follow will be compelling to some and are presented in the belief that any road-to-recovery story and subsequently formed new hypothesis will always be of interest to CFS sufferers since, like myself, they will have "tried everything" to overcome the illness. However, until the new hypothesis is tested within controlled studies, all interested CFS sufferers are encouraged to retain a degree of healthy scepticism given the existence of other explanatory hypotheses.

A final dependence note is that the Case Study of this Section, and the treatment approach of a later Section, should not be considered "self-experimentation" or formal research (the latter being a standard to which qualification is not sought), but merely a shared chronology of clinical/medical results and details of a particularly desperate effort to return to good health during an individual's CFS journey. However, even if a self-experimentation label was applied, this should not necessarily bring discard given that respected precedents exist for academic journalism centred around the Author or Commentator as test subject. For example, a popular British Broadcasting Corporation (BBC) production on sleep [20] involves experimentation on the presenter (a physician and multiaward-winning medicine/science journalist) who, in another BBC (series) production [21], explores and in some cases celebrates historical and modern day self-experimenters in medicine. Well-known examples from the series include the intentional consumption of *Helicobacter pylori* (stomach ulcer) bacterium in 1984 with eventual awarding of a Nobel Prize in 2005 (to cut a long story short), and a controversial physician now regarded as being ahead of his time in the 1950s for nutrition research into the importance of essential Omega 3 fatty acids for heart and brain health. The celebrated physician of the latter example in 1979 undertook a 100 day extreme Inuit diet with weekly self-cutting to measure personal bleed times, and within a 1956 letter [22] to the Editor of the *Lancet* writes:

> *"your readers having stereotyped minds should stop reading at this point", Dr Hugh M Sinclair FCRP.*

The present article similarly encourages open-mindedness in regards to quantum findings for a Case Study where the person of clinical focus and presenter are one in the same.

2.2 PRE CFS ONSET

Before the onset of CFS I fell into a common (but not the only) CFS demographic of a fit and motivated young adult from a professional career background, generally making the most of every available minute of the day. In early 1993 I left my professional position and moved to Townsville (in tropical North Queensland) to undertake further postgraduate studies. At the time I had no awareness of viruses such as Ross River Fever and, taking no precautions, allowed myself to be exposed to many mosquito bites (e.g., at social student functions such as evening BBQs). Unsurprisingly, in short time I developed Ross River Fever[1] which was a clear "quantum trigger" for my CFS onset.

2.3 CFS SYMPTOMS

As per the imagery invoked by the previous *quantum trigger* descriptor, the onset of CFS symptoms at 25 years of age was immediate rather than gradual (immediate or gradual onset are both commonly reported in CFS). After an initial acute period of severe symptoms, the long-term symptoms experienced aligned with those previously cited in Subsection 1.1 as classic characteristics of CFS, as well as with several secondary characteristics associated with CFS.

In the earliest years I sought consultation from several physicians but without understanding as per the introductory

---

[1] Barmah Forest virus may also have been contracted around this time since positive antibody test results for this virus were identified some years after Ross River Fever infection confirmation. However, simultaneous status for these mosquito-borne viral infections cannot be stated with certainty.

statistic of Subsection 1.1, and from naturopathic-type clinicians. I recall on one early occasion (within the first 12 months of illness) having to be insistent with a reluctant general physician as to there having to be something wrong due to the severity of fatigue, and the need for a blood test. From 2008 I have also received intermittent consultations (approximately every 18 months) from a CFS specialist physician in South Brisbane. Ultimately these interventions brought no symptom relief, despite the appreciated efforts of the latter-mentioned specialist.

Because I was never permanently housebound and was able to maintain a career and moderate level of fitness (CFS can manifest in varying ways), CFS understanding by some was difficult. Certainly, many other CFS sufferers and sufferers of other medical conditions have faced significantly greater health challenges than myself, and so appreciation of my relative good fortune is not lost. Nonetheless, it would be wrong to dismiss the detrimental impact that CFS has on the lives of millions who suffer from CFS to a similar extent (i.e., not to the extent of being housebound), since a significant degree of debilitation is still experienced, leaving such sufferers feeling continually "weighted down" and as if they have ran a marathon after pushing through each and every day.

The long-term authenticity and severity of my condition is supported by the clinical/medical results shared within the following Subsections.

2.4 SELECT CLINICAL/MEDICAL RESULTS

Subsections 2.4.1 to 2.4.4 give a glimpse of the copious medical testing undertaken over the years to which all CFS sufferers can relate (many other tests have been undertaken but are not included here due mostly to their negative finding, or findings nonessential to the shared CFS story). Urine and gut analyses of the first two of these Subsections naturally will have advanced since their time of reporting in 1998, however the results are still informative.

2.4.1 URINE ANALYSIS, UNIVERSITY OF NEWCASTLE, AUSTRALIA, 1998

The following abridged results are extracted from a urine analysis report prepared by the Department of Biological Sciences, University of Newcastle, Australia, August 1998 (sample ID 4114, Entry 4228) within a CFS research program (with commercial arm) and associated support network that are no longer in existence. The urine analysis especially examines amino and organic acid metabolic disturbances (amino acids being the building blocks of proteins).

A summarising urine excretion profile of particular interest from the above report is given in figure 1 and includes diagnostic outcomes such as a 10 rating (on a 0 to 10 scale) for myofibrillar catabolism, and an above 8 rating for one particular fatigue classification. These indicating results for the first time (five years after CFS onset) brought hope and a certain degree of self-assurance and vindication that what was being experienced was not some "yuppy flu" or state of mind to be dismissed. Ratings of 10 and >8 were certainly subjectively consistent with my daily feeling of fatigue for 29 years. It is unfortunate that these CFS analysis services, that were arguably ahead of their time, were discontinued rather than further developed, however this discontinuation no doubt reflects the many complex facets of CFS.

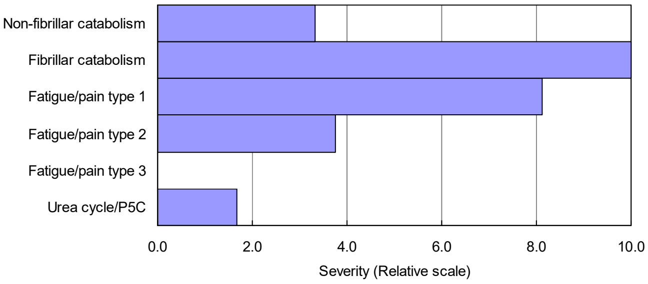

FIGURE 1. Urine excretion profile, with relative 0 to 10 unit scale, consistent with amino acid metabolism disturbances in subjects presenting with persistent pain or fatigue (graphic recreated from original report identified in-text).

The full University of Newcastle report also rates the excretion levels of urine constituents in relative percentage terms, with percentage values simply classified as low, average or high (no doubt to aid readability by the patient). Table 1 gives such values for select (4 out of 28) constituents of interest, with average population values bracketed for comparison (no population percentile ranges or standard deviations are quoted within the original report):

Table 1. Levels in relative percentage terms of select urine constituents, with bracketed values representing expected population averages.

Constituent	Low	High
Citric acid		11.69 (0.74)
Succinic acid	0.34 (1.37)	
3-Methyl-histidine		10.03 (1.33)
Lysine		8.27 (2.34)

According to the original University of Newcastle report, the relatively low and high excretion values for succinic and citric acids respectively, as seen in table 1, are together characteristic of CFS/pain and may be representative of disturbances in the Krebs cycle (high citric acid excretion levels, here approximately 16 times the population average, may remove divalent cations of elements such as magnesium, Mg). Note that from this point chemical symbols only are used to introduce elements within text. Note also that the Krebs cycle, alternatively known as the tricarboxylic acid (TCA) or citric acid cycle, is further briefly addressed within Section 3.

Also within table 1, 3-Methyl-histidine (3MH), or at least its analogue histidine, is an amino acid present in actin and myosin such that approximately 90% of human 3MH is contained within skeletal muscle[2]. Table 1 shows high 3MH excretion which can indicate muscle protein turnover or catabolic breakdown of myofibrillar protein (e.g., in the instance of muscle injury) [23,24]. The high lysine excretion indicated in table 1 associates with the "type 1" fatigue of figure 1.

The above-noted amino acid metabolic disturbances, including myofibrillar protein breakdown, along with evidence of Krebs cycle disturbances, will be revisited as the present article continues to build towards its eventual hypothesis.

2.4.2 GUT ANALYSIS, UNIVERSITY OF NEWCASTLE, AUSTRALIA, 1998

In parallel with the above urine analysis, a gut health analysis was also undertaken through the University of Newcastle, the reporting for which states that alterations in excreted lipid composition and aerobic/anaerobic microflora (microbiota) distribution occur in CFS. Such occurrences are perhaps generally unsurprising, given the known association between good gut health and a robust immune system, as well as the association between CFS and immunological dysfunction.

The majority of the University of Newcastle's gut analysis report will not be presented here (due more to being non-essential to the eventually drawn hypothesis), other than to briefly mention one of the several out of balance findings. This finding being coprostanol lipid (1 of 27 reported lipids) excretion being approximately 150 times lower than the population average with a coprostanol-to-cholesterol ratio of only 0.17%. This ratio value is particularly interesting and potentially telling of a compromised system. For most, the efficiency of converting cholesterol into coprostanol (via microflora metabolism) is generally high, such that minority "low converters" (ratios of < 0.5%) account for 5 to 30% of the adult population [25]. That recent study further highlights that low conversion efficiency may signify a higher risk of disease and loss of good health (though the adverse association is still not extensively assessed).

2.4.3 OLIGO SCAN (2021)

The Oligo scan (marketed as Oligoscan within industry) reports on mineral, vitamin and heavy metal levels in body tissue including peripheral blood vessels, and is based on rapid four-point spectroscopic analysis of the hand. The scan is relatively new to Australia where it is becoming increasingly popular within naturopathic and holistic practices, some of which also offer conventional medical services. The scan is intended as an indicating tool for trained clinicians who naturally would complement any indications with other relevant whole-picture clinical evidence. The diagnostic wherewithal of the scan's overall report is arguably not fully accepted (or necessarily claimed) from an academic research perspective, and the present article commences with a neutral position as to any such capability.

Within the Oligo scan's mineral test report (the first main component of the overall report), the levels of 21 elements are generated, as per figure 2a which displays my results from a January 19, 2021 scan performed by a Brisbane-based clinic (commercial provider). Of the 21 elements analysed, P was revealed as the only element at a low minus or "red" level. Figure 2b shows a consistent P finding within a scan independently repeated approximately seven months later on August 16, 2021 by a separate Brisbane-based clinic.

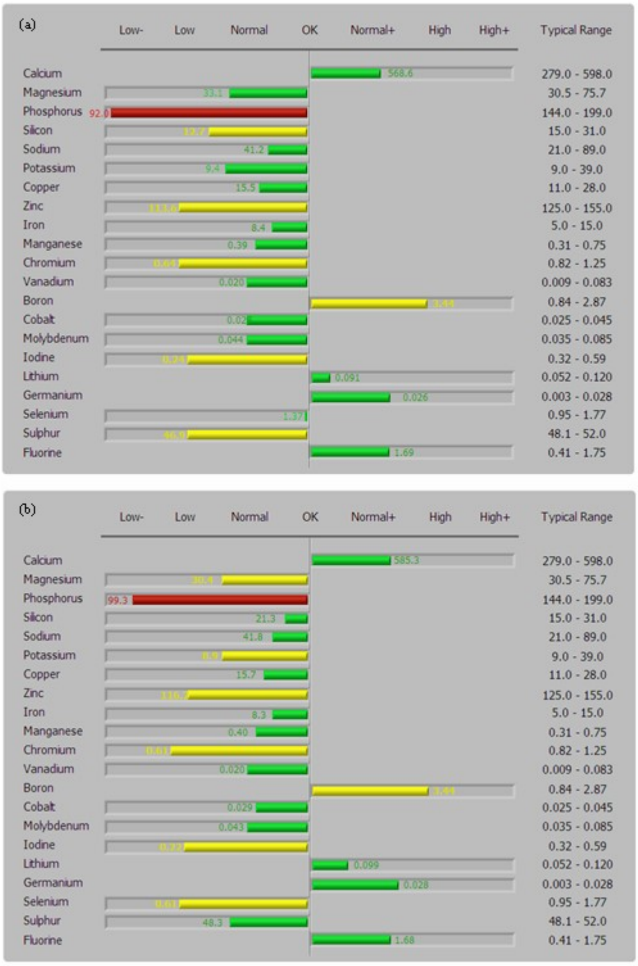

FIGURE 2. **Oilgo scan report (first main component of) which displays body tissue levels of 21 specified elements, as independently obtained on (a) January 19, 2021 and (b) August 16, 2021. Graphics have been regenerated from the original clinical reports which do not specify the units of elemental levels.**

---

[2] Myofilaments are organised into bundles called myofibrils and largely consist of the *contractile* proteins actin (thin filaments) and myosin (thick filaments). However, other important constituent proteins exist such as for thin filaments the *regulating* proteins tropomyosin and attached troponin (complex). Tropomyosin interacts with actin, myosin and troponin to regulate muscle contraction and relaxation (i.e., controls filament sliding), a process for which Ca^{++} binding to troponin in response to action potential-induced Ca^{++} concentration changes is key.

The scan results of figure 2 were obtained under a subjectively considered balanced diet that routinely included foods relatively high in P. Note that while over the years I have tried taking health supplements, under health or medical practitioner guidance, I have never experienced a perceived beneficial CFS alleviatory effect from such supplements (which I can have intolerance towards, including instances of fatigue exacerbation which does not pass with persistence). Hence, no supplements were taken in the months leading up to these Oligo scans. Indeed, over the years I have formed the *unqualified* opinion that CFS is very complex (universally accepted as being the case) and so for many, or certainly in my case, a prescribed supplemental remedial approach unfortunately does not provide the "simple answer" (else for example, such remedies would have already been identified by the medical support teams of high-profile CFS sufferers in fields such as professional sport, and by the many CFS studies across the world-wide tertiary landscape). Naturally, taking health supplements under the broad umbrella of fatigue is beneficial and even essential to many, including some other CFS sufferers, and in no way does the present article discourage their use (as always, individual effects vary and decisions on the use of such supplements must always be made under the guidance of a qualified health practitioner).

As indicated above, there is some reservation about the scientific efficacy of the Oligo scan for academic research (e.g., as raised within academic on-line discussion forums), and indeed taking a wait-and-see approach until supporting (or otherwise) scientific evidence grows is probably prudent for such formalised research. However, one cannot help but be impressed by the consistency between figures 2a and 2b, the scans for which were independently undertaken seven months apart at different clinics unaware of the other clinic's scan (i.e., consistencies such as elements P and B markedly displaying the lowest and highest levels respectively, as well as several easily identified others).

The consistent low minus P result in figures 2a and 2b, for a well balanced diet relatively high in P, is naturally of interest for a sufferer of CFS, given that P plays a critical role within body energetics (see Section 3). In this regard it is noteworthy that over the years spanning my CFS, conventional blood tests have always shown blood P levels to be within a normal range (perhaps representative of blood levels not always being indicative of cellular tissue levels for some elements [26]). As per the University of Newcastle findings of Subsection 2.4.1, this Oligo scan-based P finding will be revisited as the present article continues to build towards its eventual hypothesis.

2.4.4 MISCELLANEOUS CONVENTIONAL BLOOD PATHOLOGY

The following blood pathology[3], with results outside of typical (bracketed) ranges, have been reported by Queensland Medical Laboratories at the request of the aforementioned CFS specialist physician:

Ferritin (Fe-storing protein)

- Nov 2015, Dec 2015, Jan 2020
- 354, 327, 349 (30 – 320) $\mu g \cdot L^{-1}$ respectively
- Mild elevation with no supplement intake
- Dec 2015 PCR test for hereditary haemochromatosis gene negative (C282Y, H63D, S65C mutations not detected)

Serum Vitamin D (1,25-dihydroxy vitamin D)

- July 2008
- 156 (40 – 150) $pmol \cdot L^{-1}$
- Mild elevation with no supplement intake and quite limited sun exposure.

3. POSSIBLE SIGNIFICANCE OF VERY LOW PHOSPHOROUS – "ENERGETICS 101"

Amidst all of the scientific debate, uncertainty, and points of view in regards to CFS, ultimately what is undeniable is the simple perspective that a person suffering CFS is somehow deficient in energy or the ability to effectively utilise available energy. When postulating a new CFS hypothesis, it is therefore reasonable to consider the origins of biological energy production. That is, all students of science are familiar with the notion of energy production from respiration, which involves the release of chemical energies from foods such as glucose. However, at its core this fundamental and well understood process involves P, especially in the form of ATP. For example, within both the aerobic and anaerobic equations of respiration, high-energy ATP is synthesised from adenosine diphosphate (ADP), with the synthesised ATP providing for cellular-level metabolic energy requirements (since stored chemical energy is then available via ATP splitting into ADP plus a cleaved inorganic P) [27].

In the case of skeletal muscle, ATP-sourced mechanical energy provides for the cross-bridge interactions, between actin and myosin filaments, that result in the production of muscular contractile force. The resynthesis of ATP from ADP and inorganic phosphate continually occurs within muscle cells via three main energy systems, namely the *Immediate*, *Anaerobic (Lactic Acid)* and *Aerobic (Oxidative)* systems. The latter Aerobic system provides a relatively slow rate of ATP production for endurance activities. Fats (fatty acids), proteins (amino acids) and carbohydrates (glycogen and glucose) can all be aerobically metabolised to

---

[3] Laboratory reference numbers in the order of listing are: 15-71216303-ISM-0, 15-72141582-ISM-0, 20-71814636-ISM-0, 15-69998378-HFE-0, and 08-7028292-VDD-0.

produce ATP (with the metabolic pathways involving the Krebs cycle)[4]. Aerobic ATP production occurs in the mitochondria, and so not surprisingly mitochondrial dysfunction (e.g., lowered ATP production, *impaired oxidative phosphorylation* and mitochondrial damage) is found in CFS [11].

As well as being a major component of ATP and thus arguably being the most important element in terms of biological energy production as summarised above, P is also an important component of cell membranes and ribonucleic acid (RNA) which is synthesised by DNA in cells. So when a Case Study of a CFS sufferer of almost 30 years repeatedly returns a consistent 21 element body mineral analysis test result, whereby the only element in the low minus or red region is P (as presented within Subsection 2.4.3), and impaired oxidative phosphorylation is associated with CFS [11], the result should reasonably be considered CFS-indicative, especially when supported by other long-term diagnostic findings which include the maximum "10" and ">8" urine analysis ratings from the University of Newcastle analysis. Accordingly, the present article is building towards a CFS mechanistic (plus treatment) hypothesis involving inadequate metabolism of P (and symbiotically associated elements), but also with a quantum mechanical basis as indicated by the article's title. Before arriving at this final hypothesis, further hypothesis framework components are required (Sections 4 and 5).

4. NEW HIGH-ORDER PHASE ANALYSIS OF THE EEG AND ITS QUANTISED FINDINGS

Before reading this Section, those without a biomedical engineering or similarly mathematically-underpinned background are directed to introductory signal processing texts that address the topic of frequency domain, particularly in relation to the electroencephalogram (EEG) or "brain wave" analysis.

4.1 OVERVIEW OF NEW ANALYSIS TECHNIQUE

A promising EEG analysis technique [18] commences with the double application of high resolution Fourier analysis, whereby the second Fourier transformation is applied to an amplitude versus frequency spectrum of a conventional transformation. This technique generates new harmonics spanning the conventional frequency spectrum, in turn allowing profiles of new harmonic phase, ϕ, to be constructed over an effective time-domain, t' (i.e., the double application reverts to some quasi time-domain). The ϕ versus t' behaviour of such profiles generally displays strong linearity for EEGs collected during deep sleep. However, for awake and other stages of sleep, such profiles display many structured ϕ changes. These discrete ϕ changes, or $\Delta\phi$, are found to cluster, with influential $\Delta\phi$ clustering categorised by [18] into ten "Families". Eight of the Families are considered primary and display $\Delta\phi$ clustering about $\Delta\phi_c = 5^\circ$, 10°, 20°, 30°, 50°, 90°, 180° 270°. The remaining two Families are considered secondary and display $\Delta\phi$ clustering about $\Delta\phi_c = 135^\circ$ and 220°. The typical chaotic-like nature of conventional first-order EEG harmonic phase analysis is in stark contrast to the highly structured phase behaviour of the described new harmonics.

4.2 MORE SPECIFIC PHASE STRUCTURE FINDINGS OF NEW TECHNIQUE

In many instances within Family $\Delta\phi$ clusterings, the separations between $\Delta\phi$ values are also highly structured and may be written in terms of integer, or fractional-integer, multiples of a proposed quantum increment value, α, with ⅓ and ¼ but especially ½ being fractional examples. A *transition diagram* that graphically displays these $\Delta\phi$ separation multiplicities is given in [18] for each Family, along with the mean α value, $\overline{\alpha}_{\Delta\phi}$, for each Family.

Interestingly, several paired combinations of Family $\overline{\alpha}_{\Delta\phi}$ values form ratios that align with simple common fractions (e.g., 2/3, 1/5, 4/5) to high degrees of precision and, as also briefly raised within [18], intriguing linkage can also be made between such formed ratios and ratios of the culturally/historically significant pentatonic music scale and ratios utilised within the communication systems of intelligent mammals such as sperm whales.

Family $\overline{\alpha}_{\Delta\phi}$ versus $\Delta\phi_c$ values display strong parabolic functionality ($r = 0.99998$, $p < 0.001$, 95% CI) given by:

$$\overline{\alpha}_{\Delta\phi} = (1.9772 \pm 0.0049) \times 10^{-4}\,\Delta\phi_c^2 - (9.990 \pm 0.097) \times 10^{-3}\,\Delta\phi_c + (3.002 \pm 0.021) \times 10^{-1}, \tag{1}$$

and as graphically shown by figure 3.

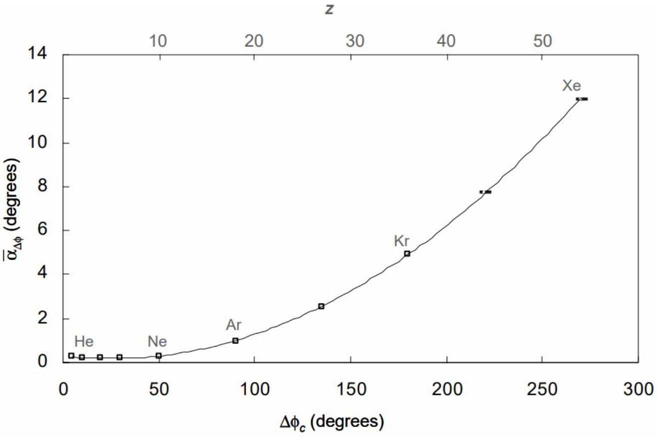

FIGURE 3. Family $\overline{\alpha}_{\Delta\phi}$ versus $\Delta\phi_c$ as presented in [18]. The secondary *x*-axis applies the linear transformation $\Delta\phi_c/5 \rightarrow z$, with subsequent annotations identifying *z* values for (five of eight) primary Family members that coincide with the atomic numbers of indicated noble (rare) gases. Error bars (95% CI) are resolvable (just) for the two right-most points only.

---

[4] Carbohydrates can additionally be anaerobically metabolised within the Krebs cycle.

Within the figure 3 parabolic function, the high precision y-value of the turning point (minimum) corresponds to $\overline{\alpha}_{\min} = 0.174019 \pm 0.000010^{\circ}$, and is representative of a seemingly universal quantum increment value that spans across Families. Viz., several occurrences of separations between $\Delta\phi$ values being structured in terms of $\alpha_{\min}$ multiples are identified within the $\Delta\phi$ clusterings (transition diagrams) of all Families [18]. The secondary x-axis and annotations of figure 3 are explained within Subsection 4.3.

4.3 QUANTUM MECHANICAL ASPECTS OF PHASE STRUCTURE FINDINGS

The above-described structuring of the separations between $\Delta\phi$ values in terms of $\overline{\alpha}_{\Delta\phi}$ multiples is quantum-like, in that any preference for *half-* or *full-integer* multiplicity is consistent with various forms of quantisation observed in many well-known quantum systems. This identified characteristic, together with other identified quantum-like characteristics including parabolic functionality which is present in various forms within several of the well-known quantum systems, led to the suggestion in [18] of a quantum mechanical governance to neural impulse generation. Hence, within [18] it was concluded that the EEG is encoded by quantised phase transitions between the newly-identified harmonics, allowing for powerful phase-shift keying impulse encoding complexity with high transitional degrees-of-freedom.

A preliminary but nonetheless intriguing offshoot quantisation finding in [18] involves the transformation of primary Family $\Delta\phi_c$ values. Viz., linear mapping to a proposed dimensionless index, z, via the transformation $\Delta\phi_c/5 \rightarrow z$ (as per the secondary x-axis of figure 3), respectively yields for the eight ascending primary Family members $z = 1, 2^*, 4, 6, 10^*, 18^*, 36^*$ and 54^*, where the asterisked z values equate to the atomic numbers, Z, of the noble (rare) gas elements of He ($1s^2$), Ne ($2p^6$), Ar ($3p^6$), Kr ($4p^6$), and Xe ($5p^6$) which are annotated within figure 3 (bracketed notation here gives the filling of the outer-most subshell for indicated elements). Following the same atomic labelling, the remaining primary Family $z = 1, 4, 6$ values equate to the elements of H ($1s^1$), Be ($2s^2$), and C ($2p^2$). It was subsequently also concluded in [18] that this mapping is possibly suggestive of neuro-quantum processes involving elementally-proportional optimal quantum states.

Another linear mapping outcome of intrigue applies to the turning point of the figure 3 parabola (recall that its high precision y-value is representative of a seemingly universal quantum increment value, $\alpha_{\min}$, that spans across Families). The corresponding x-turning point value, $\Delta\phi_{\min} \approx 25^{\circ}$, upon transformation yields $z \approx 5$ (or 5.07 ± 0.05 and see [18] for the reason $\alpha_{\min}$ is known to higher precision than $\Delta\phi_{\min}$), and so elemental labelling of $\approx$B ($2p^1$). Contextual interest in B corresponding to the governing parabola's most important point, arises from the consistently high B finding in Subsection 2.4.3, and B's significance not only within biological health, but also within geology and astrobiology on the basis of being a likely necessary component for the formation of Earth-like planetary life due to a RNA synthesis role [28].

5. THE MODERN ETHER

The present article is gradually building to a later justified hypothesis considering the possibility that for a minority of people and in certain (e.g., compromised) circumstances, constant exposure to a "modern-day ether" may compete with the complex phase oscillations and encodings of the neural processes of Section 4, and that this competition may not always be completely tolerated. Relevant background to the modern-day ether is thus given below.

5.1 PHILOSOPHICAL UNDERPINNING FOR POSSIBLE BIOLOGICAL INTERACTION

It is indisputable that radiofrequency (RF) electromagnetic waves can influence the human body, since MRI is based on the resonant absorption of RF energy by billions of protons in the body, especially protons belonging to the hydrogen atoms of water molecules. This resonant energy absorption is facilitated by proton precession being undertaken at the same frequency as that of the applied RF waves, with the precession brought about by an applied strong magnetic field that is synonymous with MRI. The resonant RF energy absorption excites the protons to a higher energy state and synchronises the protons' phases of precession (which is "MRI 101"). That is not to say that such RF energy absorption examples are biologically harmful to humans, on the contrary MRI is known for its safety. At the other end of the spectrum, United States officials believe that the deliberate recent targeting of some diplomats via a high-powered electromagnetic weapon, likely operating towards the microwave end of the RF range, has affected their neurological health to the point of brain injury. Clearly then, RF waves can influence the human body, usually in benign ways but also up to seriously adverse ways.

For the less extreme case of MRI RF waves, and more generally RF communications across the board within radio (AM/FM/digital)[5], cell phone and television broadcasting, the wavelengths of RF waves are physically of the orders of meters to centimeters (even extending to millimeters for new 5G technology). For example, an FM radio broadcast at 100 MHz corresponds to a RF wavelength of around 3 m. Hence, invisible oscillating waves of electromagnetic energy, on a macroscopic scale of physical relevance (i.e., with dimensions relatable to the every-day human macroscopic world), form part of the "modern RF ether" (from this point referred to as the modern ether) that is all around us and which permeates our beings. Again, this modern ether, which has been ever-"thickening" since

---

[5] The acronyms AM and FM respectively represent amplitude and frequency modulation.

Marconi's development of the wireless telegraph and invention of the radio in the 1890s, should be considered relatively biologically safe, and the research-grounded reports of professional bodies (such as the World Health Organization, Australian Radiation Protection and Nuclear Safety Agency, and International Commission for Non-ionising Radiation Protection) should rightly form the basis for society's position on RF exposure and safety. Of course an individual choosing to minimise and/or avoid unnecessary exposure to RF emissions is also completely reasonable.

The present article takes with seriousness its essential position that any writing under the banner of possible RF electromagnetic interactions with the human body needs to be measured and not alarmist or sensationalised; the article will not be suggesting that every-day RF exposure is routinely biologically damaging and, as per the above commentary, advocates a default to the stated governing authorities for society's guidance on safety surrounding telecommunication issues. Nonetheless, humans are electromagnetic beings in the sense that we generate low level electromagnetic emissions from the electrical activity of the brain and related neurophysiological processes, and the above essential position does not exclude reasoned discussion on the possibility of some form of interaction between the human body and the modern ether, even if interaction is just on some inert level like in MRI (with recognition that biological interactions within the MRI analogy are facilitated by strong magnetic fields which are not present in every-day life). Similarly, the possibility that for a minority and in certain compromised circumstances, constant exposure to the modern ether may compete with the complex neural phase oscillations and encodings of Section 4, and that the competition may not always be completely tolerated, should not be discounted. An aspect of RF telecommunications considered particularly relevant for later hypothesis justification follows.

5.2 INTRODUCTORY THEORY OF STANDARD FREQUENCY MODULATION IN TELECOMMUNICATION

Within standard FM theory, modulating a carrier RF signal's frequency by an amount proportional to the amplitude of the primary signal (such as an analog voice recording) to be broadcasted, also effectively modulates the phase of the carrier RF signal. In addition, the modulation of phase can produce a noise effect in the frequency-domain [19] and phase oscillations can be expected within the (secondary) harmonics of this domain. Thus, even with deliberate phase-shift keying schemes used within modern digital RF communications placed aside, standard RF communications are rife with phase modulations. An overview of standard FM theory that aids in the understanding and quantification of its main inherent phase modulations is given below.

An FM signal of instantaneous amplitude, e, and which is modulated sinusoidally (artificial construct for demonstration purposes), can be written as:

$$e = E\sin\left(2\pi\left[f_c + \Delta F\sin(2\pi ft)\right]t\right), \tag{2a}$$

where E is the maximum amplitude of the carrier wave, f_c is the unmodulated carrier wave's frequency (e.g., 100 MHz), ΔF is the peak deviation or swing of the carrier frequency away from f_c, f is the modulation frequency for the example case of simple sinusoidal modulation, and t is time (in practice, f_c is modulated in a more complex manner representative of the irregular modulations within speech, music, or other waveform for broadcast).

Routine trigonometric manoeuvring allows (2a) to be re-expressed as:

$$e = E\sin\left(2\pi f_c t + \varphi\right), \tag{2b}$$

wherein $\varphi = 2\pi\Delta Ft\sin\left(2\pi ft\right)$ represents a modulation in phase (i.e., f_c modulation effectively produces a phase modulation for a constant f_c).

Although the modulations of real-life FM transmissions are more complex than in (2b), real-life modulations nonetheless occur between the discrete limits of $\pm\Delta F$ and so have a partially discrete nature despite their analog origins. Later consideration with quantified justification (see Subsection 6.3), will therefore be given to the possibility of whether the above phase modulations have the capacity to resonantly influence the complex high-order phase modulations upon which the central nervous system's electrical impulse encoding appears to be based (as per [18] and as summarised in Section 4).

6. COMMENCING POSTULATE AND ENSUING HYPOTHESIS

The framework components of a to-be-formed hypothesis have now been established. This Section links these components to provide a justified hypothesis for a CFS mechanism, targeted action upon which (as per Section 7) has, for the presented Case Study, recently coincided with seemed recovery initiation (or at least quantifiable relief) 29 years after CFS onset.

6.1 POSTULATE

A commencing postulate for the encompassing hypothesis is as follows:

Postulate

For the $\Delta\phi_c$ within high-order phase encoding of neural electrical impulses, linear mapping via the transformation $\Delta\phi_c/5 \rightarrow z \rightarrow Z$ to certain elements such as noble gases (suggestive of elementally-proportional quantised neural processes), can be extended to other elements. Extension to such other elements involves the reverse mapping of Z to $\Delta\phi_c$, which also allows the further prediction of corresponding $\overline{\alpha}_{\Delta\phi}$ values via the interpolation of (1).

6.2 EARLY QUANTUM INSIGHTS ARISING FROM POSTULATE

The following early quantum insights for now simply set the scene for results to follow and are somewhat speculative. The primary post-treatment quantum results presented later in Subsection 8.1 do not rely on the element linkages made here (but rather just on the overall sense as reflected in the hypothesis of Subsection 6.3).

The Case Study's Oligo scan results (figure 2), showing P and B as consistently, markedly, and unusually, having the respective lowest and highest relative levels of 21 reported elements within the scans' mineral test report, leads one to consider, in an exploratory manner, the places held by these two elements within the neural phase encoding parabola of figure 3. Potential quantum remarkableness lies with the fact that a bodily disposition presents with a P-associated "state" (critical for energy production) having the lowest relative "occupancy" of all 21 elements, and a B-associated state having the highest relative occupancy, with B also associated with the parabola minimum (of figure 3) which could be envisaged as some neural quantum state of minimum energy. In which case, it could be said that the lowest energy state has the highest relative occupancy for the CFS sufferer, and so perhaps suggestive of some kind of *excitational transition or therapeutic deliverance to a higher energy state being required for a return to good health*.

Reversal of the $\Delta\phi_c/5 \rightarrow z \rightarrow Z$ transformation (reverse mapping) for P ($Z = 15$) yields a predicted $\Delta\phi_c = 75^\circ$, with (1) in turn predicting a corresponding $\overline{\alpha}_{\Delta\phi} = 0.663 \pm 0.012^\circ$ (95% CI), which may also be expressed as $\overline{\alpha}_{\Delta\phi} = 2/3^\circ$ to within 0.5% alignment. Predicted $\Delta\phi_c$ and $\overline{\alpha}_{\Delta\phi}$ values for an individual element from this point will carry a subscript indicative of the element (e.g., $\Delta\phi_P = 75^\circ$ and $\overline{\alpha}_P = 0.663 \pm 0.012^\circ$ for P), which is also appropriate since $\Delta\phi$ clustering, as suggested by the original "*c*" subscript and explored in [18], is not a present focus. Also, while $\overline{\alpha}_{\Delta\phi}$ values are not further addressed within this early quantum insights Subsection, they are similarly calculated and presented in a unified manner for other elements later.

Following the same reverse mapping modus operandi for B gives $\Delta\phi_B = 25^\circ$, and a subsequent $\Delta\phi_B{:}\Delta\phi_P$ ratio of 1:3 (which is naturally reflected by the elements' Z values). In isolation this ratio is arguably unremarkable (although in the context of [18] and its reported ratio-based governance of neural impulse encoding for which 1:3 is a key ratio, perhaps the finding is singularly interesting for a CFS Case Study in which the two elements markedly stand out). Regardless, remarkable status appears reinstated when other elements of interest from the Oligo scan results, namely Zn and Ca, are similarly included alongside P and B. The bases of collective consideration for this quartet of elements within an early quantum insights exploration are summarised by table 2:

Table 2. Quartet element selection bases for the specified reverse mapping analysis leading to possible quantum insights.

Element	Bases for quartet element selection
P	• Consistently, markedly and unusually displays the *lowest* relative Oligo scan level out of 21 considered elements. • Fundamental role in energy production (e.g., as the basis of ATP). • Second most abundant mineral by weight in the human body. • Present in every cell.
B	• Consistently, markedly and unusually displays the *highest* relative Oligo scan level out of 21 considered elements. • Likely necessary component for the formation of life due to a RNA synthesis role. • Associates with the parabola minimum in figure 3. • Arguably one of the least essential trace elements in terms of bodily function (though its "boring tag" is changing, having for example a known synergy with Ca).
Zn	• Consistently one of the lowest relative Oligo scan levels out of 21 considered elements. • Independently identified by clinical consultants as a primary deficiency to address following Oligo scans. • Essential immune system and wound healing roles (sometimes prescribed during viral recovery periods), and in general is quintessentially recognisable as essential for good health. • Second most abundant trace mineral after Fe in the human body. • A known synergy exists with P.
Ca	• Consistently one of the few Oligo scan levels in the normal plus range. • Most abundant mineral by weight in the human body due to skeletal mineralisation. • Key role in muscle contraction (see Subsection 2.4.1 footnote). • Key role in cardiac action potential generation and cardiac rhythm maintenance (and thus body clock homeostasis). • Key role in cellular signalling/communication [29]. • Quintessentially recognisable as essential for good health. • Known synergies exist with P, as well as with B.

The predicted $\Delta\phi$ values for P, B, Zn and Ca, when superimposed upon the governing parabola of neural phase encoding, yields figure 4. As graphically highlighted by figure 4, P, Ca and Zn all have associated $\Delta\phi$ values that are integer multiples of B's value (i.e., of the parabola minimum). Accordingly, the ratios $\Delta\phi_B{:}\Delta\phi_{Ca}$, $\Delta\phi_P{:}\Delta\phi_{Zn}$ and $\Delta\phi_B{:}\Delta\phi_{Zn}$ are 1:4, 1:2 and 1:6 respectively, with $\Delta\phi_B{:}\Delta\phi_P = 1{:}3$ previously identified. These findings may imply the presence of some possible quantum connectedness based on integer multiplicity and symmetry. Hence, for the CFS Case Study at hand for which it is suggested that a B-associated quantum neural state is being preferentially occupied over a P-associated quantum neural state, other preferential occupancies (e.g., Ca-associated quantum neural state) might also be indicated.

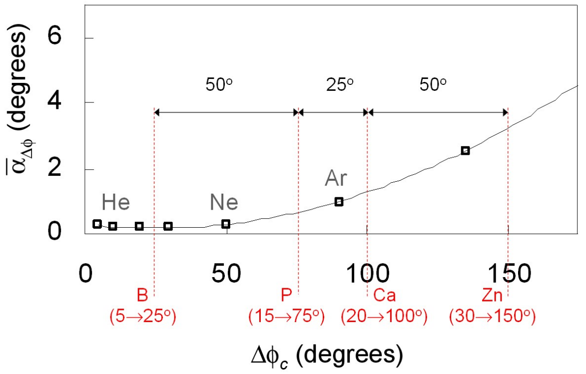

FIGURE 4. **$\Delta\phi$ ($\equiv \Delta\phi_c$) values predicted by reverse mapping for B, P, Ca and Zn, and considered as "quantum states" when superimposed upon the governing parabola of neural phase encoding (figure 3).**

From the above, ratios such as B:P, B:Zn, B:(P×Zn) and (B×Ca):(P×Zn), based on elemental levels from Oligo or other such scans, may be worthy to explore as possible personal clinical indicators during recovery from long-term (>20 years) CFS. Analysis of these ratios is given later in Subsection 8.2. The possibility of extension to other combinatory indicial personal ratios should not be excluded, while the appropriateness and sensitivity of such indices for shorter CFS durations (i.e., for some other individuals) is left for future consideration.

Finally for this early quantum insights exploration, the spacings of the so-called neural states in figure 4 are analogously mindful of quantum mirror symmetries associated with states of phenomena such as spin-up versus spin-down and matter versus antimatter, and also seemingly consistent with mirror symmetries identified in [18]. However, while Ca inclusion in the above analysis is justified by table 2, its inclusion may be considered convenient given its normal plus (green) level in figure 2. Hence, the mirror symmetry insight is especially tentative. Nonetheless, interest in the quantum-like forms surrounding figure 4 is not diminished if only P, B and Zn are retained, with 1:3:6 ratios and their subsequent symmetries remaining for corresponding $\Delta\phi$ values.

6.3 *HYPOTHESIS*

The present article's hypothesis can now be stated and is motivated by the question of: why for the CFS Case Study are the relative occupancies of quantum neural states seemingly "out of kilter". The hypothesis, as partially alluded to within Section 5, is as follows:

> *Hypothesis*
>
> For a minority of persons and in certain circumstances, constant exposure to the modern RF ether, which is becoming increasingly crowded, may compete with the complex phase oscillations and encodings of neural processes. This competition may not always be completely tolerated, especially (but not just) by those already in compromised states of well-being (e.g., recovering from a virus with neurological impact). More specifically, phase oscillations within the modern RF ether may correspond with element $\Delta\phi$ or $\overline{\alpha}_{\Delta\phi}$ values calculated in accordance with the commencing postulate. Removal of the described competition, combined with positive neural stimulation, might aid in illnesses such as CFS (e.g., via neural rewiring facilitation and activation of key element utilisation, within the confines of element availability).

Clearly, many over several decades have raised concerns over exposure to the modern ether (some in rather eccentric or extreme detrimental ways, and others in more measured ways), and the area of discussion is likely to remain controversial for some time. What is original about the present hypothesis is its ability for justification by quantified results that stem from its highly specific aspects. For now, justification commences with added specificity surrounding RF-neural interaction possibility, as given by Subsections 6.3.1 and 6.3.2. However, before visiting these Subsections it should be reemphasised that the present article is not alarmist about modern ether exposure and, as per Subsection 5.1, holds that society's exposure should follow the guidelines of stated governing authorities.

6.3.1 FM INTERACTION JUSTIFICATION: SPECIFIC

As per Subsection 5.2, in-practice modulation within FM transmissions is more complex than the simple artificial sinusoidal modulation of (2), and involves the carrier wave still swinging in and out of phase with f_c over multiple cycles, but in a more irregular manner. However, when further visualising a RF wavelength permeating the body at some instant, in-practice modulation remains relatively simple from the overall perspective of the carrier wave being modulated within the limits of $f_c \pm \Delta F$, since this represents an effective phase modulation of $\varphi_{eff} = \pm\Delta F/f_c$ fraction of a complete phase cycle (2π radians or 360°). Typical f_c values fall between 88 to 108 MHz for conventional FM radio (with bands above and below this range for television), and some typical ΔF values are 75, 50, 25, 5, 2 kHz. Thus, an example of $f_c = 100$ MHz, $\Delta F = 75$ kHz corresponds to $\varphi_{eff} = 0.27°$.

The above φ_{eff} value may be relevant since seven of the ten Families of neural phase encoding identified in [18] possess $\overline{\alpha}_{\Delta\phi}$ values in the same vicinity (i.e., between 0 and 1.0°), and it is easy to generate a host of other φ_{eff} values in this vicinity when considering other ΔF and f_c combinations (which also arise from other f_c stations spaced by 100 kHz or similar). Hence, while FM does not directly apply deliberate and specific phase encoding as found within modern digital communications that employ techniques such as phase-shift keying, the alignment between φ_{eff} and $\overline{\alpha}_{\Delta\phi}$ means that some resonant interaction may be possible.

6.3.2 FM INTERACTION JUSTIFICATION: GENERAL

Discrete Phase Noise Effect

As per the brief comment of Subsection 5.2, the phase modulation described by (2b) is expected to bring about a noise effect of discrete side lobes (ordinarily unwanted but digitally utilised in [19]) within a station's bandwidth, which can produce phase oscillations potentially capable of some form of neural phase interference.

Critical kHz Range

The fact that ΔF values are in the kHz range itself may raise the possibility of neural interaction, since the frequencies of music, speech, and audible sound in general, are also in the kHz range (up to ultrasound at 20 kHz). Viz., a multitude of modulations within the $f_c \pm \Delta F$ bandwidth (not the formal definition of bandwidth), and even "beat"-like phenomena between transmissions from different stations, will fall in the audible kHz range. Of course not being sound waves there is no direct audibility, but sound waves at these frequencies are anatomically and physiologically converted into biological electromagnetic signals that are representative of the frequencies, and so it is reasonable to consider the possibility of FM signals in the "critical kHz range" having occasional subtle indirect interaction ability. As previously stated, over the decades several have raised concerns over possible effects of the modern ether, and so the observation here likely overlaps with those of the past.

Lessons from Kindred Ocean Mammals

Within [18] it was revealed that some communication processes of sperm and beluga whales involve simple common fractions that were also identified within the complexities of high-order phase encodings of neural impulses within the human brain. And so it seems that humans have even more in common with such majestic creatures (e.g., than simply being highly intelligent mammals with sophisticated social structures), which as a generalisation will be unsurprising to many.

With the above commonality in mind, the reasons behind the heart-wrenching sight of large pods of these intelligent mammals beaching themselves largely remain a mystery, with the largest recorded beaching in modern history involving approximately 1000 whales upon the Chatham Islands, a New Zealand Territory in the Pacific Ocean, and occurring in 1918 (15 years after Marconi sent the first practical commercial radio message from Massachusetts to England). There are multiple believed reasons behind beachings and some of these are attributed to temporary corruption and confusion within the whales' internal navigation due to interference from electromagnetic field changes, including those brought about by solar flares. This evidence-based (at least in some cases) electromagnetic attribution is generally accepted without major controversy. Hence, a suggestion that the modern ether can affect humans, not at the same acutely obvious level but in some generally inert or less obvious way, should also remain a possibility amidst calm. After all, in the early years of CFS just a few decades ago, the condition was unfairly branded as "yuppy flu", suggesting modern lifestyle and environment, particularly a technological environment, were contributing factors.

The modern ether is such a complex and condensed amalgamation of so many encrypted signals that it would certainly be deafening, confusing and unbearable if we could actually "hear" the ether as constant background noise (indeed it would have to be many levels worse than being in a crowded room of several loud conversations). Luckily we cannot "hear" the modern ether in this way. However, given that in some respects we are electromagnetic beings, it is again reasonable to suggest that the human brain might possibly be sensitive, in the slightest of ways, to the modern ether (especially older brains without the same generative/compensatory ability of a young, developing brain).

7. "QUANTUM TREATMENT" APPROACH

Seemed recovery initiation for 29 year duration CFS coincided with the completion of an informal "quantum treatment" approach applied in two stages, as outlined below. Since the approach represents an individual's unqualified, self-directed undertaking, it requires refinement and testing within a future controlled formalised study in order to validate any attached claim or finding. Also, the reported recovery could alternatively be explained by coincidence, placebo, or individual responsiveness unhelpful to others (just as other alternative treatment approaches can be highly beneficial to some but not the majority). No attempt should be made to replicate or expand upon the approach outside of a controlled formal study, especially since several possible contraindications exist as identified in Subsection 7.1.

7.1 QUANTUM TREATMENT STAGE 1

Duration

A one hour session undertaken two or (mostly) three times per day, for a period of 23 days.

Regime

Each one hour session consisted of meditation/relaxation within a Faraday-type shielding cage (referred to as a Faraday cage from this point forward), listening to soft classical music (Mozart) lying mostly supine. Since the Faraday cage was not air conditioned, several ice and cold packs were available and utilised as required (i.e., depending on the temperature of the day) to ensure a comfortably cool environment.

Faraday Cage Construction

The Faraday cage was constructed from five sheets of 1200 × 2400 Al (5005 H34 alloy), three sheets being 0.8 mm thick, one being 0.6 mm thick, and one being 1.0 mm thick.

The dimensions of the resulting Faraday cage, with over 95% usage of the available Al, were approximately 1920 × 1430 × 700 mm to allow the housing of a double bed size mattress (figure 5). The Al grade, and range of sheet thickness utilised, were chosen on the basis of: RF attenuation effectiveness, availability, and cost minimisation with the overall cost being approximately $300 AUD (including Al rivets and L-shaped angle line edging for the cage's opening that seats a removable lid). The usage of the different sheet thicknesses was however somewhat strategic (e.g., with the 1.0 mm sheet being partially used within the cage base and the remainder for the removable lid).

FIGURE 5. **Various perspectives of a Faraday-type shielding cage housing a double bed size mattress, with and without removable lid.**

Demonstrating the informal, homemade credentials of this latest CFS alleviation effort, functional testing of the Faraday cage simply involved ensuring that a standard non-digital AM/FM radio and cell phone (both placed internally to the cage) remained disconnected reception-wise. It was also ensured through pulse oximetry that blood oxygen saturation percentage, or SpO_2 levels, were not observably affected for a personal enclosure duration of 1.5 hours.

Regime Rationale

The rationale behind shielding against RF exposure is explained within Subsections 5.1 and 6.3. The rationale behind the (mostly) thrice daily approach in part comes from the impracticality of whole-house, or even whole-room, Faraday cage constructions, which are clearly incongruous for an intended inexpensive and simple homemade trial. However, the thrice daily approach was also influenced by the success that some (by no means the majority) have had with other sessional (per-day) therapy regimes (e.g., neural rewiring and cryogenic therapy in the form of ice baths). Such success stories *may* indicate that whatever system/neural reboot is needed for CFS recovery, it can be achieved on an hours-per-day therapy basis.

The ice/cold pack application was with the intention of being comfortable not "torturous", so as to provide a conducive meditation/relaxation environment (which was indeed subjectively the case). The ice/cold pack application was also inspired by the quantum-based suggestion of Subsection 6.2 that CFS might be linked to a minimum quantum neural state[6] associated with the turning-point of figure 3, and so might positively respond to some kind of targeted "excitation" to a healthier quantum neural state. An assumption was made that elevated core body temperature should be avoided for such positive excitation, however because the applied therapy regime aimed to be relatively passive and comfortable, significant core body temperature reduction was avoided.

The classical music component was included to enhance relaxation, and was also motivated by the neural phase encoding connectedness with music theory as found in [18] and the copious formal studies demonstrating the neuro-benefits of music therapy (as briefly introduction in [18]).

Contraindication Examples

Some perceived risks of the above-described treatment approach include: adverse reactions to a confined space including for asthmatics due to reduced airflow; falling asleep in a confined airflow space; working with "sharps" in the form of sheet metal and metal filings; Al exposure; instability of a relatively heavy assembly if not securely constructed; ice burns and/or adverse blood circulatory effects due to ice/cold pack application.

7.2 QUANTUM TREATMENT STAGE 2

Progress results following the 23 day Stage 1 quantum treatment protocol, and based on an Oligo re-scan (December 7), displayed modestly encouraging indicators as outlined within the next Quantum Results Section. However, an unexpected outcome of the re-scan was a seemingly appreciable Al increase within its report's heavy metal test component. The percentage Al increase in relation to the average of the January 19 and August 16

---

[6] Or maximum state depending on one's perspective (i.e., minimum available energy, maximum immune system response, and so on…)

scans was 37%. Since percentage increase can be misleading without consideration of distribution statistics such as standard deviation, providing a less dramatic but still commanding comparison was the re-scan report's qualitative Al level description of "high plus", having been elevated from "high" and "high minus" respectively in relation to the pre-treatment scans.

While the above unexpected outcome was certainly unwanted and demonstrates how adverse outcomes can result outside of a formally controlled study, as per the Oligo scan repeatability comment of Subsection 2.4.3, here again one cannot help but be impressed, this time in relation to scan sensitivity. That is, the re-scan was seemingly sensitive to the activities of construction of, and/or meditation/relaxation within, an Al Faraday cage over several weeks. Gloves were worn for most (but not all) stages of construction and hands were otherwise washed post any construction activity. Hence, the adverse outcome might be explained by carbonic acid, from carbon dioxide build-up within the confined cage, reacting with (vapourising) Al surfaces in relatively early stages of oxidation (which begins immediately upon surface exposure to the atmosphere).

Due to the adverse Al outcome and competing external factors, the treatment trial was suspended for several weeks. During this time-out the internal surfaces of the Faraday cage were sealed with several coatings of extremely low volatile organic compound (VOC) interior house paint marketed for its gentleness in relation to fumes and breathability.

A parallel decision was also made to modify the Faraday cage to increase its ventilation, thereby allowing internal sleeping at nights (so as to possibly increase treatment effectiveness due to body repair and immune system activity that occur during sleep). Accordingly, a duplicate lid was fabricated with over 1100 × 1 mm diameter drill holes spaced in a 3 cm square grid arrangement to give an overall (modest) ventilation area of approximately 9 cm^2. With this night-use lid in place, pulse oximetry percentage SpO_2 levels were not observably affected for a personal enclosure duration of at least 4.5 hours. Enclosure testing beyond this time was not required since night sleeping was intended for up to 4 hours only (representing at least half of the night's sleep).

Approximately 11.5 weeks after the completion of the Stage 1 trial, the Stage 2 trial, involving a daily 60 to 70 minute meditation/relaxation session (one only) and night sleeping for up to 4 hours (approximately 3 hours on average), commenced for a duration of 32 days. After settling into this Stage 2 routine, its sleeping period was scheduled for the "second half" of the night so as to wake up to a new day from the Faraday cage. An Oligo re-scan for the Stage 2 trial was undertaken on March 30, 2022 at a third independent clinic.

8. QUANTUM RESULTS AND DISCUSSION

The following results are from a medical/quantum physicist's perspective without qualifications in nutrition. Thus, nutritional advice is not intended and nor should it be taken from any surrounding discussion.

8.1 PRIMARY QUANTUM ANALYSIS

8.1.1 OVERVIEW (NON-QUANTUM)

Subjective feelings of diarised symptom improvement following Stage 2 treatment, rated as modest, moderate or appreciable and which generally improved upon Stage 1 outcomes, include:

- Reduction in muscle aches (appreciable).
- Reduction in primary governing fatigue (modest-to-moderate).
- Increase in exercise endurance ability (moderate).
- Increase in mental clarity and resilience to mental exertion (moderate).
- Improved (less broken) sleep (modest-to-moderate).

The reduction in muscle aches was particularly noticeable even midway through Stage 1. Before treatment commencement, the continuity of exercise was not possible due to what felt like frequent and wide-spread "micro muscle tears", not just during exercise but upon everyday movements (possibly consistent with the clinical diagnosis of Subsection 2.4.1). By the end of Stage 2, such muscular injury and discomfort had significantly abated allowing a return to exercise continuity and with increased endurance.

While the above subjective feelings of improvement are encouraging, it is recognised that the improvements could simply be attributable to the benefits of prolonged meditation/relaxation which had never before been undertaken for periods comparable to those of the treatment.

Interesting and more quantifiable preliminary outcomes are observed when the 21 element listing of the post-treatment Oligo scans (of December 7, 2021 for Stage 1 and March 30, 2022 for Stage 2) are re-ordered based on the percentage change of element level, as compared to the average of the original January 19 and August 16 pre-treatment 2021 scans (the four scans in chronological order will be referred to as Scans 1, 2, 3 and 4). In descending order of percentage change (i.e., ranked from largest positive change down), table 3 gives the top four elements of scan 4[7]. Other than a slight reordering of the elements (but with Co still remaining in 1st position), the elements identified by table 3 do not change if Scan 4 is compared only against the most recent pre-treatment Scan 2 (this

---

[7] Does not include Se which is omitted from the 21 element analysis due to its marked transient nature between all four Oligo scans. However, Se is considered an essential antioxidant and reduces in level with brain aging such that level targeting through strategies such as dietary supplementation with exercise may reverse memory loss (e.g. in Alzheimer's disease [30]). Hence, significance of the transient observation should not be discounted.

outcome is expected due to the consistency between Scans 1 and 2). Also, a similar analysis for Scan 3 identifies the same elements (with a change of rank order) with reduced percentage change, indicating that the Scan 4 outcomes of table 3 are not random (i.e., not one-off for the day of the scan) but the result of progressive change.

Note that no vitamin/mineral supplements were regularly or sporadically taken during the months leading up to Scans 3 and 4 and similarly no changes in dietary or other relevant habits were introduced during that same period (with a diet consisting of drinking purified non-fluoridated water as standard, and toothpaste brand/type remaining constant).

Table 3. Elements with the largest positive percentage change in level (bracketed value) when comparing post-treatment Oligo Scan 4 with the average values of pre-treatment Scans 1 and 2.

Ranking#	1	2	3	4
Element	Co (+15.8)	Li (+14.8)	P (+14.1)	F (+13.4)

#Rankings are simple in that the percentage changes that govern rank do not consider the standard deviations of element level population distributions.

The four elements identified by table 3, which do not all commence from an obviously low base level, are of interest because of the following possibly pertinent facts:

- The first-ranked element in table 3, Co, plays critical neurophysiological roles and, particularly in the form of vitamin B12 (cyanocobalamin), enhances nerve repair, improves functional recovery after brain injury, and is central to the production of haemoglobin [31,32]. These roles partly stem from being an integral component of a biochemical reaction (transmethylation) that is essential to myelin sheath protein production [31]. Also, upon linear mapping Co is identified in [18] as representing one of the ten Families of neural phase encoding.

- The second-ranked element in table 3, Li, is known to (i) stimulate the proliferation of stem cells, including neural stem cells; (ii) increase the concentrations of neural markers (n-acetyl-aspartate and myoinositol) in the brain; (iii) have a protective effect towards neurons; and (iv) increase brain cell density and volume in patients with bipolar disorder (has long been used by clinicians to treat manic depression) [33].

- The third-ranked element in table 3, P, is a key element identified by the present article as having possible quantum significance (see figure 4 and surrounding commentary), and naturally is key to energy production as per Section 3.

- For the fourth-ranked element in table 3, F, a possibly intriguing aside (for some), is that fluorite crystal is often associated with focus, mental clarity and peace of mind within metaphysical practices.

- Of the 21 elements, Co, Li, P and F are the *four most magnetically/electromagnetically relevant* in terms of quantities such as gyromagnetic ratio, γ, nuclear spin quantum number, I, and spin magnetic dipole moment, μ, as well as in terms of ferromagnetism (elaborated upon with brief explanation of quantities within the next Primary Quantum Results Subsection 8.1.2).

Note that the neurotoxic effects, at adversely elevated levels, of some of the trace elements identified above are acknowledged but not expanded upon within continuing discussion.

Another interesting feature of Scans 3 and 4 is the progressive decline in Mg level, with a substantial -36.1% and -40.8% change at Scans 3 and 4 respectively (again as compared to the average of Scans 1 and 2 which is implied from this point unless otherwise stated). Also, despite the progressive +14.1% increase in P as displayed by table 3, Scan 4 still shows P levels in the low minus (red) region, such was its extremely low commencing base level, and the originally low Zn and Cr levels slipped further backwards in Scan 4 to also join P in the low minus region. More specifically, the overall declines of Zn and Cr at Scan 4 are -5.2% and -5.6% respectively, with Cr actually joining P in the low minus region as of Scan 3.

Understandably, some may express concern at the above Mg, Zn and Cr outcomes (if physiologically legitimate), particularly for Mg given its importance for muscles undergoing exercise, thereby spelling a need for treatment approach avoidance. In the fullness of time that position may prove correct. However, for now a contrary positive position is given consideration. The fact that of the scans' 21 elements, Mg undergoes a substantial and the largest percentage decline, and this decline coincides with a considerable subjective reduction in muscular symptoms, appears to support that the removal of modern ether influences, combined with neural stimulation, had some physiological effect, albeit an unexpected effect. And so one might ask questions such as, does the decline reflect:

- *Muscular uptake of Mg?*
- *Temporary preferential recovery, at the expense of Mg, of the identified most magnetically relevant elements?*

Moreover, long-term disruption of element uptake and metabolic processes may negate body homeostasis and be unpredictably reflected within attempted restorative changes and negative feedback processes (including within the Krebs cycle as per Subsection 2.4.1, and as the body expends energy to maintain affected magnetically relevant elements). Similarly, the removal of said disruption may result in an unexpectedly involved path back to the equilibrium of homeostasis. The Mg result should not however be considered in isolation (i.e., Ca, one of the few elements at a relatively high but still normal pre-treatment level, also underwent progressive decline as discussed shortly in Subsection 8.2).

8.1.2 PRIMARY QUANTUM RESULTS

It is mathematically revealing to collate results of the seven elements with marked outcomes, as identified in the previous Subsection (Co, Li, P, F, Mg, Zn and Cr). The collation of these elements is summarised by table 4 (and see its footnote for the basis of extra Mo inclusion).

Table 4 is mathematically fascinating since for all of the elements: (i) **Z values are integer (n) multiples of 3;** (ii) elements with a *positive* change (Co, Li, P and F) display *odd* values of n, while elements with a *negative* change (Mg, Zn, Cr, and Mo) display *even* values for n; (iii) $\Delta\phi$ values are integer or half-integer (m) multiples of 30°; and (iv) elements with a *positive* change display *half-integer* multiples of m, while elements with a *negative* change display *integer* multiples of m.

Table 4. Summary of elements with the most notable percentage change in level (bracketed) when comparing post-treatment Oligo Scan 4 with the average values of pre-treatment Scans 1 and 2. Element Z values are written as integer, n, multiples of 3, and $\Delta\phi$ values predicted by reverse mapping of Z are written as m multiples of 30°, where m is an integer or integer multiple of a common fraction. Reverse-mapping-predicted $\overline{\alpha}_{\Delta\phi}$ values are given with uncertainties at 95% CI. Median $\overline{\alpha}_{\Delta\phi}$ values that fall within 0.5% of, or approximate to, a nominal integer, or integer multiple of a fraction (⅓ or ¼), are given in the two right-most columns (with the percentage deviation from nominal bracketed). The rightmost inset, for comparison of form, displays the fine structure energy levels of hydrogen based on a rotational kinetic energy extension to Bohr's model [34].

Basis for element inclusion	Element (% change)	Z	n ($Z = n\times3$)	$\Delta\phi$ (degrees)	m ($\Delta\phi = m\times30^{\circ}$)	Model $\overline{\alpha}_{\Delta\phi}$ (degrees)	Nominal $\overline{\alpha}_{\Delta\phi}$ (% departure)
Largest % increase	Co (+15.8)	27	9	135	4½	2.5550 ± 0.0241	$\approx \frac{5}{2}(+2.2)$
	Li (+14.8)	3	1	15	½	0.1948 ± 0.0037	$\approx \frac{1}{5}(-2.6)$
	P (+14.1)	15	5	75	2½	0.6631 ± 0.0121	$\frac{2}{3}(-0.53)$
	F (+13.4)	9	3	45	1½	0.2510 ± 0.0075	$\frac{1}{4}(+0.41)$
Largest % decrease	Mg (-40.8)	12	4	60	2	0.4126 ± 0.0097	$\approx \frac{2}{5}(-3.1)$
Low minus or "red" level#	Zn (-5.2)	30	10	150	5	3.2504 ± 0.0277	$3\frac{1}{4}(+0.01)$
	Cr (-5.6)	24	8	120	4	1.9486 ± 0.0208	$\approx 2(-2.6)$
	Mo (-14.9)	42	14	210	7	6.9218 ± 0.0441	$\approx 7(-1.1)$

#P also qualifies for the low minus category. Mo is shaded since it displays the lowest level of all elements after P, Zn, and Cr, falling just above the low minus threshold.

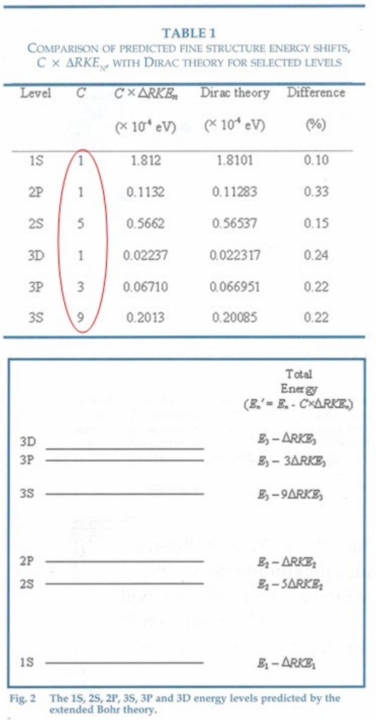

TABLE 1

COMPARISON OF PREDICTED FINE STRUCTURE ENERGY SHIFTS, $C \times \Delta RKE_N$, WITH DIRAC THEORY FOR SELECTED LEVELS

Level	C	$C\times\Delta RKE_n$ ($\times 10^{-4}$ eV)	Dirac theory ($\times 10^{-4}$ eV)	Difference (%)
1S	1	1.812	1.8101	0.10
2P	1	0.1132	0.11283	0.33
2S	5	0.5662	0.56537	0.15
3D	1	0.02237	0.022317	0.24
3P	3	0.06710	0.066951	0.22
3S	9	0.2013	0.20085	0.22

Fig. 2 The 1S, 2S, 2P, 3S, 3P and 3D energy levels predicted by the extended Bohr theory.

The probability of randomly selecting seven elements, with the identified Z multiplicity of 3, from the defined Oligo set is $p = 0.0001$ (and $p < 0.00001$ with Mo inclusion). Even if table 4 construction is considered selective (which to a degree it is since for example the number of elements in each table category differ), the probability of chance occurrence is still considerably low. Furthermore, even though results independence cannot be claimed for established reasons, the findings are based on consistent clinical reports independently obtained from three separate health providers. Findings could not have been foreseen (short of deliberately removing elements such as P and Zn for an extended time from one's diet etc.).

The fascinating (i) to (iv) outcomes above actually display many quantum mechanical characteristics, some of which include:

- Categorisations based on positive versus negative, even versus odd, integer versus half-integer (mindful of quantum properties such as charge, parity and spin).
- In regards to nuclear spin, the increasing elements of Co, Li, P and F have half-integer I values ($I = {}^{7}/_{2}, {}^{3}/_{2}, {}^{1}/_{2}$ and ${}^{1}/_{2}$ respectively with magnitudes in table order), while the decreasing elements of Mg, Zn, Cr and Mo have $I = 0$.
- The $\Delta\phi = m\times30^{\circ}$ multiplicity is interesting since symmetrical occurrences involving 30° (and therefore 60°) govern the quantum properties of elementary particles, for which properties such as charge, spin, strangeness, etc. can be geometrically arranged in various triangular and hexagonal arrays in which such angles are inherent (e.g., hadron arrangement within SU3 group symmetry).

- The $\Delta\phi$ values can in fact be written as multiples of any angle (i.e., not just 30°) with a corresponding multiplicative change in m (such as $\Delta\phi = m'\times 45^\circ$, where m' is an integer, or integer multiple of 1/3, and $\Delta\phi = m''\times 90^\circ$, where m'' is an integer multiple of 1/6). For the latter 90° case (for which m'' values in the elemental order of table 4 are 9/6, 1/6, 5/6, 3/6, 4/6, 10/6, 8/6 and 14/6), it might *loosely* be said that the overall neuro-quantum state (or function) at the time of Scan 4 is formed from a set of *orthogonal* basis states (or functions), which is a most quantum-like scenario.

- Another interesting quantum mechanical characteristic of table 4 comes from comparison with an extension to Bohr's model of atomic hydrogen [34] (while Bohr's model and this extension are semi-quantum due to their classical aspects, they still arguably provide useful physical insights amidst the inherent restrictions of classicality). The extension includes integer, C, multiples of an analytically derived electron rotational kinetic energy (ΔRKE) term and predicts the fine structure energy shifts of electron orbits to high accuracies comparable to Dirac's relativistic treatment. The ΔRKE term is given by:

$$\Delta RKE_n = \frac{\pi m^2 r_e Z^3 e^6}{16\varepsilon_0^3 h^4 n^4}, \tag{3}$$

where m is electron mass[8], r_e is electron radius, e is electron charge magnitude, ε_0 is the permittivity of free space, h is planck's constant, and n is an integer signifying the principal orbit (i.e., is a principal quantum number). Clearly, the m and n in (3) differ from the m and n notation used within table 4, however the original notation of [34] is retained since ambiguity is unlikely and the notation is archetypal of atomic physics and Bohr's model.

A results table from the 2003 *Physics in Canada* publication of the extended model [34], showing the fine structure energy shifts of various orbits in terms of C multiples of ΔRKE_n, is given as an inset to table 4. The tables are presented side-by-side for comparison purposes since the n values for elements with a positive increase in table 4 (i.e., n = 1, 3, 5 and 9), take the same integer values of C in the table inset. The comparison finding is perhaps representative of the fact that quantum mechanical geometric symmetries (e.g., within energy level diagrams) are known to approximately and proportionally reoccur across many atomic scales. This comparison might be further explained by the fact that the C = 1, 3, 5 and 9 fine structure differentiation represents preferred lowest or conventional states of hydrogen, and Case Study treatment outcomes seem to indicate a progression towards increased occupancy of some preferred lower neuro-quantum states.

The Co, Li, P and F description as "most magnetically relevant" in Subsection 8.1.1, and their noting within a recent dot point of having half-integer I (with the decreasing elements of table 4 conversely having $I = 0$), indeed warrant further discussion. The elements are described as most magnetically relevant since F, P and Li appear highest behind H in tabulations (e.g., within MRI) of biological magnetically active elements of abundance and with high γ (recall H is also associated with one of the primary Families of neural phase encoding in [18]). In MRI-type scenarios, γ sets the precession frequency for a given applied magnetic field (as raised in Subsection 5.1) and classically is a measure of how much magnetic effect one gets from a spinning charged particle ($\gamma = \mu/S$ where S is intrinsic spin angular momentum which I parameterises). The γ values of F, P and Li are 40.1, 17.2 and 16.5 MHz/T respectively, compared to 42.6 MHz/T for H (the nuclear magnetic sensitivity of Co is slightly higher than that of Li).

It is also intriguing that Co is one of only three ferromagnetic (at room temperature) elements of biological relevance, the others being Fe ($I = 0$) and Ni ($I = {}^{3}\!/_{2}$), with the trio of transition metals appearing consecutively within the same row of the periodic table. Ferromagnetism is more concerned with *electron* spin, but nonetheless has effect in the MRI environment (as an ongoing analogy) of RF waves and magnetic fields (e.g., ferromagnetism may cause artefacts due to introduced magnetic field heterogeneities).

It is quite fascinating and potentially telling that the *heavy metal* element with the largest percentage increase is Co's ferromagnetic partner, Ni (see Appendix A), while over several years of CFS blood ferritin levels were above typical range without supplements (see Subsection 2.4.4). Adding further fascination, if not supporting evidence, Cr at the opposite end of table 4 is the only *antiferromagnetic* element. Hence, accumulated evidence is suggestive of modern ether removal combined with neural stimulation having catalysed the uptake of the most magnetically relevant elements (which includes P, the focus of previous Sections), from which one might hypothesise that removal of neural phase interference has initiated a biological recovery or response.

When considering the possibility of modern ether interference effects, the $\Delta\phi$ values of table 4 elements being expressible in terms of landmark Cartesian/polar angles (e.g., $\Delta\phi_{\mathrm{Co}} = 90^\circ + 45^\circ$, $\Delta\phi_{\mathrm{Li}} = 45^\circ - 30^\circ$, $\Delta\phi_{\mathrm{P}} = 45^\circ + 30^\circ$, $\Delta\phi_{\mathrm{F}} = 45^\circ$, $\Delta\phi_{\mathrm{Mg}} = 60^\circ$, $\Delta\phi_{\mathrm{Zn}} = 180^\circ - 30^\circ$, $\Delta\phi_{\mathrm{Cr}} = 180^\circ - 60^\circ$, $\Delta\phi_{\mathrm{Mo}} = 270^\circ - 60^\circ$) is interesting despite some degree of mathematical expectedness. Interest here derives from some phase-shift keying schemes within digital RF communication encoding using such angular values for their phase shifts. Also, $\Delta\phi$ formation about landmark angles here is generally consistent with the radial geometry of neural phase wheels in [18] (see within for phase wheel definition). However, CFS has existed since before the

---

[8] Accuracy is enhanced by substituting the reduced mass expression, $mM/(m + M)$ for m, where M is the mass of the hydrogen nucleus.

advent of digital RF communication, and so the interference justification of Subsection 6.3.1 remains a primary justification.

Another interesting observation for table 4 is that $\overline{\alpha}_{\Delta\phi}$ values approximate as integers or simple common fractions. Interest in integer/fractional-integer alignment for $\overline{\alpha}_{\Delta\phi}$ stems from possible connectedness to some quantum process, since such multiplicities are quintessentially characteristic of a range of quantum systems. Interest also stems from possibly providing another avenue for modern ether interference (as explained within Appendix B, wherein Table B1 lists all elements from $Z = 1$ to 63 for which generated median $\overline{\alpha}_{\Delta\phi}$ values fall within 0.5% of some integer, or integer multiple of ⅓ or ¼).

Note that the $\overline{\alpha}_{\Delta\phi}$ values predicted by (1) and given in table 4 and table B1 are taken as falling exactly on the $\overline{\alpha}_{\Delta\phi}$ versus $\Delta\phi_c$ model curve of figure 3, whereas in [18] all Family $\overline{\alpha}_{\Delta\phi}$ values fall slightly off the model curve (as is the norm for most curves-of-best-fit), despite the curve's exceptionally high correlation. In [18] it is assumed with justification that these slight departures or residuals carry quantum significance. While that assumption is still firmly advocated, the present article takes $\overline{\alpha}_{\Delta\phi}$ values as falling exactly on the $\overline{\alpha}_{\Delta\phi}$ versus $\Delta\phi_c$ model curve for convenience (here the same level of high precision analysis is not required for points made), and because both perspectives can readily co-exist and hold quantum significance[9].

Due to the approximate integer/fractional-integer values of $\overline{\alpha}_{\Delta\phi}$ in table 4, the ratios of these values will also naturally approximate as integers or simple common fractions as per [18] (wherein $\overline{\alpha}_{\Delta\phi}$ values are generally not integers or fractional-integers and are known to higher accuracy, and so the formation of precise ratio values in [18] is more remarkable).

Other quantum mechanical comparisons can be made for table 4 which accounts for most of the relevant body elements with $Z = n \times 3$ (the Oligo scan understandably does not include C, Ar and Kr). However, these comparisons are not pursued here, with other interesting Oligo scan outcomes now preferentially explored.

8.2 PERSONAL QUANTUM INDICES

Subsection 6.2 shared early quantum insights, involving the elements B, Ca, P and Zn, which set the current scene. Within that Subsection the ratios B:P, B:Zn, B:(P×Zn), and (B×Ca):(P×Zn), were proposed as possible personal CFS indices during recovery. Returning for a closer inspection of these elements, it can now be revealed that over the course of Scans 3 and 4, the relatively high values of B and Ca progressively reduced by overall amounts of -14.8 and -15.6% respectively, to the point of B no longer being the element with the highest level (a quite interesting outcome in the absence of any dietary change or supplement intake).

Table 5 contains the values of these ratios for Scans 1 to 4, with the B:P and (B×Ca):(P×Zn) ratios demonstrating the largest progressive changes of -34% and -51% respectively at Scan 4. Hence, the ratios appear to be sensitive to perceived feelings of CFS improvement, and the progressive declines in B and Ca with increase in P suggest that the quantum scenario speculated in Subsection 6.2 might possibly hold some basis. Of course despite the 14.1% increase in P, the fact that P and Zn levels are in the low minus region at Scan 4 would mean that there is much scope for further recovery and corresponding ratio declines (as per subjective feelings). The slipping backwards of Zn levels mathematically explains why some of the proposed indices appear less sensitive than others at the Scan 4 stage of seemed recovery.

Table 5. Ratios B:P, B:Zn, B:(P×Zn), and (B×Ca):(P×Zn), proposed as possible personal CFS indices, calculated from the elemental values pre-treatment Scans 1 and 2, and post-treatment Scans 3 and 4. The percentage changes (bracketed) are in comparison to the average of the two pre-treatment scans.

Ratio	Scan 1 (19 Jan)	Scan 2 (16 Aug)	Average (pre-treatment)	Scan 3 (7 Dec)	Scan 4 (30 Mar)
B:P	0.0374	0.0346	0.0360	0.0320 (-13)	0.0269 (-34)
B:Zn	0.0303	0.0296	0.0299	0.0270 (-11)	0.0269 (-11)
B:(P×Zn)	0.000329	0.000298	0.000314	0.000281 (-12)	0.000247 (-27)
(B×Ca):(P×Zn)	0.187	0.174	0.181	0.145 (-25)	0.120 (-51)

The in-tissue -15.6% decline for Ca could alone carry important ramifications beyond illnesses like CFS, but on this point especially one should not speculate upon tentative results.

9. CONCLUSIONS, FUTURE DIRECTIONS AND IMPLICATIONS

The many identified quantum characteristics of element level changes for a long-term CFS sufferer in response to modern ether removal and neural stimulation may suggest that electromagnetic environmental factors can have an adverse neurosphysiological effect for the susceptible few and that the high-order phase encodings of neural processes are indeed quantum mechanically based.

The quantified explanation as to why the modern ether may have an adverse neurophysiological effect is original and arguably convincing (e.g., partially based upon the phase modulations of FM transmissions overlapping with key $\overline{\alpha}_{\Delta\phi}$ values of neural phase encoding). Also arguably convincing is the fact that in response to modern ether removal, the most magnetically relevant body elements displayed the largest percentage increase in levels. Implications of this outcome may explain why the large majority of people who recover

---

[9] As an analogy, electron orbits of the principal energy levels of the hydrogen atom carry exact parabolic functionality of significance [18,34], but fine structure energy levels which are perturbed slightly away from the principal levels also carry significance.

from CFS do not fully recover to pre-illness energy levels (i.e., the continuing presence of the modern ether may cause chronic low-level neural phase interference despite some degree of effective neural rewiring or related recovery).

The presented Case Study results may show a system that has begun to heal in response to the applied (in two stages) "quantum treatment" by: an appreciable reduction in muscular discomfort; a modest-to-moderate reduction in primary fatigue; a moderate increase in exercise endurance ability; P levels being on the increase; and marked changes in proposed personal quantum indices. Treatment has continued since the end of the Stage 2 reporting, with further subjective improvements experienced. Over the course of 29 years no other approach has brought any meaningful personal relief and, like all with CFS, the approaches trialled have been numerous.

As advocated throughout, a future controlled formalised study is required to uphold the presented justified hypothesis and its quantum mechanical rationale with tentative findings. If the hypothesis is upheld, then the following final messages ensue:

- One or more of the (in tissue) ratios, B:P, B:Zn, B:(P×Zn), or (B×Ca):(P×Zn), may be useful personal indices for relative monitoring during CFS recovery, especially for long-term CFS sufferers.

- Research into how RF communication approaches can be modified to avoid or reduce the risk of possible subtle adverse neurological health effects (originating from complex neural impulse phase signalling interference) in the susceptible few would be indicated. For the majority such modifications would not be necessary, as per the non-alarmist tone throughout in regards to modern RF ether exposure. As research and understanding progress, similar modifications but in favour of the majestic intelligent mammals of the ocean may also be indicated.

- The complementary use of music therapy can most likely be improved upon, especially given that some neurological illnesses require interventions as invasive as deep brain stimulation. Hence, the replacement of music therapy by a slightly less passive complementary treatment partner (e.g., transcranial magnetic stimulation) may prove more effective whilst also catering for hearing impaired persons involved in any future study.

- A discussion on the potential benefits of regular meditation or quite time, not just within a space free of distraction, but also within an electromagnetically silent space, is encouraged (which naturally carries over to home/workplace design and daily practices).

- On a more broad philosophical level, if a mostly inert, invisible and widely-considered socially beneficial phenomenon such as RF atmospheric transmissions can, for a susceptible few, subtly (without known definitive biomarkers) hinder neural recovery or facilitate adverse neurological health effects, what then must be the long-term adverse environmental and health effects of the unfathomable tonnage of toxic pollutants continually pumped and dumped upon our once pristine Earth?

REFERENCES

1. Kim DY, Lee JS, Park SY, Kim SJ, Son CG. 2020 Systematic review of randomized controlled trials for chronic fatigue syndrome/myalgic encephalomyelitis (CFS/ME). *J. Transl. Med.* **18**:7. (https://doi.org/2010.1186/s12967-019-02196-9)
2. Brenna E, Araja D, Pheby DFH. 2021 Comparative survey of people with ME/CFS in Italy, Latvia, and the UK: A report on behalf of the Socioeconomics Working Group of the European ME/CFS Research Network (EUROMENE). *Medicina* **57**:300. (https://doi.org/10.3390/medicina57030300)
3. Muirhead N, Muirhead J, Lavery G, Marsh B. 2021 Medical School Education on Myalgic Encephalomyelitis. *Medicina* **57**:542. (https://doi.org/10.3390/medicina57060542)
4. Action for ME. *What is ME Introduction and Big Survey* [Internet, cited 2021 July 23]. Available from: https://www.actionforme.org.uk
5. Kapur N, Webb R. 2016 Suicide risk in people with chronic fatigue syndrome. *Lancet* **387,** 1596-1597. (https://doi.org/10.1016/S0140-6736(16)00270-1)
6. Komaroff AL. 2019 Advances in understanding the pathophysiology of ME/CFS. *JAMA* **322,** 499-500. (https://doi.org/10.1001/jama.2019.8312)
7. Sandler CX, Lloyd AR. 2020 Chronic fatigue syndrome: Progress and possibilities. *Med. J. Aust.* **212,** 428-433. (https://doi.org/10.5694/mja2.50553)
8. Saha AK, Schmidt BR, Wilhelmy J, Nguyen V, Abugherir A, Do JK, Nemat-Gorgani M, Davis RW, Ramasubramanian AK. 2019 Red blood cell deformability is diminished in patients with chronic fatigue syndrome. *Clin. Hemorheol. Microcirc.* **71,** 113-116. (https://doi.org/10.3233/CH-180469)
9. Miwa K. 2015 Cardiac dysfunction and orthostatic intolerance in patients with myalgic encephalomyelitis and a small left ventricle. *Heart Vessels* **30,** 484-489. (https://doi.org/10.1007/s00380-014-0510-y)
10. Richards RS, Wang L, Jelinek H. 2007 Erythrocyte oxidative damage in chronic fatigue syndrome. *Arch. of Med. Res.* **38,** 94-98. (https://doi.org/10.1016/j.arcmed.2006.06.008)
11. Morris G, Maes M. 2014 Mitochondrial dysfunctions in myalgic encephalomyelitis/chronic fatigue syndrome explained by activated immuno-inflamatory, oxidative and nitrosative stress pathways. *Metab. Brain Dis.* **29,** 19-36. (https://doi.org/10.1007/s11011-013-9435-x)
12. Marshall M. 2020 COVID-19's lasting misery. *Nature* **585,** 339-341. (https://doi.org/10.1038/d41586-020-02598-6)
13. Marshall M. 2020 How COVID-19 can damage the brain. *Nature* **585,** 342-343. (https://doi.org/10.1038/d41586-020-02599-5)
14. Bested AC, Marshall LM. 2015 Review of myalgic encephalomyelitis/chronic fatigue syndrome: an evidence-based approach to diagnosis and management by clinicians. *Rev. Environ. Health* **30,** 223-249. (https://doi.org/10.1515reveh-2015-0026)
15. Shepherd CB. 2017 PACE trial claims for recovery in myalgic encephalomyelitis/chronic fatigue syndrome – true or false? It's time for an independent review of methodology and results. *J. Health Psychol.* **22,** 1187-1191. (https://doi.org/10.1177/1359105317703786)
16. Marshall M. 2021 COVID's toll on small and taste: what scientists know. *Nature* **589,** 342-343. (https://doi.org/10.1038/d41586-021-000556)
17. Douaud G, Lee S, Alfaro-Almagro F, Arthofer C, Wang C, McCarthy P, Lange F, Andersson JLR, Griffanti L, Duff E, et al. 2022 SARS-CoV-2 is associated with changes in brain structure in UK Biobank. *Nature.* (https://doi.org/10.1038/s41586-022-04569-5)
18. Simeoni RJ. 2021 A new approach to high-order electroencephalogram phase analysis details the mathematical mechanisms of central nervous system impulse encoding. *UNET J. Sci. Soc.* **1,** 1-34. (https://doi.org/10.52042/UNETJOSS010101)

19. Simeoni RJ. A discrete oscillator phase noise effect applied within phase-shift keying RF digital signal modulation. In: 9th International Conference on Signal Processing and Communication Systems; 2015 December 14-16; Cairns, Australia. p. 1-9. (https://doi.org/10.1109/ICSPCS.2015.7391745)
20. British Broadcasting Corporation. 2013 *The truth about sleep*, Producer England R.
21. British Broadcasting Corporation. 2016 *Medical mavericks: the history of self-experimentation*, Producer Gregory A.
22. Sinclair HM. 1956 Deficiency of essential fatty acids and atherosclerosis, etcetera. *Lancet* **267,** 381-383. (https://doi.org/10.1016/S0140-6736(56)90126-X)
23. Sjölin J, Stjernström H, Henneberg S, Hambraeus L, Friman G. 1989 Evaluation of 3-methylhistidine excretion in infection by 1-methylhistidine and the creatine ratios. *Am. J. Clin. Nutr.* **49,** 62-70. (https://doi.org/10.1093/ajcn/49.1.62)
24. Sheffield-Moore M, Dillon EL, Randolph KM, Casperson SL, White GR, Jennings K, Rathmarcher J, Schuette S, Janghorbani M, Urban RJ, et al. 2014 Isotopic decay of urinary or plasma 3-methylhistidine as a potential biomarker of pathologic skeletal muscle loss. *J. Cachexia Sarcopenia Muscle* **5,** 19-25. (https://doi.org/10.1007/s13539-013-0117-7)
25. Juste C, Gerard P. 2021 Cholesterol-to-coprostanol conversion by the gut microbiota: what we know, suspect and ignore. *Microorganisms* **9**:1881. (https://doi.org/10.3390/microorganisms9091881)
26. Mutter J. 2011 Is dental amalgam safe for humans? The opinion of the Scientific Committee of the European Commission. *J. Occup. Med. Toxicol.* **6**:2. (https://doi.org/10.1186/1745-6673-6-2)
27. Abernathy B, Hanrahan SJ, Kippers V, Mackinnon LT, Pandy MG. 2005 *The biophysical foundations of human movement*, 2nd ed. South Yarra, Victoria: Palgrave Macmillan.
28. Gasda PJ, Haldeman EB, Wiens RC, Rapin W, Bristow TF, Bridges JC, Schwenzer SP, Clark B, Herkenoff K, Frydenvang J, et al. 2017 In situ detection of boron by ChemCam on Mars. *Geophys. Res. Lett.* **44,** 8739-8748. (doi:10.1002/2017GL074480)
29. Smedler E, Uhlén P. 2014 Frequency decoding of calcium oscillations. *Biochem. Biophys. Acta.* **1840,** 964-969, 2014. (https://doi.org/10.1016/j.bbagen.2013.11.015)
30. Van der Jeugd A, Parra-Damas A, Baeta-Corral R, Soto-Faguas CM, Ahmed T, LaFerla FM, Giménez-Llort L, D'Hooge R, Saura CA. 2018 Reversal of memory and neuropsychiatric symptoms and reduced tau pathology by selenium in 3xTg-AD mice. *Sci. Rep.* **8**:6431. (https://doi.org/10.1038/s41598-018-24741-0)
31. Flippo TS, Holder Jr WD. 1993 Neurological degeneration associated with nitrous oxide anesthesia in patients with vitamin B12 deficiency. *Arch. Surg.* **128,** 1391-1395. (doi:10.1001/archsurg.1993.01420240099018)
32. Wu F, Xu K, Liu L, Zhang K, Xia L, Zhang M, Teng C, Tong H, He Y, Xue Y, et al. 2019 Vitamin B12 enhances nerve repair and improves functional recovery after traumatic brain injury. *Front. Pharmacol.* (https://doi.org/10.3389/fphar.2019.00406)
33. Young W. 2009 Review of lithium effects on brain and blood. *Cell Transplant.* **18,** 951-975. (https://doi.org/10.3727/096368909X471251)
34. Simeoni RJ. 2003 Bohr's model of atomic hydrogen extended to include electron rotational kinetic energy. *Physics in Canada.* **59**, 309-311.
35. Anke M, Croppel B, Kronemann H, Grün M. 1984 Nickel – an essential element. *IARC Sci. Publ.* **53,** 339-365.

ACKNOWLEDGMENTS AND DATA AVAILABILITY

For those interested, the Author welcomes emailed requests for further details relating to the presented Case Study. Similarly, the extended May 9, 2022 "World ME Day version" of this article, that supports the day's theme of *#LearnFromME*, is also available from the Author.

APPENDIX A – HEAVY METAL OBSERVATIONS

The described quantum treatment approach having some effect on heavy metal levels is not to be expected, especially for relatively short treatment periods. Nonetheless, the human body has some ability for the self removal of heavy metals and interesting observations are revealed when a quantum analysis similar to that of Subsection 8.1 is applied to the 15 heavy metal elements assessed within the Oligo scan. Before presenting analysis results in terms of ranked level changes, it is declared that trends are not as convincing as in Subsection 8.1 (e.g., in terms of the progressive nature of changes) but conversely it is recognised that if any effect is real, then practical limits must apply since continual change without limit would be unreasonable to expect, and unhealthy in the case of increasing levels (which must eventually plateau).

When ranking the heavy metal elements[10] in descending order from largest percentage increase down, the first ranked element for both Scans 3 and 4 is Ni. While the increase is modest (12% and 8% for Scans 3 and 4 respectively), the ranking is somewhat interesting since the reversed mapped value of $\Delta\phi_{Ni} = 140^o$ is angularly equivalent to 50^o about a landmark Cartesian angle (i.e., $140^o = 90^o + 50^o$) and $\Delta\phi_c = 50^o$ equates to one of the eight primary Family members in [18]. Also, the corresponding value of $\overline{\alpha}_{Ni}$ is approximately 30^o (29.44 ± 0.12^o) which is interesting given the $\Delta\phi = m\times 30^o$ multiplicity in table 4. The result may lead one to ponder whether removal of the modern ether, and hence removal of some associated phase interference around 30^o, combined with neural stimulation, catalysed some change involving increased Ni uptake or utilisation.

This highest ranking for Ni is also interesting from an essential trace element perspective. That is, Ni deficiency reportedly [35] may disturb skeletal incorporation of Ca, lead to adverse skin effects, and disturb Zn and carbohydrate metabolism. Table 4 seems to indicate disturbed Zn metabolism and skin symptoms are a non-specified (by the present article) aspect of the Case Study. While the initial Ni levels in Scans 1 and 2 are not reported as being excessively low (one of six heavy metals in the normal or green range), one might ask … *is the modest Ni increase reflecting the commencement of system healing?*

Cd and ~~Pb~~ Hg are the heavy metals with the two highest relative levels (consistently the case for Oligo Scans 1 to 4, both being in the high plus yellow but not excessive range). Furthermore, the highest-to-lowest ranking topped by Ni places Pb last for both Scans 3 and 4 (i.e., on average Pb levels reduce by the most). Even more interesting than the Ni 50^o angular outcome is the fact that $\Delta\phi_{Pb} = 410^o$ is solely equivalent to 50^o (i.e., $360^o + 50^o$). The above observations are summarised by table A1, which as per Subsection 8.1

---

[10] Al is omitted from the analysis due to the previously noted adversely appreciable increase in its level (which had reduced from Scans 3 to 4).

possibly provides a glimpse from a quantum mechanical perspective as to why heavy metals interfere with processes involving essential elements (the table also includes related Ag and Gd observations).

Table A1. Heavy metal elements with the most notable level change when comparing post-treatment Oligo Scan 4 with the average values of pre-treatment Scans 1 and 2. Also selectively given are $\Delta\phi$ values (deconstructed), and a notable corresponding $\overline{\alpha}_{\Delta\phi}$ value for Ni as predicted by reverse mapping.

Basis for element inclusion	Element	Z	$\Delta\phi$ (degrees)	Model $\overline{\alpha}_{\Delta\phi}$ (degrees)
Largest % increase	Ni	28	140 (90+50)	29.44 ± 0.12
Largest % decrease	Pb (1st)	82	410 (360+50)	
	Ag (2nd)	47		
	Gd (3rd)	64	320 (270+50)	

Supportive of the high Cd levels across Scans 1 to 4 is a hair toxicology test of March 2021 (with analysis performed within the Environmental Analysis Laboratory, Southern Cross University, by a commercial provider – result ID: K3573-1). The analysis highlights Cd as being the only heavy metal in the provider's defined red zone, with a level of 0.062 mg/kg being approximately three times a population average and just falling into said zone. More than one health practitioner, including my CFS specialist physician, has suggested the possibility of heavy metals adversely replacing desirable elements at the cellular level and within the Krebs cycle. Noting that Cd vertically proceeds Zn in Group 12 of the periodic table (and therefore has the same outer-most subshell electron configuration of $d^{10}s^2$), and that Zn and Cd both have Z values that are integer multiples of 3 (recall that Subsection 8.1 quantum findings arose from the observation that all Z values in table 4 are integer multiples of 3), some Cd-based disturbance as a contributing CFS factor for the presented Case Study may be indicated.

The identification of Ag in table A1 is interesting given the controversy surrounding colloidal Ag supplements, but again it is not appropriate or possible to draw conclusion from the tentative result.

APPENDIX B – SUPPLEMENTARY REVERSE MAPPING RESULTS

This Appendix contains further outcomes from the reverse mapping modus operandi of Subsection 6.2 (i.e., applies the $\Delta\phi_c/5 \rightarrow z \rightarrow Z$ transformation in reverse). Here, the reverse mapping is applied to all elements from $Z = 1$ to 63, and then only selects those with a median $\overline{\alpha}_{\Delta\phi}$ value, as generated by (1), that falls within 0.5% of some integer, or integer multiple of a fraction (⅓ or ¼), when expressed in units of degrees.

Interestingly, table B1 contains several of the "usual suspect" elements from the main discussion. Note that as explained in Subsection 8.1, predicted $\overline{\alpha}_{\Delta\phi}$ values given in table B1 are taken as falling exactly on the $\overline{\alpha}_{\Delta\phi}$ versus $\Delta\phi_c$ model curve of figure 3, whereas in [18] all Family $\overline{\alpha}_{\Delta\phi}$ values fall slightly off the model curve. Hence, the predicted $\overline{\alpha}_{\Delta\phi}$ value for Ar in table B1 differs slightly from the corresponding value stated in [18]. Several intriguing aspects of table B1 exist but are not pursued here (e.g., the noble gas elements of Ar and Xe having landmark $\Delta\phi$ values of 90° and 270° respectively, and linkage of some of the heavier elements via a known decay chain).

The primary reason for identifying elements with integer-related $\overline{\alpha}_{\Delta\phi}$ values within table B1 is that there is an uncanny integer connectedness for $\overline{\alpha}_{\Delta\phi}$ values in the main table 4. It may well be that this connectedness is an all-for-one chance occurrence. Viz., if the ratios of $\overline{\alpha}_{\Delta\phi}$ values display fractional connectedness, as in [18], then one by-chance absolute alignment (to within 0.5% as specified) would result in alignment for all (the previously explained $\alpha_{\min} \approx 0.1740^\circ$ that applies across all Families in [18] is also suggestive of some universal linkage). The non-SI unit of degree is an artificial construct and so no obvious reason exists as for why $\overline{\alpha}_{\Delta\phi}$ values would align with such a construct. Regardless, alignment exists and amidst the complexity of the modern ether there may well be indirect fractional-integer phase modulations comparable to the $\overline{\alpha}_{\Delta\phi}$ values of table B1 (since RF communication transmissions routinely contain ordered arrays of integer spaced quantities, and digital phase-shift keying schemes certainly employ integer amounts of degrees in their discrete phase shifting). Hence, the two right-most columns of table B1 are worthy of reporting.

Table B1. $\Delta\phi_c$ and corresponding $\overline{\alpha}_{\Delta\phi}$ values predicted by reverse mapping of elements from $Z = 1$ to 63 and for which generated (median) $\overline{\alpha}_{\Delta\phi}$ values fall within 0.5% of some integer, or integer multiple of a fraction (⅓ or ¼), when expressed in units of degrees. Uncertainties are stated at 95% CI.

Z	Element	$\Delta\phi$ (degrees)	Model $\overline{\alpha}_{\Delta\phi}$ (degrees)	± (degrees)	Nominal $\overline{\alpha}_{\Delta\phi}$ (degrees)	Deviation (%)
9	F	45	0.2510	0.0075	¼	0.40
15	P	75	0.6631	0.0121	⅔	-0.53
18	Ar	90	1.0026	0.0148	1	0.26
29	Cu	145	3.0087	0.0265	3	0.29
30	Zn	150	3.2504	0.0277	3¼	0.012
31	Ga	155	3.5020	0.0289	3½	0.057
46	Pd	230	8.4619	0.4484	8½	-0.45
53	I	265	11.5377	0.3281	11½	0.33
54	Xe	270	12.0167	0.1391	12	0.14
55	Cs	275	12.5055	0.0442	12½	0.044
56	Ba	280	13.0042	0.0327	13	0.033
57	La	285	13.5129	0.0952	13½	0.095
58	Ce	290	14.0314	0.2239	14	0.22